High-*P*-*T* early Palaeoproterozoic metamorphism in southern India

Jade Anderson

Supervisors: Alan Collins, Martin Hand and David Kelsey

2010 Honours student, Centre for Tectonics, Resources and Exploration

Geology and Geophysics, School of Earth and Environmental Sciences,

The University of Adelaide, Adelaide, S.A 5005, Australia

Email: jade.anderson@student.adelaide.edu.au

ABSTRACT

Southern India is comprised of granulite facies metamorphosed crustal blocks, separated by crust penetrating shear zones that have experienced a diverse tectonothermal history from the Archaean to Cambrian. The early Palaeoproterozoic metamorphosed Salem Block in southern India preserves felsic and mafic gneisses ideal for investigating the aerial extent of the preserved Archaean-Palaeoproterozoic southern Indian crust and the metamorphic rock record in the Archaean-Palaeoproterozoic transition. U-Pb zircon, *in situ* monazite geochronology and zircon REE analysis obtained using Laser-Ablation Inductively-Coupled-Plasma Mass-Spectrometry (LA-ICP-MS), and *P-T* phase equilibria and average *P-T* conventional thermobarometry calculated using THERMOCALC from the Kanja Malai Hills, demonstrate that the Salem Block extends south to at least the northern Palghat-Cauvery Shear System. Peak *P-T* estimates of ~800-850 ºC and 14-16 kbar at *ca.* 2490 Ma were attained in the southern Salem Block and suggest decompression followed peak metamorphism. The *P-T-t* constraints in the southern Salem Block are anomalously high pressure compared to other Archaean-Palaeoproterozoic metamorphic events and require thermal regimes that are typically generated in convergent plate margin settings.

Keywords: Southern Granulite Terrane, Salem Block, metamorphism, LA-ICP-MS, U-Pb geochronology, Palaeoproterozoic.

TABLE OF CONTENTS

1. INTRODUCTION

Understanding the physical and thermal conditions of tectonism in a temporal framework provides a wealth of information about the thermal characteristics of tectonic processes (e.g. Kelsey *et al.* 2007; Clark *et al.* 2009b; Cutts *et al.* 2010). Of particular interest is the pre-early Palaeoproterozoic metamorphic record, which has been documented to preserve markedly different metamorphic characteristics, principally the rarity of eclogite facies assemblages and relative abundance low-medium pressure, amphibolite-granite facies assemblages (e.g. Harley 1989; Bégin & Pattison 1994; Pattison *et al.* 2003) when compared to modern day tectonothermal regimes (e.g. Corfu *et al.* 2003b; Liou *et al.* 2004). Exploring the *P-T* evolution of regions that have experienced Archaean-earliest Palaeoproterozoic metamorphism can provide a fundamental window into these thermal and tectonic processes of the earlier Earth (c.f. Brown 2007a; Brown 2007b).

The southern margin of the Salem Block, comprising the southern Dharwar Craton and Southern Granulite Terrane in southern India is an ideal area to investigate such *P-T* conditions of Neoarchaean-earliest Palaeoproterozoic metamorphism. The Salem Block underwent high grade metamorphism in the Neoarchaean-Palaeoproterozoic (Peucat *et al.* 1993; Raith *et al.* 1999; Mojzsis *et al.* 2003; Clark *et al.* 2009a; Sato *et al. in press*), and has also been linked to Neoproterozoic-Cambrian metamorphism (Bhaskar Rao *et al.* 1996; Meißner *et al.* 2002; Ghosh *et al.* 2004). The correlation between the timing and conditions of metamorphism remains poorly understood due to the sparse *P-T* constraints and lack of previous work that integrate geochronological and metamorphic data sets. As a consequence, a full understanding of the southern spatial extent of the

Salem Block and tectonometamorphic processes is currently hampered. This study presents an integrated geochronological, zircon REE, metamorphic and structural dataset of the Kanja Malai Hills, situated along the northern boundary of the Palghat Cauvery Shear System and southern margin of the Salem Block. The results presented here will aid to: 1) quantitatively constrain the pressure-temperature and timing of metamorphism of the Salem Block, 2) refine the spatial extent of the Palghat Cauvery Shear System and the southern extent of the Dharwar Craton, and 3) provide a foundation for examining the metamorphic conditions of an unusually high *P*, early Palaeoproterozoic metamorphosed terrane.

2. GEOLOGICAL BACKGROUND

2.1 Regional geological overview of Southern India

Peninsular India (Fig. 1b) represents a series of largely granulite facies crustal blocks that are bounded by crust penetrating shear zones and collectively termed the Southern Granulite Terrane (SGT). This study adopts the definition of the SGT as being the dominantly granulite facies domain south of the largely granite-greenstone, low grade Dharwar Craton, southern India (e.g. Ghosh *et al.* 2004). The most northern unit of the SGT, the Salem Block, consists of charnockitic, metaigneous and metasedimentary gneisses that underwent metamorphism in the late Archaean to early Palaeoproterozoic (Peucat *et al.* 1993; Raith *et al.* 1999; Mojzsis *et al.* 2003; Clark *et al.* 2009a; Sato *et al. in press*). The Salem Block is bounded to the south by the Palghat Cauvery Shear System (PCSS), also referred to as the Cauvery Shear Zone (Bhaskar Rao *et al.* 1996; Chetty *et al.* 2003) and Palghat Cauvery Shear Zone (Ghosh *et al.* 2004). The PCSS was first recognised by Drury and Holt (1980) via Landsat images, and has subsequently been characterised as a ~100 km wide, E–W trending, crustal scale (Reddy *et al.* 2003), dominantly dextral set of anastomosing shear zones, interpreted to represent a constrictional transpressional flower structure (Chetty *et al.* 2003; Chetty & Bhaskar Rao 2006a). Lithologies within the PCSS have been reported to consist of intercalated aggregates of mafic gneisses, metasedimentary rocks, charnockites (Bhaskar Rao *et al.* 1996; Bhaskar Rao *et al.* 2003), and Al–Mg rich gneisses (Shimpo *et al.* 2006; Collins *et al.* 2007a; Santosh *et al.* 2008; Clark *et al.* 2009b).

The timing and *P-T* conditions of metamorphism in the PCSS have been of recent interest, with studies demonstrating that high to ultrahigh temperature, medium pressure metamorphism occurred during the Cambrian in the south of the PCSS (Collins *et al.* 2007a; Santosh *et al.* 2008; Clark *et al.* 2009b). In addition, some studies have presented Sm–Nd and Rb–Sr mineral ages of *ca.* 500–730 Ma from lithologies of the PCSS (Bhaskar Rao *et al.* 1996) and within shear zones of the PCSS (Meißner *et al.* 2002). The anomalous structural, lithological, metamorphic and isotopic nature of the PCSS when compared to adjoining crustal blocks has lead to the general consensus that the PCSS represents a large-scale crustal structure, although the exact nature and age of the PCSS remains contentious. Most interpretations of recent work ascribe the PCSS to one of the following two broad models: 1) the PCSS as a Neoproterozoic to early Cambrian structure (suture zone) (Meißner *et al.* 2002; Collins *et al.* 2007a; Santosh *et al.* 2009; Clark *et al.* 2009a) or 2) the PCSS as Archaean crust reworked during the Palaeoproterozoic and Neoproterozoic (Harris *et al.* 1994; Bhaskar Rao *et al.* 1996; Chetty *et al.* 2003; Ghosh *et al.* 2004; Chetty & Bhaskar Rao 2006b). Some workers have noted lithological and isotopic similarities that extend south of the PCSS to a lineament, subsequently referred to as the Karur-Kamban-Painavu-Trichur (KKPT) Shear Zone (Ghosh *et al.* 2004) or similar Karur-Oddanchatram Shear Zone (KOSZ) (Bhaskar Rao *et al.* 2003), which has been interpreted to represent the terrane boundary between northern and southern crustal blocks.

South of the PCSS, the Madurai Block and Trivandrum Block are separated by the Achankovil Shear Zone and contain dominantly metasedimentary gneisses, with a component of charnockitic gneisses in the northern Madurai Block. The Madurai and

Trivandrum Blocks were metamorphosed to granulite facies in the late Neoproterozoic to Cambrian (Bartlett *et al.* 1998; Braun *et al.* 1998; Ghosh *et al.* 2004; Santosh *et al.* 2006; Santosh *et al.* 2006c; Braun *et al.* 2007; Collins *et al.* 2007b).

2.2 The Salem Block

The focus of this study is the Salem Block, which is also known as the Northern Block/Domain (e.g. Drury *et al.* 1984; Chetty *et al.* 2003), southern Dharwar Craton (e.g. Raase *et al.* 1986) and Karnataka Craton (Bartlett *et al.* 1998). In this study, it is referred to as the amphibolite-granulite facies crustal domain extending from the greenschist-amphibolite boundary in the north, termed the Fermor Line (Fermor 1936), to the PCSS in the south. The transitional nature of the boundary between the low-grade Dharwar Craton and the dominantly high grade Salem Block, including structural and lithological similarities of both blocks (Drury *et al.* 1984), and a gradational increase in metamorphic grade north to south from the Dharwar Craton to the southern Salem Block (Janardhan *et al.* 1982; Raase *et al.* 1986; Rameshwar Rao *et al.* 1991) is supportive of the Salem Block representing the high grade metamorphosed continuation of the Dharwar Craton. The Salem Block contains charnockites, variable abundances of metaigneous rocks and metamorphosed metasedimentary rocks, including calcsilicates and magnetite-bearing quartzites. The southern granulite facies region of the Salem Block is dominated by charnockite hills, and relatively minor high grade metasedimentary enclaves and mafic granulites exposed in the valleys (Drury *et al.* 1984; Rameshwar Rao *et al.* 1991; Ghosh *et al.* 2004). Structurally, the Salem Block and the Dharwar Craton are characterised by dominantly NNW–SSE to N–S fabrics (Bhaskar Rao *et al.* 2003; Chetty *et al.* 2003) that are deflected into ~E–W orientations

in close proximity and within shear zones in the northern most PCSS (Ghosh *et al.* 2004). Workers have investigated the protolith ages of charnockitic and felsic gneisses throughout the Salem Block using U-Pb zircon geochronology and have obtained dominantly Mesoarchaean-Neoarchaean ages ranging from *ca.* 3000–2530 Ma (Peucat *et al.* 1993; Raith *et al.* 1999; Mojzsis *et al.* 2003; Ghosh *et al.* 2004; Clark *et al.* 2009a; Sato *et al. in press*).

The Salem Block underwent regional amphibolite-granulite facies metamorphism in the Neoarchaean-early Palaeoproterozoic. Current age constraints for this metamorphic event range from *ca.* 2530–2450 Ma (Peucat *et al.* 1993; Raith *et al.* 1999; Mojzsis *et al.* 2003; Clark *et al.* 2009a; Sato *et al. in press*) using zircon and monazite geochronology. In addition, some workers suggest that the southern Salem Block experienced subsequent Neoproterozoic metamorphic/deformation events in close proximity to, or within, the northern bounding PCSS shear zones, evidenced by Sm–Nd garnet mineral geochronology yielding ages of *ca.* 600 Ma (Meißner *et al.* 2002), monazite U-P ages of *ca.* 610 Ma (Ghosh *et al.* 2004) and Rb–Sr biotite mineral geochronology yielding ages of *ca.* 550–600 Ma, which were interpreted to represent cooling ages (Meißner *et al.* 2002). Previous workers have investigated the pressure temperature conditions of the middle to southern Salem Block using various thermometers and barometers and have reported an increase in grade from amphibolite facies to granulite facies progressing southwards. The range of pressure-temperature estimates for granulite facies rocks in the south of the Salem Block are ~700–900 ºC and ~5–10 kbar (Harris *et al.* 1982; Janardhan *et al.* 1982; Hansen *et al.* 1984; Raase *et al.* 1986; Rameshwar Rao *et al.* 1991; Hansen & Newton 1995).

2.3 The Kanja Malai Hills

The Kanja Malai Hills are located in the south of the Salem Block and on the northern margin of the PCSS (Fig. 1.c), and have been interpreted to be located within the 3–4 km wide E–W Moyar-Attur Shear Zone (Ghosh *et al.* 2004). The Moyar-Attur Shear Zone represents the interpreted northern boundary of the PCSS, and contrasts with the prominent northeast-southwest orientated structures to the north and directly south of the Salem area. The Kanja Malai Hills contains interlayered mafic granulites, BIF, granitic gneisses and metapelites (Ghosh *et al.* 2004; Santosh *et al.* 2009; Santosh *et al.* 2010; Sato *et al. in press*). Sato et al. (*in press*) recently investigated the age of magmatism and metamorphism using zircon U-Pb geochronology of a granitic gneiss, obtaining ages of ~2650 Ma and ~2450 Ma respectively. *P-T* conditions during metamorphism at Kanja Malai were estimated by Santosh et al. (2010), who interpreted retrograde *P-T* conditions of ~750 ºC and < 7.4 kbar using thermobarometry, and 1000 ºC and 9–12 kbar during apparent decompression at peak temperature from fluid inclusion density analyses. However, Santosh et al. (2010) attributed these *P-T* conditions to an early Cambrian metamorphic event based on ~540 Ma U–Pb ages obtained by Collins et al. (2007a) and Santosh et al. (2006) further south in the PCSS, rather than Palaeoproterozoic U–Pb ages obtained by Sato et al. (*in press*).

This project aims to refine the southern boundary of the Salem Block and constrain the timing and conditions of metamorphism by using the first combined zircon, *in situ* monazite geochronological, *P-T* phase diagram and conventional thermobarometric dataset in the Salem Block.

3. FIELD AREA AND LITHOLOGICAL RELATIONSHIPS

The Kanja Malai Hills are a 25 km^2 east-west trending ridge (11°37’50”–11°37’30” N, 78°02’50”–78°03’20” E). An area of approximately 1km^2 was mapped in detail in the northern Kanja Malai Hills that preserves mafic and felsic migmatitic, magnetite-quartz mylonitic and felsic proto mylonitic gneisses (Fig. 2.a). Structurally-constrained samples were collected from this area. A steeply dipping to vertical east-west to northeast-southwest trending gneissic foliation occurs throughout the area (Fig. 2.b), accompanied by moderately east plunging mineral elongation lineations in higher strain zones, and occasionally in lower strain mafic lithological layers (Fig. 2.c). Strain partitioning into high-strain zones that vary from 5 cm wide discrete shear bands (Fig 3.d) to 20 m wide east-west trending shear and proto-mylonitic zones are evident. These zones are characterised by grain size reduction, and enhanced preferred mineral orientation. Kinematic indicators preserved in higher strain domains indicate north block to the east tectonic transport. These kinematic indicators include S-C’ fabrics preserved in the high strain quartz and magnetite mylonitic shear zone (Fig. 3.e).These higher strain domains are bound by relatively lower strain stromatic migmatites (Fig 3.b).

S1 and S2 exists within all garnet-bearing mafic gneisses and felsic gneisses, with the exception of one felsic gneiss unit that only exhibits S2 ~E–W trending foliation (Fig. 3.c). Within lower strain polyphase deformational gneisses, closed–tight upright migmatitic folds with steep west-plunging hinges are pervasively found with wavelengths from 5 cm to 2 m (Fig. 3.b). In higher strained proto-mylonitic felsic gneisses, folds are dominantly upright tight-isoclinal (Fig. 3.g), with east to north-east

gently-moderately plunging hinges that are parallel to the mineral elongation lineation. These folds have wavelengths between 50 cm–2 m and deform S1 and leucosomes. Features of main lithologies are summarised in Table 1.

Due to the intensity of the deformation at Kanja Malai, there is limited preservation of primary lithological relationships between mafic and felsic lithologies. However, a 1 m wide boudinaged mafic gneiss intrudes a migmatitic gneiss (sample JA14), and one contact was observed showing a mafic gneiss lens obliquely cross cutting felsic gneiss foliation, indicating that mafic gneiss lithologies intruded felsic lithologies (Fig. 3h).

4. MINERAL PETROLOGY

Samples were taken from an approximately 1km^2 area in the northern Kanja Malai Hills. Samples can be distinguished into groups defined by similar petrological features and relationships. These groups represent the main lithological units present in the northern Kanja Malai Hills used for analysis in this study. Samples can be ascribed to three groups: 1) amphibolite-granulite garnet bearing mafic assemblages, 2) kyanite-garnet bearing felsic granulites, and 3) felsic granulites. Petrological descriptions of eight samples are grouped into these three petrological groups described below.

4.1 Kyanite and garnet bearing felsic gneisses

4.1.1 SAMPLE JA3 AND JA7

Samples JA3 and JA7 were taken from kyanite, garnet, biotite plagioclase, K-feldspar, quartz gneisses (Fig. 3.f) in the northern Kanja Malai Hills that preserve folded S1 and planar E-W trending S2 foliation. Medium to coarse grained subhedral porphyroblastic garnet (2–5 mm in diameter), fine to medium grained bladed kyanite (≤ 2 mm in diameter), fine to coarse grained subhedral to anhedral, platy to equant plagioclase, K-feldspar and quartz grains (0.5–6 mm), fine to medium grained biotite (1–3 mm along longest axis) and rare fine grained, euhedral rutile (≤ 2 mm) define the peak metamorphic assemblage, and are usually found in direct contact with each other (Fig. 4.a). A well-developed gneissosity is defined by biotite grains. Garnet grains are typically fractured and contain equant very fine quartz inclusions, and are commonly partially separated from plagioclase, K-feldspar and quartz by a very fined grained corona of biotite. Kyanite grains always occur next to garnet grains and exist

predominantly in strain shadows. However, garnet and kyanite grains may be separated by a very fine corona of biotite. Locally, layers of fine grained equant plagioclase, K-feldspar and quartz grain bands, alternating with layers of very fine to fine grained biotite grains wrap around garnet and coarse grained plagioclase, K-feldspar and quartz grains (Fig. 4.b). Myrmekitic quartz/plagioclase textures are observed in some grains.

4.2 Garnet bearing mafic gneisses

Garnet bearing mafic gneisses (Fig. 3.a) were taken from a prominent ridge in the north of the Kanja Malai Hills mapped area.

4.2.1 SAMPLE JA9A

Medium to coarse grained, equant porphyroblastic garnet (up to 10 mm), medium grained subhedral clinopyroxene grains (2–4 mm in diameter), medium grained, anhedral equant to platy plagioclase and hornblende grains (2–3 mm long), fine grained euhedral rutile (up to 2 mm) and anhedral ilmenite comprise the interpreted peak assemblage (Fig. 4.c). Foliation is defined by hornblende and plagioclase. Garnet grains are usually in contact with clinopyroxene, and are often also in contact with plagioclase and hornblende grains. Garnet and clinopyroxene-rich domains of approximately 20 mm in diameter occur, with garnet and generally clinopyroxene-poor domains outside these pods containing dominantly plagioclase and hornblende grains. Clinopyroxene grains are sometimes present in plagioclase-hornblende rich domains surrounded by plagioclase and hornblende grains. Rutile grains always occur next to ilmenite grains and typically occur on clinopyroxene-plagioclase grain boundaries. Ilmenite sometimes exists without rutile, and interpreted post peak magnetite never exists with rutile, with

both single ilmenite and magnetite grains occurring along grain boundaries and in garnet and clinopyroxene inclusions in contact with fractures.

4.2.2 SAMPLE EM16 AND JA10

Coarse grained, porphyroblastic garnet (up to 20 mm), subhedral equant to platy medium grained clinopyroxene (2–4 mm), anhedral medium grained plagioclase (3 – 5 mm), anhedral fine grained quartz (1 mm), fine to coarse grained anhedral ilmenite (1–5 mm) and medium grained anhedral hornblende (only for JA10) define the peak assemblage (Fig. 4.d,e,f). Foliation is not apparent in these samples. Garnet grains are always in direct contact with and are typically partially to completely surrounded by clinopyroxene, in addition to containing anhedral clinopyroxene inclusions. Clinopyroxene grains can exhibit needle laminae (commonly in clinopyroxene inclusions in garnet) that are parallel to cleavage. Ilmenite is fine grained in EM16 and only occurs at grain boundaries or in garnet and clinopyroxene grains when in contact with fractures, whereas ilmenite is fine to coarse grained in JA10 and is commonly in contact with garnet. Quartz is typically restricted to inclusions in garnet and along grain boundaries. No amphibole was observed in EM16. However, very fine amphibole growth may exist at some clinopyroxene, garnet and plagioclase grain boundaries. Rare fine grained (<2 mm) hornblende is observed in JA10 and is restricted to occurring next to clinopyroxene and ilmenite grains. Rare fine grained anhedral apatite occurs in contact with garnet and clinopyroxene grains.

4.2.3 SAMPLE EM19

Porphyroblastic coarse grained garnet (up to 20 mm), subhedral medium grained, equant to prismatic clinopyroxene (2–4 mm), anhedral medium to coarse grained platy plagioclase (4–7 mm), medium grained subhedral to anhedral hornblende (up to 4 mm) and occasional euhedral fine to medium grained rutile and anhedral fine to medium grained quartz (1–3 mm) comprise the interpreted peak assemblage (Fig. 4. g). Foliation is defined by hornblende and plagioclase grains. Garnet porphyroblasts occur next to clinopyroxene, plagioclase and hornblende grains but are always separated by a thin (0.5 mm width) corona of very fine grained actinolite-magnesiohornblende. Garnet grains are only in direct contact with clinopyroxene when clinopyroxene exists as fine to medium grained inclusions in garnet. Fractures in garnet grains are also filled by fine-grained actinolite-magnesiohornblende. Hornblende and plagioclase grains more commonly occur next to each other but are always separated by very fine grained actinolite-magnesiohornblende. Fine grained magnetite grains ($\leq$ 2 mm in diameter) occur dominantly along garnet-clinopyroxene grain boundaries and in contact with fractures in garnet.

4.3 Felsic gneisses

4.3.1 SAMPLE JA13 AND JA14

Medium grained garnet (up to 3 mm in diameter), fine to medium grained anhedral quartz, plagioclase and K-feldspar and fine grained anhedral ilmenite are interpreted to comprise the peak assemblage (Fig. 4.h). Garnet grains contain occasional quartz inclusions and occur next to quartz, plagioclase and K-feldspar grains. Garnet grains are commonly isolated from plagioclase and K-feldspar grains by a corona of fine-grained

biotite. Biotite is only present around and in contact with garnet grains. Very fine to fine, randomly oriented acicular muscovite grains have overgrown plagioclase and K-feldspar grains, however original grain boundary orientations and twinning of plagioclase and K-feldspar can still be at least partially observed in most of these interpreted relic grains. Ilmenite occurs along quartz boundaries and within plagioclase/muscovite aggregate grains.

5. MINERAL CHEMISTRY

Mineral chemistry was obtained on a Cameca SX51 electron microprobe (EPMA) at Adelaide Microscopy, University of Adelaide. A beam current of 20 nA and an accelerating voltage of 15 kV was used to obtain spot analyses and spot traverses of minerals. Elemental maps were obtained using an accelerating voltage of 15 kV and 100 nA, using WDS spectrometers for Fe, Mg, Ca and Mn. A representative summary of mineral chemistry of samples is presented in Table 2–3. Symbols used: $X_{Fe} = Fe^{2+}/(Fe^{2+} + Mg)$, $X_{Mg} = Mg/(Fe^{2+} + Mg)$, $X_{Alm} = Fe^{2+}/(Fe^{2+}+Mg+Ca+Mn)$, $X_{Py} = Mg/(Fe^{2+}+Mg+Ca+Mn)$, $X_{Grs} = Ca/(Fe^{2+}+Mg+Ca+Mn)$, $X_{Spss} = Mn/(Fe^{2+}+Mg+Ca+Mn)$, $X_{Ab} = Na/(Na+Ca)$, $X_{An} = Ca/(Na+Ca)$, $X_{Or} = K/(K+Na)$, Fsp: $X_K = K/(K+Ca+Na)$, Fsp $X_{Na} = Na/(K+Ca+Na)$, Fsp $X_{Ca} = Ca/(K+Ca+Na)$, $X_{Al} = Al/(Al+Fe^{3+}+2Ti)$.

5.1 Garnet bearing mafic gneiss samples

5.1.1 GARNET

Garnet grains from mafic gneiss samples show compositional zonation trends with some degree cation proportion variation for different samples, quantified by traverses across grains. Zoning profiles are characterised by increasing X_{Alm} values from the core to the rim (c = cores, r = rims: EM16 c = ~0.57, r = ~0.59, EM19 c = ~0.49, r = ~0.52, JA10 c = ~0.60, r = ~0.70, JA9a c = ~0.58, r = ~0.59). X_{Py} typically displays an inverse X_{Alm} zonation pattern and decreases from the core to the rim (EM16 c = ~0.22, r = ~0.18, EM19 c = ~0.32, r = ~0.29, JA10 c = ~0.22, r = ~0.18, JA9a c = ~0.31, r = ~0.26). X_{Grs} increases from core to rim (EM16 c = ~0.18, r = ~0.22, EM19 c = ~0.17, r = ~0.19, JA10 c = ~0.17, r = ~0.21, JA9a c = ~0.16, r = ~0.20). X_{Spss} is low and ranges from

0.009–0.017 for mafic gneiss samples. A general trend of increasing X_{Spss} core to rim is observed in sample EM19 when garnet is in contact with actinolite-magnesiohornblende (c = ~0.009, r = ~0.017). No trend in X_{Spss} is evident in samples JA9a, JA10 and EM16.

5.1.2 FELDSPAR

Plagioclase in garnet bearing mafic gneiss samples are typically sodic, with X_{An} ranging from 0.38–0.53 for sample JA10, 0.37–0.43 for sample EM16, 0.39–0.50 for sample JA9a and 0.36–0.47 for sample EM19. X_{An} decreases from core to rim in plagioclase grains that are in contact with garnet (c = ~0.48, r = ~0.41 for JA9a). X_{Or} are for the above samples are low and range from 0.003–0.017.

5.1.3 CLINOPYROXENE

Clinopyroxene in JA9a has X_{Fe} values ranging from 0.163–0.312, with recalculated Fe^{3+} cation amounts ranging between 0–0.165 for an oxygen formula unit, Al_2O_3 wt. % values between 2.12–4.72 and Na_2O wt. % between 0.74–1.09. In JA10, clinopyroxene inclusions are typically more magnesian (X_{Fe} = 0.250–0.314, recalculated Fe^{3+} cations = 0.067–0.127, Al_2O_3 = 3.1–3.2 wt. %, Na_2O = 0.86–1.11wt. %) than clinopyroxene occurring among garnet domains interpreted to be included in the peak assemblage (X_{Fe} = 0.251–0.466, recalculated Fe^{3+} cations= 0.077–0.152, Al_2O_3 = 2.67–4.06 wt. % and Na_2O = 0.93–1.07 wt. %). Similarly for sample EM19, clinopyroxene inclusions within garnet are slightly more magnesian (X_{Fe} = 0.183–0.190, recalculated Fe^{3+} cations = 0.062–0.080, Al_2O_3 = 3.400–4.210 wt. % and Na_2O = 0.540–0.960 wt. %) than clinopyroxene interpreted to be part of the peak assemblage (X_{Fe} = 0.194–0.281, recalculated Fe^{3+} cations = 0.039–0.102, Al_2O_3 = 3.79–4.26 wt. % and Na_2O = 0.50–

0.90 wt. %). In EM16, there is no distinct trend between clinopyroxene inclusions in garnet and interpreted peak assemblage clinopyroxene (inclusion: X_{Fe} = 0.310–0.382, recalculated Fe^{3+} cations = 0.057–0.088, Al_2O_3 = 2.95–3.68 wt. % and Na_2O = 0.74–0.97 wt. %, peak: X_{Fe} = 0.347–0.356, recalculated Fe^{3+} cations = 0.094–0.121, Al_2O_3 = 3.03–3.59 wt. % and Na_2O = 0.76–1.01 wt. %).

End member proportions of all clinopyroxene analyses were determined using software program AX (Powell *et al.* 1998). Clinopyroxene in all garnet-mafic rocks are dominantly diopside (JA9a: X_{Jd} = 0.020–0.068, X_{Di} = 0.695–0.897, X_{Hd} = 0.036–0.246 and X_{Ag} = 0.001–0.045; JA10: X_{Jd} = 0.020–0.0457, X_{Di} = 0.578–0.786, X_{Hd} = 0.161–0.363 and X_{Ag} = 0.018–0.039, EM16; X_{Jd} = 0.022–0.052, X_{Di} = 0.646–0.805, X_{Hd} = 0.131–0.293 and X_{Ag} = 0.017–0.041, EM19; X_{Jd} = 0.025–0.049, X_{Di} = 0.722–0.865, X_{Hd} = 0.078–0.220 and X_{Ag} = 0.002–0.026).

5.1.4 AMPHIBOLE

Following the classification methodology and names of Leake *et al.* (1997), amphibole in JA9a has $(Ca + Na)_B$ ranging from 1.788–1.919 and Na_B ranging from 0–0.133 per formula unit (pfu), and is member of the calcic group, defined by $(Ca + Na)_B \geq 1.50$ and $Na_B < 0.50$ pfu. Similarly, amphibole in JA10 and EM19 are calcic with $(Ca + Na)_B$ ranging from 1.936–1.948 and 1.760–1.880 and Na_B ranging from 0.033–0.077 and 0–0.010 pfu respectively. The capability to classify amphiboles into subdivisional groups defined by Leake *et al*. (1997) is somewhat limited due to the inability of the EPMA to distinguish cation oxidation state proportions (e.g., Fe^{3+}, Fe^{2+}). In addition, the presence of OH^-, Fl^- or Cl^- in amphibole results in the extreme difficulty in estimating Fe^{3+}

cations. Therefore, in order to minimise errors associated with uncertainty of Fe^{3+} and Fe^{2+}, amphibole has been classified into subdivisional groups based on unknown Fe^{3+} and Fe^{2+} proportions. Amphibole in sample JA9a is classified along the magnesiohornblende–tschermakite and edenite–pargasite/magnesiohastingsite boundaries ($(Na + K)_A$ = 0.414–0.612, X_{Mg} = 0.668–0.751, Si = 6.370–6.774). In JA10, amphibole is pargasite-magnesiohastingsite ($(Na + K)_A$ = 0.709–0.742, X_{Mg} = 0.393–0.409, Si = 6.313–6.409). Medium–coarse grained amphibole in EM19 is magnesiohornblende–edenite ($(Na + K)_A$ = 0.428–0.542, X_{Mg} = 0.675–0.720, Si = 6.540–6.809), whereas very fine to fine grain amphibole is classified as magnesiohornblende-actinolite that typically rims garnet and clinopyroxene ($(Na + K)_A$ = 0.086–0.280, X_{Mg} = 0.699–0.782, Si = 7.050–7.700). Ti ranges from 0.1837–2.101 pfu for JA9a, 0.152–0.227 pfu for JA10 and 0.007–0.191 pfu for EM19.

5.1.5 ILMENITE

Mn content in ilmenite ranges from 0.09–0.11 wt. % for JA10, 0.11–0.16 wt. % for JA9a and 0.02–0.15 wt. % for EM16. Recalculated Fe^{3+} cations = 0.041–0.066 for JA9a, 0.135–0.199 for JA10 and 0.142–0.211 for EM16.

5.1.6 MAGNETITE

In sample EM19, Al content in magnetite ranges from 0.02–0.07 wt. %, which corresponds to X_{Al} of 0.001–0.002. Sample JA9a contains no Al content above the minimum detection limit of the EPMA.

5.2 Kyanite-garnet bearing felsic gneiss samples

5.2.1 GARNET

Samples JA3 and JA7 display compositional zonation profiles that have an increase in X_{Fe} from core to rim (c = core, r = rim, JA3 c = ~0.58 r = ~0.67, JA7 c = ~0.63, r = ~0.65), similarly an increase in X_{Alm} from core to rim (JA3 c = ~0.57, r = ~0.61, JA7 c = ~0.57, r = ~0.59) a decrease in X_{Py} from core to rim that is inverse to X_{Alm} (JA3 c = ~0.37, r = ~0.25, JA7 c = c = ~0.33, r = ~0.28), an increase in X_{Grs} from core to rim (JA3 c = ~0.07, r = ~0.12, JA7 c = ~0.09, r = ~0.13) and low X_{Spss} values that typically increases slightly from core to rim when in contact with biotite (JA3 c = ~0.004, r = ~0.007, JA7 c = ~0.012, r = ~0.016). Figure 5 shows an elemental map for garnet in JA3.

5.2.2 FELDSPAR

Samples JA3 and JA7 both contain K-rich alkali feldspar and plagioclase. In sample JA3, plagioclase has similar proportions of Ca and Na in the core, with X_{Ca} and X_{Na} values of ~0.49. Towards the rim X_{Ca} decreases (~0.40), whereas X_{Na} increases (~0.58). X_K is low and typically decreases slightly from core (~0.080) to rim (~0.012). K-rich alkali feldspar has X_K ranging from ~0.91–0.92, and is Ca poor with X_{Ca} of ~0.003–0.04.

Sample JA7 has plagioclase with a zonation profile trend similar to sample JA3, whereby X_{Na} increases from core (~0.55) to rim (~0.66), and X_{Ca} decreases from core (~0.44) to rim (~0.34). Plagioclase is X_K poor, and increases slightly from core (~0.011)

to rim (~0.016). In K-rich alkali feldspar, X_K ranges from 0.91–0.92, with a low X_{Ca} of ~0.001.

5.2.3 BIOTITE

In sample JA3, X_{Mg} has a range of 0.70–0.726 and a Ti content between 3.4 and 4.15 wt. %. Biotite in sample JA7 is slightly less magnesian X_{Mg} has a range of 0.627–0.632 and 0.34–3.52 wt. %. Al content in biotite ranges from 15.84–16.07 wt. % in JA3 and 16.52–17.01 wt. % in JA7.

6. OUTLINE OF ANALYTICAL TECHNIQUES

6.1 Quantified metamorphic analysis- *P-T* pseudosections and conventional thermobarometry

Phase equilibria and conventional thermobarometry (average *P-T*) have been employed in this study to delineate the thermal and physical *P-T* conditions of metamorphism in the Kanja Malai Hills. The integration of this data with zircon and *in situ* monazite geochronology can allow temporal constraints to be placed on the high grade metamorphism in the southern Salem Block. Forward model phase equilibria (phase diagrams) were constructed on kyanite-garnet bearing gneiss samples JA3 and JA7. Phase diagrams are not suitable to use for *P-T* analysis of high grade mafic rocks showing evidence for partial melting, as a thermodynamic model for mafic melt compositions does not exist (Powell & Holland 2008). As a result, conventional thermobarometry has been used for obtaining *P-T* constraints on three garnet bearing mafic gneiss samples (JA9a, JA10 and EM19).

Whole rock geochemical analysis was used to determine the bulk composition of sample JA3 and JA7 because they were considered homogeneous at the scale of the sample size. The Electron microprobe was used to obtain spot chemical analyses for phase diagram compositional isopleths of sample JA3 and JA7, and minerals that are considered to have once been in equilibrium with each other in samples JA9a, JA10 and EM19 for thermobarometry calculations. Analytical procedures for phase diagram calculation and conventional thermobarometry estimates are provided in Appendix II.

6.2 Zircon and monazite geochronology and zircon trace and REE chemistry

U-(Th)-Pb geochronology was conducted using the Laser Ablation Inductively Coupled Plasma Mass Spectrometer (LA-ICP-MS) at Adelaide Microscopy, University of Adelaide. The primary aim of geochronology was to determine the age of metamorphism at Kanja Malai. *In situ* monazite grains were used in order to allow age data to be related to microstructural relationships within the rock (e.g. Kelsey *et al.* 2007; Cutts *et al. in press*). Monazite, when combined with zircon geochronology can allow more robust age constraints on metamorphism and the nature of metamorphism to be established. These geochronometers have inherently different growth behaviour systematics in melt bearing systems (Kelsey *et al.* 2008), and so integrating and comparing zircon and monazite geochronology can be useful when constraining the timing of metamorphism and possibility of polymetamorphism. Zircon Th/U trace element and REE data was obtained to investigate the link between zircon ages, timing of metamorphism and growth of silicate metamorphic minerals (e.g. Rubatto 2002). Zircon internal morphological descriptions are provided in Appendix I, and analytical procedures for U-(Th)-Pb zircon and monazite geochronology, and zircon trace and REE data are provided in Appendix II.

7. RESULTS

7.1 *P-T* pseudosections

P-T pseudosections were constructed for two garnet-kyanite felsic gneiss samples, JA3 and JA7 as such rock compositions are conducive to graphical *P-T* analysis. Figure 6.a shows the *P-T* pseudosection calculated for JA3, contoured for garnet modal proportions (gt = 0.05, 0.1) and biotite modal proportions (bi = 0.01, 0.03, 0.05, 0.07). In Fig. 6.b, compositional isopleths are calculated for X_{Alm} = 0.45, 0.5, 0.55, 0.6, 0.65, 0.7, X_{Grs} = 0.1, 0.15, 0.2, 0.25, 0.3 and X_{An} = 0.35, 0.4, 0.45, 0.5. *P-T* pseudosection constructed for JA7 is shown in Fig. 7.a showing contours calculated for garnet modal proportions (gt = 0.01, 0.05, 0.1) and biotite modal proportions (0.01, 0.03, 0.05). Figure 7.b shows compositional isopleths of X_{Grs} = 0.1, 0.15, 0.2, 0.25, X_{Alm} = 0.6, 0.65, 0.7, 0.75 and X_{An} = 0.35, 0.4.

In JA3, garnet modal proportions broadly decrease down pressure and temperature, from 0.1 to 0.03. Biotite modal proportions increase down pressure and temperature, from 0.01 to 0.07. X_{Grs} increases with increasing pressure and decreasing temperature from 0.1 to 0.3. X_{An} increases with decreasing pressure and temperature from 0.35 to 0.5, and X_{Alm} increases with decreasing temperature from 0.45 to 0.7. In sample JA7, garnet modal proportions decrease with decreasing pressure and temperature from 0.1 to 0.01. Biotite modal proportions increase with decreasing pressure and temperature from 0.01 to 0.05. Compositional isopleths for X_{Grs} increase with increasing pressure and decreasing temperature, from 0.1 to 0.25. X_{Alm} increases with decreasing temperature from 0.6 to 0.75. X_{An} increases with decreasing pressure from 0.35 to 0.4.

7.2 Conventional thermobarometry

Samples were modelled as fluid absent, assemblages with JA9a, EM19: $a\mathrm{H_2O} = 0.5$, and JA10: $a\mathrm{H_2O} = 0.25$ reflecting the somewhat variable abundance of amphibole in samples. For sample JA9a, *P-T* estimates for $a\mathrm{H_2O} = 0$, 0.25, 0.5 all pass the χ^2 test at 95% confidence. For JA9a-2, $a\mathrm{H_2O} = 0.5$ most closely corresponds with Fe-Mg reaction thermometers, thus making it an appropriate selection for use in *P-T* estimate calculations. More ambiguity is associated with estimating $a\mathrm{H_2O}$ for JA10 because, whereas JA10-1 is relatively sensitive to $a\mathrm{H_2O}$ and only *P-T* estimates with $a\mathrm{H_2O} = 0.25$ pass the χ^2 test at 95% confidence (combined with good correspondence with Fe-Mg thermometers), JA10-2 is less sensitive to $a\mathrm{H_2O}$ variations, whereby $a\mathrm{H_2O} = 0$, 0.25, 0.5 all pass the χ^2 test at 95% confidence. Furthermore, $a\mathrm{H_2O} = 0.5$ most closely corresponds to Fe-Mg thermometers, which is at odds with analysis set JA10-1. This discrepancy can be reconciled by considering that different input compositions for minerals have been used for the two different average *P-T* calculations. For sample EM19, all *P-T* estimates except $a\mathrm{H_2O} = 0.25$ for EM19-2 pass the χ^2 test at 95% confidence. A relatively small uncertainty for both EM19-1 and EM19-2 analysis sets exists when $a\mathrm{H_2O} = 0.5$ (~890 ± 58°C, ~ 12.5 ± 1.3 kbar), and when combined with good correspondence with Fe-Mg thermometers, $a\mathrm{H_2O} = 0.5$ appears to be an appropriate estimate for use in average *P-T* calculations.

Average *P-T* estimates and $a\mathrm{H_2O}$ are summarised in Table 4 and Fig. 8 and 9. As all samples used for conventional thermobarometry were taken from a ~100m^2 area, weighted averages of estimates are presented here. A weighted average of 839 ± 42 °C (1 σ) and 11.5 ± 1.6 kbar (1 σ) was obtained using end member activities and optimal

aH_2O values as outlined previously. Barometry on samples JA3 and JA7 were calculated using garnet-kyanite-quartz-plagioclase and are superimposed on Fig. 6 and 7 and presented in Table 4.

7.3 Zircon and monazite LA-ICP-MS age data

Analytical LA-ICP-MS zircon and monazite data are provided in Table 5–9. Representation of results are presented in Fig. 10-13. Representative zircon Cathodoluminescence and monazite Backscatter-Electron images are presented in Fig. 14.

7.3.1 JA3

Age data for JA3 are plotted on a conventional concordia plot and presented in weighted average and probability density distribution plots in Fig. 10. Oscillatory zoned cores, strongly luminescent domains and weakly luminescent cores and rims were targeted for analysis. Outer rims were unable to be analysed due to the thickness of these rims being <30 µm. 89 analyses on 43 zircon grains were analysed over multiple sessions in order to minimize any inaccuracy of results due to potential variability of the LA-ICP-MS and possibility for the inaccuracy of results to exceed the uncertainty of analyses throughout a single analytical session. 19 analyses were discarded due to appreciable noise of isotopic ratio signal and limited integration time of an acceptable part of the signal (analyses discarded are denoted with $^{+}$ in Table. 5-6). Of the 70 analyses for which ages were obtained, $^{207}Pb/^{206}Pb$ ages range between 2418- 2637 Ma and concordances range between 88-111%. Two populations are apparent from Fig. 10.a at *ca.* 2485 Ma and *ca.* 2600 Ma; corresponding well with different internal zonation morphologies observed in

CL. Oscillatory zoned cores correspond to the older age population. These have a weighted mean $^{207}Pb/^{206}Pb$ age of 2607 ± 24 Ma (2σ, 100 ± 5% concordance, MSWD = 1.2, *n* = 13, Fig. 10.b,c). Weakly luminescent cores and rims correspond to the younger age population and give a weighted mean $^{207}Pb/^{206}Pb$ age of 2481 ± 22 Ma (2σ, 100 ± 5% concordance, MSWD = 1.8, *n* = 20, Fig. 10.d,e). No trend could be determined for strongly luminescent featureless domains, however these domains have an age range between 2421–2539 Ma.

7.3.2 JA13

Conventional concordia, probability density distribution and weighted average plots for sample JA13 are presented in Fig. 11. 41 analyses were conducted on 36 grains targeting weakly-moderately oscillatory and concentric zoned luminescent cores, weakly luminescent featureless cores and weakly luminescent rims. Two analyses were discarded due to short integration time of an acceptable part of the isotopic signal. $^{207}Pb/^{206}Pb$ isotopic ages for analyses range from 2356 ± 36–2662 ± 40 Ma (2σ) and concordances range from 60–104%. Two populations exist for JA13, with a younger peak at *ca.* 2490 Ma and an imprecise older peak at *ca.* 2635 Ma (Fig. 11a). Analyses conducted on concentric zoned cores, weakly luminescent featureless cores and weakly luminescent rims correspond to the younger age population and analyses with 100 ± 10% concordance yield a $^{207}Pb/^{206}Pb$ weighted average of 2488 ± 14.8 Ma (2σ MSWD of 1.16, *n* = 27, Fig. 11.b,c). Only three analyses on oscillatory zoned cores were possible because of the small size of the cores (Fig. 11.d). These cores give ages of (2662 ± 39 Ma, 2631 ± 36 Ma and 2593 ± 36 Ma, 2 σ). A Pb loss trend with >10%

discordance exists for seven analyses. These analyses correspond with weakly luminescent featureless cores and are often surrounded by chaotic internal features.

7.3.3 JA14

49 analyses on 40 zircon grains were conducted over multiple LA-ICP-MS sessions and targeted weakly luminescent cores, strongly luminescent domains and weakly luminescent rims. Age data is presented in conventional concordia, probability density distribution weighted average plots in Fig. 12. Analyses yielded a $^{207}Pb/^{206}Pb$ age range from 2425 ± 34 Ma–2537 ± 36 Ma (2σ) and a concordance range from 94–116%. Different internal features observed under CL did not correspond with any distinctive age patterns and one age population exists at *ca.* 2490 Ma. The $^{207}Pb/^{206}Pb$ age weighted average for 100 ± 10% concordant analyses is 2493 ± 12 Ma (2σ MSWD = 1.4, n = 46). Given that the internal morphology analysed in this sample is typical of morphological features observed in metamorphic growth or recrystallisation of zircon (Corfu et al., 2003), the quoted weighted average age is the best estimation for the age of metamorphism for this sample.

7.3.4 JA7

Conventional concordia, weighted average and probability distribution plots for monazite analyses of sample JA7 are provided in Fig 13. 16 analyses on 16 monazite grains were conducted targeting both light and dark domains. Three analyses were discarded due to variable nature of the isotopic signal and inability for a portion of the signal with a sufficient integration time to be selected. Despite heterogeneous internal morphologies and variations in textural relationships of monazite grains to other

minerals, one age population is apparent. 13 analyses have $^{207}Pb/^{206}Pb$ ages that range from 2426 ± 34–2509 ± 45 Ma (2σ) and 97–102% concordancy. A weighted average $^{207}Pb/^{206}Pb$ age of 2467 ± 20 Ma (2σ) and MSWD of 1.11 was yielded from 13 analyses. The quoted weighted average is the best estimate for metamorphism for this sample and is consistent with the interpreted metamorphic ages yielded by zircon samples.

7.4 Zircon chemistry

7.4.1 ZIRCON U-TH-PB CHEMISTRY

Plots of ^{238}U versus ^{232}Th and $^{207}Pb/^{206}Pb$ versus $^{232}Th/^{238}U$ are presented in Fig. 15 for all analysed zircon samples (JA3, JA13, JA14). Data are divided into analyses of key CL features exhibited by zircon grains in each sample.

Oscillatory zoned cores of sample JA3 (kyanite-garnet bearing gneiss) preserve ~350 ppm U and 90 ppm Th concentrations, and have $^{232}Th/^{238}U$ ratios that range from 0.03–1.49 and average of ~0.40. Analyses of strongly luminescent, featureless domains have ~140 ppm U, ~30 ppm Th, and $^{232}Th/^{238}U$ ratios that range from 0.06–0.55, with a markedly lower average $^{232}Th/^{238}U$ ratio of ~0.21, compared to oscillatory cores. Weakly luminescent domain analyses have ~260 ppm U and ~30 ppm Th concentrations, and varying $^{232}Th/^{238}U$ ratios from 0.02–0.48, that are on average (avg. $^{232}Th/^{238}U = 0.13$) substantially lower than oscillatory cores and strongly luminescent, featureless domains. Although there is no definitive correspondence between CL features and Th or U, a positive correlation exists between Th and U for all data for sample JA3 (Fig. 15.a). A broad positive trend exists between $^{232}Th/^{238}U$ ratio and

$^{207}Pb/^{206}Pb$ age, whereby older cores generally have higher $^{232}Th/^{238}U$ ratios, and younger weakly luminescent domains have lower $^{232}Th/^{238}U$ ratios. Strongly luminescent featureless domains tend to occupy the transition between older Th enriched oscillatory cores and younger, Th depleted weakly luminescent domains (Fig. 15.b).

Sample JA13 displays interpreted inherited oscillatory zoned cores, concentric zoned cores, weakly luminescent cores and weakly luminescent rims. Three oscillatory zoned inherited cores were analysed and have ~100 ppm U, ~50 ppm Th (Fig. 15.c) and $^{232}Th/^{238}U$ ratios of 0.46, 0.53 and 0.57, which are distinct from other analyses when these core are plotted on $^{232}Th/^{238}U$ against $^{207}Pb/^{206}Pb$ age (Fig. 15.d). Concentric zoned cores preserve ~200 ppm U values and ~80 ppm Th values, and $^{232}Th/^{238}U$ ratios that range from 0.22–0.54 (avg. = 0.38). Weakly luminescent cores have ~350 ppm U and ~50 ppm Th and have a range of $^{232}Th/^{238}U$ from 0.01–0.42 with a lower ratio average of avg. = 0.22 in comparison to the ratio average of concentric zoned cores. Similarly, rims have ~300 ppm U and ~30 ppm Th, with $^{232}Th/^{238}U$ ratios lower than concentric zoned and weakly luminescent cores (0.01–0.31, avg. = 0.12). Represented in Fig 15.d, a transitional decrease in $^{232}Th/^{238}U$ ratios is observed from concentric zoned cores to weakly luminescent cores and rims, however all analyses fall into one $^{207}Pb/^{206}Pb$ age bracket with (*ca.* 2450–2530 Ma) with no distinct trend between $^{232}Th/^{238}U$ ratios and $^{207}Pb/^{206}Pb$ age, with the exception of the interpreted inherited cores.

Analyses of JA14 (Fig. 15.e,f) have been divided into cores, rims and strongly luminescent, featureless domains. Cores preserve ~400 ppm U and ~70 ppm Th and have a wide range of $^{232}Th/^{238}U$ ratios between 0.08–0.65 (avg. = 0.37). Strongly luminescent featureless domains have ~250 ppm U and ~70 ppm Th, with varying $^{232}Th/^{238}U$ ratios from 0.04–0.94, with a slightly larger ratio average when compared to cores (avg. = 0.47). Rims of sample JA14 have ~350 ppm U and ~30 ppm Th and distinctly lower $^{232}Th/^{238}U$ values than cores and strongly luminescent domains (0.03–0.10, avg. = 0.07).

7.4.2 ZIRCON REE CHEMISTRY

Chondrite normalised zircon REE analyses are presented in Table 10. Sample JA14 (Fig. 16.a) has zircon grains with ΣREE = ~790–2300 ppm. The chondrite normalised REE patterns for these zircon cores are characterised by steep LREE patterns (Sm_n/La_n = 84.80–271.96, avg. = 165.60), enrichment of HREE (Lu_n/Sm_n = 80.59–173.01, avg. = 142.23), a positive Ce anomaly (Ce/Ce* = 31.42–97.56, avg. = 68.24) and negative Eu anomaly (Eu/Eu* = 0.04–0.19, avg. = 0.08), whereby $Ce/Ce^* = Ce_n/\sqrt{(La_n \times Pr_n)}$, $Eu/Eu^* = Eu_n/\sqrt{(Sm_n \times Gd_n)}$ (Taylor & McClennan 1985) and $_n$ denotes the element has been chondrite normalised. In comparison to cores, zircon rims of sample JA14 display variably steep LREE patterns (Sm_n/La_n = 13.92–633.85, avg. = 261.65), are less enriched in HREE (Lu_n/Sm_n = 26.15–151.19, avg. = 71.54), have a variable positive Ce anomaly (Ce/Ce* = 7.98–128.27, avg. = 66.12) and slightly less pronounced negative Eu anomaly (Eu/Eu* = 0.045–0.40, avg. 0.14).

Sample JA3 (Fig. 16.b) have zircon grains with ΣREE = 810.69–3042.83 ppm. Zircon oscillatory zoned cores show chondrite normalised patterns that are characterised by moderate LREE slopes (Sm_n/La_n = 8.27–43.14, avg. = 17.06), HREE enrichment (Lu_n/Sm_n =45.77–188.77, avg. = 96.47), a moderately positive Ce anomaly (Ce/Ce* = 4.14–94, avg. = 6.32), and a negative Eu anomaly (Eu/Eu* = 0.17–0.25, avg. = 0.24). Weakly luminescent domains (cores and rims) exhibiting internal morphologies typical of solid state recrystallisation (e.g. 'ghost zoning', Hoskin & Black 2000) have LREE slopes of Sm_n/La_n = 4.10–67.71 (avg. = 20.66), variable but on average less HREE enriched slopes compared to oscillatory zoned cores (Lu_n/Sm_n = 9.23–188.74, avg. = 73.18), with a variable small to large positive Ce anomaly (Ce/Ce* = 2.52–14.66, avg. = 5.55), and variable negative Eu anomaly (Eu/Eu* = 0.44–0.77, avg. = 0.35). Weakly luminescent domains (cores and rims) that do not show solid state recrystallisation features have variable LREE slopes (Sm_n/La_n =7.57–91.45, avg. =26.06), HREE of Lu_n/Sm_n = 16.22–59.24 (avg. = 32.04), with a variable Ce positive anomaly (Ce/Ce* = 1.99–43.03, avg. = 10.41) and a less pronounced negative Eu anomaly compared to oscillatory zoned cores and interpreted solid state recrystallisation domains (Eu/Eu* = 0.14–0.92, avg. = 0.54).

8. DISCUSSION

This study has focused on examining the timing and conditions of metamorphism of the Kanja Malai Hills, in the southern Salem Block and in the northern PCSS along the Moyar-Attur Shear Zone. The timing and conditions of metamorphism of the Kanja Malai Hills have significant implications for refining the northern extent of Neoproterozoic-Cambrian metamorphism within the PCSS, southern extent of the Archaean-Palaeoproterozoic metamorphosed Salem Block and constraining the physical conditions experienced during metamorphism. The following discussion will address the implications of the results of the timing and conditions of metamorphism for the Salem Block, and compare these to the early Palaeoproterozoic metamorphic rock record.

8.1 Interpretation of zircon and monazite ages

8.1.1 ZIRCON AGES AND CHEMISTRY

There is an increasing amount of work integrating zircon morphology, trace element, REE and geochronological data to determine the link between zircon U-(Th)-Pb age and metamorphic paragenesis (e.g. Rubatto 2002; Hermann & Rubatto 2003; Harley & Kelly 2007; Rubatto & Hermann 2007; Clark *et al.* 2009b). The combination of these tools are particularly useful when examining the timing and *P-T* conditions of granulite facies metamorphism, as it can allow the U-(Th)-Pb age preserved in zircon to 1) be ascribed to a metamorphic event, and 2) be correlated relative to metamorphic mineral assemblage evolution.

Analyses of zircon with internal morphologies characteristic of metamorphic growth in JA3, JA13 and JA14 (weakly luminescent rim overgrowths, weakly luminescent concentric zoned cores, Hoskin & Schaltegger, 2003) and metamorphic isotopic modification, such as solid state recrystallisation in samples JA3 and JA14 (weakly luminescent domains preserving 'ghost zoning', strongly luminescent featureless domains, Hoskin & Black, 2000) yield ages that are statistically indistinguishable between *ca.* 2480-2490 Ma. This age is considered to be the age of the high grade metamorphic event at Kanja Malai. Sample JA13 is characterised by an E-W trending foliation (S2) and is interpreted to be localised remelting of migmatitic gneiss JA14, as there is no distinct structural or lithological boundary between the units. Sample JA13 is structurally interpreted to be the youngest unit at Kanja Malai, and considered to be a discrete leucosome of JA14. It is therefore possible that this age is also dating the timing of remelting and generation of E-W (S2) fabric throughout the bulk of the Kanja Malai Hills at *ca.* 2490 Ma if this foliation formed coevally with metamorphism.

Oscillatory zoned cores in JA3, characteristic of zircon crystallisation of an igneous protolith (Vavra 1994; Corfu *et al.* 2003a; Hoskin & Schaltegger 2003) give a distinctly older age of *ca.* 2610 Ma. This age is interpreted to represent either the age of felsic magmatism at Kanja Malai or age of magmatism in the source region of detritus. This age is slightly younger than the age of magmatism obtained from a granitic gneiss by Sato *et al.* (*in press*) of *ca.* 2647 Ma at the Kanja Malai Hills, and possibly reflects multiple pulses of felsic magmatism, although it cannot be discounted that the age of magmatism/source magmatism in this study may not reflect the true age of magmatism, given that cores show evidence for slight isotopic mobilisation (e.g. faded zoning).

A number of authors have documented a decrease in Th/U ratios between primary igneous and metamorphic zircon (Rubatto 2002; Hoskin & Schaltegger 2003). Additionally, Th/U ratios have been reported to decrease during solid state recrystallisation, typically as a result of expulsion of the more incompatible Th ion from the crystal lattice during recrystallisation (Hoskin & Black 2000). The assignment of the above morphologies to either igneous or metamorphic genesis is generally supported by larger Th/U ratios for oscillatory zoned cores, and smaller Th/U ratios for weakly luminescent domains. Oscillatory zoned cores in sample JA3 show a range in Th/U ratios (avg. ~0.40) that are typically lower than the conventional cut off for igneous zircon (>0.5, Hoskin & Schaltegger, 2003). However, the Th/U ratios of these cores are generally substantially greater than Th/U ratios for weakly luminescent domains (avg. ~0.13). The observation that the core Th/U ratios are lower than conventional ratios may be a result of partial solid state recrystallisation processes during metamorphism resulting in some degree of isotopic disturbance, which is evidenced by faded zoning and the presence of transgressive recrystallisation fronts at the boundaries of some cores (Hoskin & Black 2000). Strongly luminescent featureless domains in sample JA3 do not show any distinct Th/U or age trends and may be a result of differential retention of the igneous protolith zircon isotopic composition during recrystallisation. There are no distinct Th/U ratio populations for concentric zoned cores and rims in sample JA13, and this may reflect that both that concentric zoned cores and rims are characteristic internal morphologies formed during high grade metamorphism (see Corfu *et al.* 2003a).

REE analyses of metamorphic cores and rims of sample JA14 have strong HREE enrichment slopes that suggest that zircon grew in the absence of garnet during

metamorphism (Rubatto 2002). This interpretation is consistent with the relative lack of garnet in the rock (< 1%). The strong negative Eu anomaly indicates that the crystallisation of metamorphic cores probably occurred during the presence of an Eu depleted melt, possibly as a result of crystallising feldspar scavenging Eu. The presence of the negative Eu anomaly in rims may indicate the presence of an Eu depleted melt given that the morphologies of the rims are typical for zircon formed during high grade metamorphism in the presence of melt (Corfu *et al.* 2003a). However, the commonly preserved negative Eu anomaly in crustal zircon may also be caused by the reduced Eu^{2+} state that is typically incompatible in the zircon crystal lattice (Hoskin & Schaltegger, 2003). Kelsey et al. (2008) showed that zircon growth above the solidus is likely to only occur at or after peak metamorphism (peak temperature). Given the ages obtained for cores and rims are identical within uncertainty and in consideration of the above points, the age recorded by zircon in JA14 is interpreted to be recording high grade peak or post peak metamorphism during anatexis.

In sample JA3, the consistent HREE enriched pattern exhibited by oscillatory zoned cores and substantial negative Eu anomaly indicates that crystallisation of these cores occurred in absence of garnet from an Eu depleted melt, probably from feldspar crystallising (Rubatto 2002; Hoskin & Schaltegger 2003). Weakly luminescent domains (both cores and rims) in JA3, separated into domains that show a presence or absence of characteristic solid state recrystallisation textures (e.g. ghost zoning), have variable LREE enrichment, positive Ce and negative Eu anomalies and HREE enrichment. The slight reduction in HREE slope and chondrite normalised abundance for solid state recrystallised domains, in comparison to oscillatory zoned cores of JA3 may indicate

that zircon underwent solid state recrystallisation in the presence of garnet (Rubatto 2002). Given that slope of HREE is only slightly flatter than oscillatory cores in JA3, it is interpreted that these solid state recrystallised zircon domains underwent HREE diffusional competition with garnet but didn't approach equilibrium because HREE depletion is not close to that expected from zircon/garnet REE equilibrium experiments (Rubatto 2002). This is also consistent with the preservation of features such as 'ghost zoning', which indicate a lack of equilibration of the zircon domains with melt. The slight reduction of the negative Eu anomaly in solid state recrystallised domains similarly may be explained by the lack of chemical communication between these domains and Eu depleted melt. The slightly more enriched average LREE compared to oscillatory zoned cores is at odds with the notion that solid state recrystallisation typically expels impurities from the crystal lattice, such as the larger and more incompatible LREE (Hoskin & Black 2000). This relative slight LREE enrichment may be influenced by one heavily enriched LREE analysis (Fig.16.b), and is likely to be an overestimation of LREE.

The observation that the undifferentiated weakly luminescent domains with no solid state recrystallisation features are heavily LREE enriched, relative to oscillatory cores is peculiar in respect to both solid state recrystallisation (see above) and typical zircon REE signatures for sample JA3. It is possible that the highly enriched LREE of these domains may be due to the incorporation of micro-inclusions of a mineral with LREE affinity (e.g. monazite) during crystallization or protolith crystallisation, depending on if these domains indeed underwent solid state recrystallisation, or represent metamorphic growth. The flat average HREE slope is influenced by Sm being relatively enriched and

chondrite normalised concentrations of HREE are similar to those of oscillatory zoned cores, indicating that these domains probably did not form in the presence of with garnet, and therefore these zones may represent new growth in the presence of melt.

An imprecise discordia chord of seven weakly luminescent featureless cores, surrounded by chaotic internal morphology in JA14 is likely to have resulted from metamictisation due to an initial greater concentration of Th and U. It is possible that Pb loss of these metamict cores were facilitated by Neoproterozoic-Cambrian metamorphic/shearing event in the PCSS, particularly due to the location of the Kanja Malai Hills in the Moyar-Attur Shear Zone, for which mineral resetting has been proposed to occur in the Neoproterozoic (Meißner *et al.* 2002). If the metamictisation of these cores were due to a Neoproterozoic-Cambrian imprint, such an imprint probably was relatively minor as any evidence for isotopic resetting after the ~2470-2490 Ma high grade metamorphic event is limited to these seven cores.

8.1.2 MONAZITE AGES

Monazite grains were analysed in sample JA7 and preserve $^{207}Pb/^{206}Pb$ age of ~2470 Ma. At granulite facies conditions, monazite grains typically record an age along the metamorphic *P-T* path (Rubatto *et al.* 2001; Rubatto *et al.* 2006). Earlier authors have interpreted that under high temperature conditions, U-Pb age of monazite typically represents the timing of the rocks passing down through closure temperatures of ~700 °C (Parrish 1990; Dahl 1997; Vavra & Schaltegger 1999; Rubatto *et al.* 2001). More recent work has suggested that monazite has closure temperatures- not dissimilar to zircon (e.g. closure temperature of 950 ºC for a 20 µm diameter monazite at 10 ºC/Ma,

Cherniak & Watson 2000; Cherniak *et al.* 2004). The commonly observed younger U-Pb age recorded by monazite, when compared to zircon has been proposed to be more likely to be due to differences between the age and temperature at which monazite and zircon began growing (Kelsey *et al.* 2008). Taking this into account, the monazite age of ~2470 Ma is interpreted to be representative of monazite growth during metamorphism, most likely on the retrograde path. There is no systematic U-Pb age relationship between monazite located texturally within garnet and monazite located in the quartz, plagioclase and K-feldspar matrix, and this is considered to be due to monazite growing in garnet and the matrix over a time scale shorter than the resolution of the LA-ICP-MS.

8.1.3 AGE OF METAMORPHISM

Monazite in sample JA7 yield the same age, within uncertainty, as zircon samples JA3, JA13 and JA14 (JA7= 2467 ± 20 Ma, JA3 = 2481 ± 24 Ma, JA14 = 2493 ± 12 Ma, JA13 = 2488 ± 14.8 Ma, all uncertainties are 2 σ). The timing of high grade peak to post-peak metamorphism and anatexis is therefore interpreted to have occurred between ~2470-2490 Ma. For the purposes for simplifying an approximate age of metamorphism, the above zircon and monazite ages yield a $^{207}Pb/^{206}Pb$ weighted average of 2486 ± 16 Ma (2 σ, MSWD = 1.7). This weighted average will be used here on, but is not meant to imply that zircon and monazite ages from these samples are necessarily recording the same section of the metamorphic path. Although the growth systematics between zircon and monazite can differ significantly during granulite facies metamorphism, the geochronological techniques used here do not allow the timing of peak and retrograde metamorphism to be distinguished.

8.2 Conditions of metamorphism

The *P-T* phase diagrams of kyanite-garnet bearing gneisses JA3 and JA7, when superimposed, constrain peak *P-T* conditions defined by the garnet, kyanite, biotite, plagioclase, rutile, K-feldspar, quartz, liquid interpreted peak assemblage to 800-850 ºC and 14-16 kbar (Fig. 7.c). Conventional thermobarometric estimates of garnet bearing mafic gneiss samples yield a weighted average temperature of 839 ± 42 ºC, and pressure of 11.5 ± 1.6 kbar (1 σ) (Fig. 9). Both conventional thermobarometry *P-T* estimate methods yield similar temperatures of ~800–850 °C. This consistency of conventional thermobarometry temperature estimates with phase diagram peak stability fields indicate that there was limited diffusion of minerals during cooling.

In contrast to peak temperatures, conventional thermobarometry estimates yield pressures that are 1–6 kbar lower than pressures obtained from superimposed peak stability fields of phase diagrams. It is beyond the scope of this study to discuss the largely unquantifiable inherent uncertainties associated with each thermobarometric method (e.g. see Bégin & Pattison 1994; Powell & Holland 2008), but considering that phase diagram equilibria and average *P-T* conventional thermobarometry employed this study are fundamentally dependent on different input compositional information (whole rock composition versus individual mineral spot chemical analyses respectively), a discrepancy in *P* resulting from differences in compositional information is worthwhile investigating.

Variation between pressure for average *P-T* conventional thermobarometry and *P-T* phase equilibria estimates may be attributed to minerals compositionally recording different parts of the *P-T* path. Several authors (e.g. Pattison & Bégin 1994; Pattison *et al.* 2003; Hauzenberger *et al.* 2005) have shown that prograde and peak metamorphic zoning characteristics of minerals can often undergo complete re-equilibration or resetting along the retrograde path, thus effectively erasing the chemistry and chemical zonation signatures of prograde and peak metamorphism. In addition, decoupling of faster diffusing elements (e.g. Fe-Mg) relative to slower diffusing (e.g. Al, Si, Ca), particularly during granulite facies metamorphism can lead to element zonation recording different stages of the *P-T* path (e.g. Fitzsimons & Harley 1994; Pattison & Bégin 1994; Pattison *et al.* 2003).

The compositional zoning profiles of garnet have increasing X_{Fe} zoning from core to rim, a feature that is typically associated with retrograde metamorphism (e.g. Pattison & Bégin 1994). Ca zoning of garnet and plagioclase in garnet bearing mafic gneiss and kyanite-garnet gneiss samples do not record typical retrograde compositional profiles like Fe and Mg and, although the zoning of Ca in garnet and plagioclase may reflect a decoupling of Ca from garnet Fe and Mg (Spear 1993; Fitzsimons & Harley 1994; Indares *et al.* 2008), or for garnet, a breakdown of surrounding minerals, these possibilities are only speculative. It is unlikely however that the chemical compositional zoning of Fe, Mg and Ca in garnet represent peak *P-T* conditions, and this is a probable explanation for the lower *P* yielded by conventional thermobarometry.

Inferring a *P-T* path for the granulite facies metamorphic event at Kanja Malai is difficult because there is an absence of mineral microstructures that allow reactions to be confidently surmised (Vernon 1996). Whereas phase diagram compositional isopleths, corresponding to measured compositional data and conventional thermobarometry are particularly susceptible to recording compositional features that are not reflective of peak or retrograde *P-T*, relative trends in modal proportions, corresponding to mineral volume percent trends are more likely to be representative of peak-retrograde *P-T* conditions for minerals interpreted to comprise the peak metamorphic assemblage (e.g. Stuwe & Powell 1995; Kelsey *et al.* 2003). Garnet and biotite modal proportions were calculated for JA3 and JA7. Garnet modal proportions for JA7 and JA3 respectively broadly correspond with estimates of garnet volume percent in each sample and decrease down pressure and temperature (Fig. 6.a, 7.a). Conversely, biotite modal proportions correspond to estimated biotite volume percent in JA3 and JA7 and increase down pressure and temperature. A slight increase in abundance of biotite as a result of secondary biotite growth around the rims of garnet from the breakdown of garnet is consistent with the modal abundance trends, and may indicate a decrease in *P*. The breakdown of garnet rims when in direct contact with secondary biotite is also evidenced by a slight increase in Mn, thus garnet volume percent is a minimum. This means that calculated pressures represent *minimum* peak pressure.

Given that the grossular-kyanite-plagioclase-quartz (GASP) barometer of kyanite-garnet gneiss samples JA3 and JA7, have a slope that crosses relative decreasing garnet modal proportions in both JA3 and JA7, increasing X_{Grs} in JA7, and is relatively parallel to X_{Grs}

in JA3 from ~850 °C down temperature, it is possible that the rocks at Kanja Malai experienced a *P-T* cooling path at a slope relatively parallel to the GASP barometer slope. Such a path would allow Ca in garnet to increase, and a decrease in garnet modal proportion down temperature after decompression. As mentioned above, compositional isopleth trends for granulite facies rocks should be treated with caution, and so the above *P-T* characteristics are thus presented only as a possibility.

It is possible to propose broad *P-T* path characteristics for the metamorphic event at Kanja Malai, whereby peak metamorphism was attained at 800-850 ºC and at least 14-16 kbar, given by superimposed peak mineral assemblage fields and modal proportions of minerals in phase diagrams for samples JA3 and JA7. Although there is no unique interpretation applicable to each set of data, combined data phase diagram and conventional thermobarometry are most likely to represent decompression of 1-6 kbar following peak *P-T* at ~14-16 kbar, 800-850 ºC.

8.3 A polymetamorphic terrane?

The reported Neoproterozoic-Cambrian garnet, biotite and monazite mineral ages within the southern Salem Block and along shear zones along the northern PCSS has lead to the suggestion that the Salem Block has experienced polymetamorphism to some extent (Bhaskar Rao *et al.* 1996; Ghosh *et al.* 2004). Despite field evidence for two deformation events, the suggestion of a polymetamorphosed terrane is not supported by chemical or isotopic data found in this study. Compositional zoning in all garnet grains preserve smooth profiles with no sharp zonation trends or obvious deflections that might be expected in polymetamorphic terrains (e.g. Cutts *et al.* 2010). The possibility

that there has been complete resetting of all Fe, Mg, and Ca in garnet grains during a second metamorphic event is possible, however zircon and monazite data preserve only one Palaeoproterozoic metamorphic event. In order for there to be more than one metamorphic event and be consistent with the data above, it would require the occurrence of two metamorphic events in the Palaeoproterozoic that were separated by a time scale shorter than the resolution of the LA-ICP-MS (~30-40 Ma).

8.4 Refinement of the conditions of the early Palaeoproterozoic high grade metamorphic event in the Salem Block

Constraints on the timing of metamorphism of the Kanja Malai Hills obtained in this study at ~2490 Ma overlap within uncertainty with U-Pb zircon metamorphic ages obtained at Kanja Malai by Sato *et al.* (*in press*) at ~2450 Ma, and are in agreement with the age of high grade metamorphism reported by Clark et al. (2009a). There is some disparity between U-Pb zircon ages from previous authors in the Salem Block (~2450-2530 Ma, Peucat *et al.* 1993; Raith *et al.* 1999; Mojzsis *et al.* 2003) and it is unclear whether this is a true geological expression or due to differences in analytical methods. The broadly consistent Palaeoproterozoic age of metamorphism obtained in this study confirms that the Kanja Malai Hills belong to the Salem Block (i.e. the metamorphosed Dharwar Craton).

The *P-T* estimates of peak metamorphism of ~800-850 ºC, and ~14-16 kbar at the Kanja Malai Hills obtained in this study are substantially higher in pressure than pre-existing *P-T* estimates in the Salem Block (~700-900, 5-10 kbar, Harris *et al.* 1982; Janardhan *et al.* 1982; Hansen *et al.* 1984; Raase *et al.* 1986; Rameshwar Rao *et al.* 1991; Hansen &

Newton 1995). The conventional thermobarometric methods employed by previous studies are fundamentally dependent on compositional mineral chemistry and rely on the assumption that preserved compositions in minerals are the same as they were at peak *P-T* conditions (see the above discussion on conventional thermobarometry results). It is quite probable that resetting and possible decoupling of mineral chemical zoning has resulted in estimates from these previous studies being reflective of *P-T* along the retrograde path during decompression rather than peak metamorphism.

Taking the above into account, the most robust method to obtain peak *P-T* estimates for the high grade metamorphic event in the Salem Block is through the construction of phase diagrams (i.e. phase diagrams generally have a first order dependence on bulk composition rather than mineral composition, Powell & Holland 2008). This study is the first to use quantitative phase equilibria to estimate the conditions of Palaeoproterozoic metamorphism in the Salem Block, and from the points discussed above, the estimates of 800-850, ~14-16 kbar obtained in this study are considered to be the best estimate of the conditions of peak metamorphism. These peak conditions significantly contribute to the understanding of the regional Palaeoproterozoic metamorphic event in the Salem Block, and notably reveal that pressures experienced by these granulite facies rocks are markedly higher than has been previously estimated.

8.5 Tectonic implications for the Southern Granulite Terrane

The Southern Granulite Terrane records a diverse tectonothermal history spanning from the Latest Archaean-Early Palaeoproterozoic to the Cambrian (Collins *et al.* 2007a; Santosh *et al.* 2008; Clark *et al.* 2009b), which, despite extensive research is not fully understood. The results of this study have direct implications for refining the areal extent of tectonometamorphic events in the SGT and the associated crustal blocks and structures. The age of high *P-T* metamorphism found in this study at ~2490 Ma indicates that the early Palaeoproterozoic metamorphosed Salem Block extends at least as far south as the Kanja Malai Hills.

The location of the Kanja Malai Hills within the Moyar-Attur Shear Zone (Ghosh *et al.* 2004) on the northern boundary of the PCSS is significant because it allows the geochronological results obtained in this study to place a northern areal limit for the high grade Neoproterozoic-Cambrian metamorphism reported in the PCSS (Bhaskar Rao *et al.* 1996; Meißner *et al.* 2002; Collins *et al.* 2007a; Santosh *et al.* 2008; Clark *et al.* 2009b). The absence of substantial evidence for a Neoproterozoic-Cambrian overprint suggests that the northern limit of this metamorphic event lies further south. This is at odds with studies that report Neoproterozoic metamorphism/deformation ages at or in close proximity to the Kanja Malai Hills or within the Moyar-Attur Shear Zone (Harris *et al.* 1996; Meißner *et al.* 2002; Ghosh *et al.* 2004; Santosh *et al.* 2010) and it is possible that this Neoproterozoic overprint is limited to higher strain partitioned areas within the 3-4 km wide shear zone. Given that the structurally youngest unit at Kanja Malai is an interpreted leucosome that records ~2490 Ma metamorphism and E-W

trending S2 foliation, it is possible that the regional E-W trending fabric around the Moyar-Attur Shear Zone (northern PCSS) may have at least originated from this high *P-T* Palaeoproterozoic metamorphic event.

Two of the current outstanding ambiguities surrounding the tectonothermal history of the SGT are the age and nature of PCSS. Two main recent interpretations of the PCSS exist: 1) that the PCSS represents a Cambrian suture zone (Meißner *et al.* 2002; Collins *et al.* 2007a; Santosh *et al.* 2009; Clark *et al.* 2009a), and 2) that the PCSS is Archaean crust that has been reworked in the Palaeoproterozoic and Neoproterozoic (Harris *et al.* 1994; Bhaskar Rao *et al.* 1996; Chetty *et al.* 2003; Ghosh *et al.* 2004; Chetty & Bhaskar Rao 2006b), with the terrane boundary not the PCSS but located further south into the Madurai Block (Bhaskar Rao *et al.* 2003; Ghosh *et al.* 2004). The results of this study do not conclusively support any one model, but do show that the following should be taken into account when assessing such models.

1) The high *P-T ca.* 2490 Ma metamorphic event may have been associated with E-W trending fabrics that are typically attributed to be a feature of the PCSS. If these E-W fabrics formed synchronously with the *ca.* 2490 Ma high *P-T* metamorphic event, it suggests that either these fabrics may predate the PCSS if it is a suture zone associated with Cambrian amalgamation, or that at least the Moyar-Attur Shear zone in the north of the PCSS was initially a Palaeoproterozoic structure.
2) The results of this study provide no evidence that the Kanja Malai Hills represent ocean plate stratigraphy associated with a Cambrian suture (e.g.

Santosh *et al.* 2009) and any Cambrian suture zone would have existed south of the Kanja Malai Hills, further within the PCSS.

8.6 Comparisons of high *P* metamorphism in the early Palaeoproterozoic

The metamorphic rock record through time provides us with a window to evaluate the secular changes in geodynamic processes through Earth history (Brown 2007a; Brown 2007b). In the following, we are concerned with the early rock record from Archaean-Palaeoproterozoic and briefly outline the contrasts between the characteristic metamorphic conditions recorded during this time and the *P-T* estimates obtained in this study. The Archaean rock record is characterised by ubiquitous granulite facies (e.g. Harley 1989; Pattison *et al.* 2003), low-to moderate-*P* metamorphism with thermal gradients of ~75 °C/kbar (Brown 2007a). There is no recorded evidence for high pressure granulites or eclogite facies rocks until the late Mesoarchaean (Mints *et al.* 2010), and no evidence for blueschist or ultra high pressure metamorphism (excluding xenoliths) until the Neoproterozoic (Maruyama *et al.* 1996). Even in the Neoarchaean-Palaeoproterozoic, high-pressure metamorphic rocks are extremely rare. There is general consensus among the geological community that an early Earth would have been secularly hotter, with higher mean mantle temperature and higher heat production (Brown 2007a).

Eclogite facies rocks and high pressure granulites (~750-1000 ºC, ~1.5->2.5 Ga) are a phenomenon related to subduction and collision typically in the Proterozoic-Phanerozoic rock record (Brown 2007a). The thermal gradients needed to form and preserve these rocks occur in terrane-accretion orogenic systems (e.g. Ota *et al.* 2004b)

and collisional plate orogenic systems, such as subduction-to-collision systems predominately in the Phanerozoic (e.g. Liou *et al.* 2004).

The *P-T* estimates of peak metamorphism obtained in this study are high pressure granulites, near eclogite facies at ~800–850 ºC, ~14–16 kbar. For the purposes of comparing these estimates to other *P-T* estimates during the Palaeoproterozoic-Archaean, these peak *P-T* estimates correspond to an average apparent thermal gradient of ~17 °C/km (not meant to imply a linear increase of temperature with depth). The peak *P-T-t* estimates obtained from this study are unusual, and plot at higher pressures and lower thermal gradients than most 2400-3500 Ma high grade *P-T* metamorphic estimates (Fig. 17.a,b). The few eclogite facies rocks preserved the Archaean-earliest Palaeoproterozoic metamorphic record have been attributed to have formed via subduction processes operating on some scale during the earlier Earth (Collins *et al.* 2004; Ota *et al.* 2004a; Volodichev *et al.* 2004; Mints *et al.* 2010). Whether the scarcity of these eclogite facies rocks reflects the secularly different geodynamic processes operating during the Archaean-early Palaeoproterozoic compared to modern day process (Brown 2007b; Brown 2007a), or the lack of preservation of these assemblages in the rock record remains unclear. Nevertheless, this study provides a foundation for future work to investigate the areal extent and possible tectonothermal mechanisms for obtaining and preserving these high pressures both regionally in the Salem Block, and on a global scale during the Archaean-early Palaeoproterozoic.

9. CONCLUSIONS

The main findings of this study are:

1. The Kanja Malai Hills underwent high grade metamorphism and anatexis during the earliest Palaeoproterozoic (*ca.* 2.49 Ga).
2. Palaeoproterozoic metamorphism at Kanja Malai indicates that the Salem Block (Dharwar Craton) extends at least to the northern PCSS.
3. Peak *P-T* conditions of the southern Salem Block metamorphism were ~800–850 °C and ~14–16 kbar, and may have been followed by decompression and relatively fast cooling.
4. There is no evidence for a Neoproterozoic-Cambrian overprint at Kanja Malai, and any suture zone would lie further south of Kanja Malai within the PCSS.
5. The peak *P-T* estimates recorded by the southern Salem Block are anomalously high pressure when compared to the other Neoarchaean-Palaeoproterozoic metamorphosed terranes in the rock record. The peak *P-T* estimates obtained in this study require thermal regimes typical of those generated at convergent plate boundaries.

ACKNOWLEDGEMENTS

I would like to firstly thank my supervisors Alan Collins, Martin Hand and David Kelsey, who have been an invaluable source of knowledge and guidance. I would also like to thank Justin Payne who has provided a great deal of help throughout the year, which I am very grateful for. I am also very appreciative of the analytical guidance and patience provided by Angus Netting and Ben Wade at Adelaide Microscopy throughout the year. A big thank you to Kathryn Cutts for her help and wisdom on all things metamorphic. I would also like to acknowledge that this project was funded by a joint Australian-Indian research grant, and would like to thank M. Santosh, T. Chetty, D. Mohanty and V. Siva for their kind hospitality while in India. Diana, Libby, Steph and Will: for being great field buddies, and for all the India and various other conversations. I would like to thank my family and friends for their support this year. Finally, to everyone in room 211: this year wouldn't have been the same without you.

9. REFERENCES

ALEINIKOFF J., SCHENCK, W., PLANK, M., SROGI, L., FANNING, C., KAMO, S. AND BOSBYSHELL, H. 2006. Deciphering igneous and metamorphic events in high-grade rocks of the Wilmington Complex, Delaware: Morphology, cathodoluminescence and backscattered electron zoning, and SHRIMP U-Pb geochronology of zircon and monazite. *Geological Society of America Bulletin* **118**, 39-64.

BARTLETT J. M., DOUGHERTY-PAGE J. S., HARRIS N. B. W., HAWKESWORTH C. J. & SANTOSH M. 1998. The application of single zircon evaporation and model Nd ages to the interpretation of polymetamorphic terrains: an example from the Proterozoic mobile belt of south India. *Contributions to Mineralogy and Petrology* **131**, 181-195.

BÉGIN N. J. & PATTISON D. R. M. 1994. Metamorphic evolution of granulites in the Minto Block, northern Québec: extraction of peak P-T conditions taking account of late Fe-Mg exchange. *Journal of Metamorphic Geology* **12**, 411-428.

BHASKAR RAO Y. J., CHETTY T. R. K., JANARDHAN A. S. & GOPALAN K. 1996. Sm-Nd and Rb-Sr Ages and P-T History Of the Archean-Sittampundi and Bhavani Layered Meta-Anorthosite Complexes In Cauvery Shear Zone, South-India - Evidence For Neoproterozoic Reworking Of Archean Crust. *Contributions to Mineralogy and Petrology* **125**, 237-250.

BHASKAR RAO Y. J., JANARDHAN A. S., VIJAYA KUMAR T., NARAYANA B. L., DAYAL A. M., TAYLOR P. N. & CHETTY T. R. K. 2003. Sm-Nd model ages and Rb-Sr isotope systematics of charnockites and gneisses across the Cauvery Shear Zone, southern India: implications for the Archaean-Neoproterozoic boundary in the southern granulite terrain. *In:* Ranmakrishnan M. ed., *Tectonics of Southern Granulite Terrain*, pp 297-317, Geological Society of India Memoir 50.

BRAUN I., CENKI-TOK B., PAQUETTE J.-L. & TIEPOLO M. 2007. Petrology and U-Th-Pb geochronology of the sapphirine-quartz-bearing metapelites from Rajapalayam, Madurai Block, Southern India: Evidence for polyphase Neoproterozoic high-grade metamorphism. *Chemical Geology* **241**, 129-147.

BRAUN I., MONTEL J. M. & NICOLLET C. 1998. Electron microprobe dating monazites from high-grade gneisses and pegmatites of the Kerala Khondalite Belt, southern India. *Chemical Geology* **146**, 65-85.

BROWN M. 2007a. Metamorphic conditions in orogenic belts: a record of secular change. *International Geology Review* **49**, 193-234.

BROWN M. 2007b. Metamorphism, Plate Tectonics, and the Supercontinent Cycle. *Earth Science Frontiers* **14**, 1-18.

CHERNIAK D. J. & WATSON E. B. 2000. Pb diffusion in zircon. *Chemical Geology* **172**, 5-24.

CHERNIAK D. J., WATSON E. B., GROVE M. & HARRISON T. M. 2004. Pb diffusion in monazite: a combined RBS/SIMS study. *Geochimica et Cosmochimica Acta* **68**, 829-840.

CHETTY T. R. K. & BHASKAR RAO Y. J. 2006a. Constrictive deformation in transpressional regime: field evidence from the Cauvery Shear Zone, Southern Granulite Terrain, India. *Journal of Structural Geology* **28**, 713-720.

CHETTY T. R. K. & BHASKAR RAO Y. J. 2006b. Strain pattern and deformational history in the eastern part of the Cauvery shear zone, southern India *Journal of Asian Earth Sciences* **28**, 46-54.

CHETTY T. R. K., BHASKAR RAO Y. J. & NARAYANA B. L. 2003. A structural cross section along Krishnagiri-Palani Corridor, Southern Granulite Terrain of India. *In:* Ramakrishnan M. ed., *Tectonics of Southern Granulite Terrain*, pp 255-278, Geological Society of India, Memoir 50.

CLARK C., COLLINS A. S., SANTOSH M., TAYLOR R. & WADE B. P. 2009b. The P-T-t architecture of a Gondwanan suture: REE, U-Pb and Ti-in-zircon thermometric

constraints from the Palghat Cauvery shear system, South India. *Precambrian Research* **174**, 129-144.

CLARK C., COLLINS A. S., TIMMS N. E., KINNY P. D., CHETTY T. R. K. & SANTOSH M. 2009a. SHRIMP U-Pb age constraints on magmatism and high-grade metamorphism in the Salem Block, southern India. *Gondwana Research* **16**, 27-36.

COLLINS A. S., CLARK C., PLAVSA D., AMARASINGHE U., FODEN J., CHETTY T. R. K. & SANTOSH M. 2010. Ediacaran-Cambrian Tectonic Evolution of Southern India and Surrounding Terranes. *Indian Journal of Geoogy*, 23-40.

COLLINS A. S., CLARK C., SAJEEV K., SANTOSH M., KELSEY D. E. & HAND M. 2007a. Passage Through India: The Mozambique Ocean Suture, High Pressure Granulites and the Palghat-Cauvery Shear System. *Terra Nova* **19**, 141-147.

COLLINS A. S., REDDY S. M., BUCHAN C. & MRUMA A. 2004. Temporal Constraints on Palaeoproterozoic Eclogite Formation and Exhumation (Usagaran Orogen, Tanzania). *Earth & Planetary Science Letters* **224**, 175-192.

COLLINS A. S., SANTOSH M., BRAUN I. & CLARK C. 2007b. Age and sedimentary provenance of the Southern Granulites, South India: U-Th-Pb SHRIMP secondary ion mass spectrometry. *Precambrian Research* **155**, 125-138.

CORFU F., HANCHAR J. M., HOSKIN P. W. O. & KINNY P. D. 2003a. Atlas of zircon textures. *In:* Hanchar J. M. & Hoskin P. W. O. eds., *Zircon*, Vol. 53, pp 468-500, Mineralogical Society of America, Reviews in Mineralogy and Geochemistry, Washington, D.C.

CORFU F., RAVNA E. J. K. & KULLERUD K. 2003b. A Late Ordovician U–Pb age for the Tromsø Nappe eclogites, Uppermost Allochthon of the Scandinavian Caledonides. *Contributions to Mineralogy and Petrology* **145**, 502-513.

CUTTS K. A., HAND M. & KELSEY D. E. *in press*. Early Mesoproterozoic high-temperature granulites from the Gawler Craton, southern Australia. *Lithos*.

CUTTS K. A., KINNY P. D., STRACHAN R. A., HAND M., KELSEY D. E. & EMERY M. 2010. Three metamorphic events recorded in a single garnet: Integrated phase modelling, in situ LA-ICPMS and SIMS geochronology from the Moine Supergroup, NW Scotland. *Journal of Metamorphic Geology* **28**, 249-267.

DAHL P. S. 1997. A crystal-chemical basis for Pb retention and fission-track annealing systematics in U-bearing minerals, with implications for geochronology. *Earth and Planetary Science Letters* **150**, 277-290.

DRURY S. A., HARRIS N. B. W., HOLT R. W., REEVES-SMITH J. & WHITEMAN R. T. 1984. Precambrian tectonics and crustal evolution in south India. *Journal of Geology* **92**, 3-20.

DRURY S. A. & HOLT R. W. 1980. The tectonic framework of the south Indian craton: a reconnaissance involving LANDSAT imagery. *Tectonophysics* **65**, 1-15.

DUTCH R. A., HAND M. & KELSEY D. E. 2010. Unravelling the tectonothermal evolution of reworked Archean granulite facies metapelites using *in situ* geochronology: an example from the Gawler Craton, Australia. *Journal of Metamorphic Geology* **28**, 293-316.

FITZSIMONS I. C. W. & HARLEY S. L. 1994. The influence of retrograde cation exchange on granulite *P-T* estimates and a convergence technique for the recovery of peak metamorphic conditions. *Journal of Petrology* **35**, 543-576.

GEISLER T., PIDGEON R. T., VAN BRONSWIJK W. & PLEYSIER R. 2001. Kinetics of thermal recovery and recrystallistaion of partially metamict zircon; a Raman spectroscopic study. *European Journal of Mineralogy* **13**, 1163-1176.

GEOLOGICAL SURVEY OF INDIA 1995. *Geological and mineral map of Tamil Nadu and Pondicherry*. Bangalore.

GHOSH J. G., DE WIT M. J. & ZARTMAN R. E. 2004. Age and tectonic evolution of Neoproterozoic ductile shear zones in the Southern Granulite Terrain of India, with implications for Gondwana studies. *Tectonics* **23**, doi:10.1029/2002TC001444.

HANSEN E. C. & NEWTON R. C. 1995. Differentiation of Late Archean crust in the Eastern Dharwar Craton, Krishnagiri-Salem area. *Journal of Geology* **103**, 629.

HANSEN E. C., NEWTON R. C. & JANARDHAN A. S. 1984. Fluid inclusions in rocks from the amphibolite-facies gneiss to charnockite progression in southern Karnataka, India: direct evidence concerning the fluids of granulite metamorphism. *Journal of Metamorphic Geology* **2**, 249-264.

HARLEY S. L. 1989. The origins of granulites: a metamorphic perspective. *Geol. Mag.* **86**, 359-373.

HARLEY S. L. & KELLY N. M. 2007. The impact of zircon-garnet REE distribution on the interpretation of zircon U-Pb ages in complex high-grade terraines: An example from the Rauer Islands, East Antarctica. *Chemical Geology* **241**, 62-87.

HARRIS N. B. W., BARTLETT J. M. & SANTOSH M. 1996. Neodymium isotope constraints on the tectonic evolution of East Gondwana. *Journal of Southeast Asian Earth Sciences* **14**, 119-125.

HARRIS N. B. W., R.W. H. & DRURY S. A. 1982. Geobarometry, geothermometry, and late Archean geotherms from the granulite facies terrain of South India. *Journal of Geology* **90**, 509-527.

HARRIS N. B. W., SANTOSH M. & TAYLOR P. N. 1994. Crustal evolution in south India: constraints from Nd isotopes. *Journal of Geology* **102**, 139-150.

HAUZENBERGER C. A., ROBEL J. & STUWE K. 2005. Garnet zoning in high pressure granulite-facies metapelites, Mozambique belt, SE-Kenya: constraints on the cooling history. *European Journal of Mineralogy* **17**, 43-55.

HERMANN J. & RUBATTO D. 2003. Relating zircon and monazite domains to garnet growth zones: age and duration of granulite facies metamorphism in the Val Malenco lower crust. *Journal of Metamorphic Geology* **21**, 833-852.

HOLLAND T. & POWELL R. 2003. Activity–composition relations for phases in petrological calculations: an asymmetric multicomponent formulation. *Contributions to Mineralogy and Petrology* **145**, 492-501.

HOLLAND T. J. B. & POWELL R. 1998. An internally consistent thermodynamic data set for phases of petrological interest. *Journal of Metamorphic Geology* **16**, 309-343.

HOSKIN P. W. O. & BLACK L. P. 2000. Metamorphic zircon formation by solid-state recrystallisation of protolith igneous grains. *Journal of Metamorphic Geology* **18**, 423-439.

HOSKIN P. W. O. & SCHALTEGGER U. 2003. The composition of zircon and igneous and metamorphic petrogenesis. *In:* Hanchar J. M. & Hoskin P. W. O. eds., *Zircon*, pp 27-62, Mineralogical Society of America, Reviews in Mineralogy & Geochemistry, Volume 53, Washington, D.C.

INDARES A., WHITE R. W. & POWELL R. 2008. Phase equilibria modelling of kyanite-bearing anatectic paragneisses from the central Grenville Province. *Journal of Metamorphic Geology* **26**, 815-836.

JACKSON S. E., PEARSON N. J., GRIFFIN W. L. & BELOUSOVA E. A. 2004. The application of laser ablation-inductively coupled plasma-mass spectrometry to in-situ U/Pb zircon geochronology. *Chemical Geology* **211**, 47-69.

JANARDHAN A. S., NEWTON R. C. & HANSEN E. C. 1982. The transformation of amphibolite facies gneiss to charnockite in southern Karnataka and northern Tamil Nadu, India. *Contributions to Mineralogy and Petrology* **79**, 130-149.

KELSEY D. E., CLARK C. & HAND M. 2008. Thermobarometric modeling of zircon and monazite growth in melt-bearing systems: examples using model metapelitic and metapsammitic granulites. *Journal of Metamophic Geology* **26**, 199-212.

KELSEY D. E., HAND M., CLARK C. & WILSON C. J. L. 2007. On the application of in situ monazite chemical geochronology to constraining P-T-t histories in high-temperature (>850 degrees C) polymetamorphic granulites from Prydz Bay, East Antarctica. *Journal of the Geological Society, London* **164**, 667-683.

KELSEY D. E., WHITE R. W. & POWELL R. 2003. Orthopyroxene–sillimanite–quartz assemblages: distribution, petrology, quantitative P–T–X constraints and P–T paths. *Journal of Metamorphic Geology* **21**, 439-453.

LEAKE B., E., WOOLLEY A., R., ARPS C., E. S., BIRCH W., D., GILBERT M. C., GRICE J., D., HAWTHORNE F., C., KATO A., KISCH H., J., KRIVOVICHEV V., G., LINTHOUT K., LAIRD J., MANDARINO J., A., MARESCH W., V., NICKEL E., H., ROCK N., M. S., SCHUMACHER J., C., SMITH D., C., STEPHENSON N., C. N., UNGARETTI L., WHITTAKER E., J. W. & GUO Y. 1997. *Nomenclature of amphiboles; report of the subcommittee on amphiboles of the International Mineralogical Association, Commission on New Minerals and Mineral Names* (Vol. 1). The Canadian Mineralogist.

LIOU J. G., TSUJIMORI T., ZHANG T., KATAYAMA L. & MARUYAMA S. 2004. Global UHP metamorphism and continental subduction/collision: The Himalayan model. *International Geology Review* **46**, 1-27.

LUDWIG K. R. 2003. *User's Manual for Isoplot 3.00*. Berkeley Geochronological Center, Special Publication No.4.

MARUYAMA S., LIOU J. G. & TERABAYASHI M. 1996. Blueschists and Eclogites of the World and Their Exhumation. *International Geology Review* **38**, 485 - 594.

MEIßNER B., DETERS P., SRIKANTAPPA C. & KÖHLER H. 2002. Geochronological evolution of the Moyar, Bhavani and Palghat shear zones of southern India: implications for east Gondwana correlations. *Precambrian Research* **114**, 149-175.

MINTS M. V., BELOUSOVA E. A., KONILOV A. N., NATAPOV L. M., SHCHIPANSKY A. A., GRIFFIN W. L., O'REILLY S. Y., DOKUKINA K. A. & KAULINA T. V. 2010. Mesoarchean subduction processes: 2.87 Ga eclogites from the Kola Peninsula, Russia. *Geology* **38**, 739-742.

MOJZSIS S. J., DEVARAJU T. C. & NEWTON R. C. 2003. Ion Microprobe U-Pb Age Determinations on Zircon from the Late Archean Granulite Facies Transition Zone of Southern India. *The Journal of Geology* **111**, 407-425.

OTA T., GLADKOCHUBB D. P., SKLYAROV E. V., MAZUKABZOV A. M. & WATANABE T. 2004a. P-T history of garnet-websterites in the Sharyzhalgai complex, Southwestern margin of Siberian craton: evidence for Paleoproterozoic high-pressure metamorphism. *Precambrian Research* **132**, 327-348.

OTA T., TERABAYASHI M. & KATAYAMA I. 2004b. Thermobaric structure and metamorphic evolution of the Iratsu eclogite body in the Sanbagawa belt, central Shikoku, Japan. *Lithos* **73**, 95-126.

PARRISH R. R. 1990. U-Pb dating of monazite and its application to geological problems. *Canadian Journal of Earth Sciences* **27**, 1431-1450.

PATTISON D. R. M. & BÉGIN N. J. 1994. Zoning patterns in orthopyroxene and garnet in granulites: implications for geothermometry. *Journal of Metamorphic Geology* **12**, 387-410.

PATTISON D. R. M., CHACKO T., FARQUHAR J. & MCFARLANE C. R. M. 2003. Temperatures of granulite-facies metamorphism: Constraints from experimental phase equilibria and thermobarometry corrected for retrograde exchange. *Journal of Petrology* **44**, 867-900.

PAYNE J. L., FERRIS G., BAROVICH K. M. & HAND M. 2010. Pitfalls of classifying ancient magmatic suites with tectonic discrimination diagrams: An example from the Paleoproterozoic Tunkillia Suite, southern Australia. *Precambrian Research* **177**, 227-240.

PAYNE J. L., HAND M., BAROVICH K. M. & WADE B. P. 2008. Temporal constraints on the timing of high-grade metamorphism in the northern Gawler Craton; implications for assembly of the Australian Proterozoic. *Australian Journal of Earth Sciences* **55**, 623-640.

PEARCE N. J., PERKINS W. T., WESTGATE J. A., GORTON M. P., JACKSON S. E., NEAL C. R. & CHENERY S. P. 1997. A Compilation of New and Published Major and Trace Element

Data for NIST SRM 610 and NIST SRM 612 Glass Reference Materials. *Geostandards and Geoanalytical Research* **21**, 115-144.

PEUCAT J. J., MAHABALESHWAR B. & JAYANANDA M. 1993. Age of younger tonalitic magmatism and granulitic metamorphism in the South India transition zone (Krishnagiri area): comparison with older Peninsular gneisses from the Gorur-Hassan area. *Journal of Metamorphic Geology* **11**, 879-888.

POWELL R., HOLLAND T. & WORLEY B. 1998. Calculating phase diagrams involving solid solutions via non-linear equations, with examples using THERMOCALC. *Journal of Metamorphic Geology* **16**, 577-588.

POWELL R. & HOLLAND T. J. B. 1988. An internally consistent thermodynamic dataset with uncertainties and correlations: 3. Applications to geobarometry, worked examples and a computer program. *J. Metamorphic Geol.* **6**, 173-204.

POWELL R. & HOLLAND T. J. B. 1994. Optimal geothermometry and geobarometry. *American Mineralogist* **79**, 120-133.

POWELL R. & HOLLAND T. J. B. 2008. On thermobarometry. *Journal of Metamorphic Geology* **26**, 155-179.

RAASE P., RAITH M., ACKERMAND D. & LAL R. K. 1986. Progressive Metamorphism of Mafic Rocks from Greenschist to Granulite Facies in the Dharwar Craton of South India. *The Journal of Geology* **94**, 261-282.

RAIMONDO T. 2009. A kinematic, metamorphic, geochemical and geochronological framework for intracontinental reworking in the western Musgrave Block, Central Australia. *GSWA report*.

RAITH M. M., SRIKANTAPPA C., BUHL D. & KOEHLER H. 1999. The Nilgiri enderbites, South India: nature and age constraints on protolith formation, high-grade metamorphism and cooling history. *Precambrian Research* **98**, 129-150.

RAMESHWAR RAO D. R., NARAYANA B. L., CHARAN S. N. & NATARAJAN R. 1991. P-T conditions and geothermal gradients of gneiss-enderbite rocks: Dharmapuri area, Tamil Nadu, India. *Journal of Petrology* **32**, 539-554.

REDDY P. R., PRASAD R. B., VIJAYA RAO V., SAIN K., PRASADA RAO P., KHARE P. & REDDY M. S. 2003. Deep seismic reflection and refraction/wide-angle reflection studies along the Kuppam-Palani transect in the southern granulite terrain of India. *In:* Ramakrishnan M. ed., *Tectonics of Southern Granulite Terrain*, pp 79-106, Geological Society of India Memoir 50.

RUBATTO D. 2002. Zircon trace element geochemistry: partitioning with garnet and the link between U-Pb ages and metamorphism. *Chemical Geology* **184**, 123-138.

RUBATTO D. & HERMANN J. 2007. Experimental zircon/melt and zircon/garnet trace element partitioning and implications for the geochronology of crustal rocks. *Chemical Geology* **241**, 38-61.

RUBATTO D., HERMANN J. & BUICK I. S. 2006. Temperature and bulk composition control on the growth of monazite and zircon during low-pressure anatexis (Mount Stafford, central Australia). *Journal of Petrology* **47**, 1973-1996.

RUBATTO D., WILLIAMS I. S. & BUICK I. S. 2001. Zircon and monazite response to prograde metamorphism in the Reynolds Range, central Australia. *Contributions to Mineralogy and Petrology* **140**, 458-468.

SANTOSH M., COLLINS A. S., TAMASHIRO I., KOSHIMOTO S., TSUTSUMI Y. & YOKOYAMA K. 2006. The Timing of ultrahigh-temperature metamorphism in Southern India: U-Th-Pb electron microprobe ages from zircon and monazite in sapphirine-bearing granulites. *Gondwana Research* **10**, 128-155.

SANTOSH M., MARUYAMA S. & SATO K. 2009. Anatomy of a Cambrian suture in Gondwana: Pacific-type orogeny in southern India? *Gondwana Research* **16**, 321-341.

SANTOSH M., TAGAWA M., YOKOYAMA K. & COLLINS A. S. 2006c. U-Pb electron probe geochronology of the Nagercoil granulites, Southern India: Implications for Gondwana amalgamation. *Journal of Asian Earth Sciences* **28**, 63-80.

SANTOSH M., TSUNOGAE T., SHIMIZU H. & DUBESSY J. 2010. Fluid characteristics of retrogressed eclogites and mafic granulites from the Cambrian Gondwana suture zone in southern India. *Contributions to Mineralogy and Petrology* **159**, 349-369.

SANTOSH M., YOKOYAMA M., TSUTSUMI Y. & YOSHIKURA S.-I. 2008. Electron microprobe dating of monazites from an ultrahigh-temperature granulite in southern India; implications for the timing of Gondwana assembly. *Journal of Mineralogical and Petrological Sciences* **103**, 77-87.

SATO K., SANTOSH M., TSUNOGAE T., CHETTY T. R. K. & HIRATA T. *in press*. Laser ablation ICP mass spectrometry for zircon U-Pb geochronology of metamorphosed granite from the Salem Block: Implication for Neoarchean crustal evolution in southern India. *Journal of Mineralogical and Petrological Sciences*.

SHIMPO M., TSUNOGAE T. & SANTOSH M. 2006. First report of garnet-corundum rocks from southern India: implications for prograde high-pressure (eclogite-facies?) metamorphism. *Earth & Planetary Science Letters* **242**, 111-129.

SLÁMA J., KOSLER J., CONDON D. J., CROWLEY J. L., GERDES A., HANCHAR J. M., HORSTWOOD M. S. A., MORRIS G. A., NASDALA L., NORBERG N., SCHALTEGGER U., SCHOENE B., TUBRETT M. N. & WHITEHOUSE M. J. 2008. Plesovice zircon -- A new natural reference material for U-Pb and Hf isotopic microanalysis. *Chemical Geology* **249**, 1-35.

SPEAR F. S. 1993. *Metamorphic Phase Equilibria and Pressure-Temperature-Time Paths*. Mineralogical Society of America, Washington D.C.

STUWE K. & POWELL R. 1995. PT paths from modal proportions - application to the Koralm Complex, Eastern Alps. *Contributions to Mineralogy and Petrology* **119**, 83-93.

TAYLOR S. R. & MCCLENNAN S. M. 1985. *The continental crust: Its composition and evolution*. Blackwell Oxford.

VAN ACHTERBERGH E., RYAN C. G., JACKSON S. E. & GRIFFIN W. L. 2001. Data reduction software for LA-ICP-MS. *In:* Sylvester P. J. ed., *Laser-ablation-ICPMS in the earth sciences; principles and applications*, Vol. 29, pp 239-243, Mineralogical Association of Canada, Short Course Handbook, Ottowa.

VAVRA G. 1994. Systematics of internal zircon morphology in major Variscan granitoid types. *Contributions to Mineralogy and Petrology* **117**, 331-344.

VAVRA G. & SCHALTEGGER U. 1999. Post-granulite facies monazite growth and rejuvenation during Permian to Lower Jurassic thermal and fluid events in the Ivrea Zone (Southern Alps). *Contributions to Mineralogy and Petrology* **134**, 405-414.

VERNON R. H. 1996. *Problems with inferring P-T-t paths in low-P granulite facies rocks* (Journal of Metamorphic Geology, Vol. 14).

VOLODICHEV O. I., SLABUNOV A. I., BIBIKOVA YE V., KONILOV A. N. & KUZENKO T. I. 2004. Arkheyskiye eklogity Belomorskogo podvizhnogo poyasa, Baltiyskiy shchit. Translated Title: Archean eclogites in the Belomorian mobile belt, Baltic Shield. *Petrologiya* **12**, 609-631.

WHITE, POWELL, HOLLAND & WORLEY 2000. The effect of TiO2 and Fe2O3 on metapelitic assemblages at greenschist and amphibolite facies conditions: mineral equilibria calculations in the system K2O–FeO–MgO–Al2O3–SiO2–H2O–TiO2–Fe2O3. *Journal of Metamorphic Geology* **18**, 497-511.

WHITE R. W., POWELL R. & CLARKE G. L. 2002. The interpretation of reaction textures in Fe-rich metapelitic granulites of the Musgrave Block, central Australia: constraints from mineral equilibria calculations in the system K2O-FeO-MgO-Al2O3-SiO2-H2O-TiO2-Fe2O3. *Journal of Metamorphic Geology* **20**, 41-55.

WHITE R. W., POWELL R. & HOLLAND T. J. B. 2007. Progress relating to calculation of partial melting equilibria for metapelites. *Journal of Metamorphic Geology* **25**, 511-527.

10. FIGURE AND TABLE CAPTIONS

Figure 1. a) Location of the Southern Granulite Terrane in India, *b)* geological map of the Southern Granulite Terrane (SGT) showing dominant lithological distribution, the Palghat Cauvery Shear System (PCSS), Karur-Kamban-Painavu-Trichur Shear Zone (Ghosh *et al.* 2004), major shear zones, spatial extent of the Dharwar Craton, Salem Block, Madurai Block and Trivandrum Block (modified after Geological Survey of India 1995; Collins *et al.* 2010), *c)* regional map of the Palghat Cauvery Shear System, Moyar-Attur Shear Zone and location of Kanja Malai Hills.

Figure 2. a) Lithological map of sample collection area in the northern Kanja Malai Hills, *b)* poles to foliation (S2), and *c)* mineral elongation lineation measurements from the Kanja Malai Hills sample collection area.

Figure 3. Field photographs of *a)* garnet bearing mafic gneiss unit, *b)* migmatitic garnet-biotite bearing felsic gneiss (sample JA14), *c)* K-feldspar-biotite felsic gneiss interpreted leucosome (JA13), *d)* discrete leucosomes cross cutting S1 along antiformal fold hinges, *e)* S C' fabrics indicating north block east (photo taken facing down), *f)* garnet-kyanite bearing felsic gneiss unit (JA3), *g)* folded psammitic layer in orthopyroxene-garnet gneiss, *h)* contact between garnet bearing mafic gneiss and garnet-biotite migmatitic gneiss showing S1 folds obliquely cut by mafic gneiss unit.

Figure 4. a) Photomicrograph of sample JA3 showing garnet surrounded by biotite and in contact with kyanite, and matrix of quartz, plagioclase and K-feldspar, *b)* photomicrograph sample JA7 of coarse grained quartz, K-feldspar and plagioclase

grains surrounded by biotite, *c)* photomicrograph of sample JA9a showing garnet rich domain in contact with clinopyroxene, plagioclase and hornblende, *d)* photomicrograph of sample JA10 showing garnet, clinopyroxene, plagioclase and ilmenite, *e)* photomicrograph of EM16 showing clinopyroxene inclusions within garnet, *f)* photomicrograph of sample EM16 showing garnet surrounded by clinopyroxene, *g)* photomicrograph of EM19 showing garnet and clinopyroxene rimmed by actinolite-magnesiohornblende in plagioclase matrix. Hornblende is also in the matrix but is out of field of view, *h)* photomicrograph of sample JA14 showing feldspar, fined grained muscovite, garnet and biotite. Abbreviations used: gt = garnet, bi = biotite, hb = hornblende, cpx = clinopyroxene, q = quartz, pl = plagioclase, mu = muscovite, Ksp = K-feldspar, ky = kyanite act = actinolite-magnesiohornblende, ilm = ilmenite.

Figure 5. a-d) Microprobe elemental maps for Fe, Mg, Ca and Mn of garnet for an area of sample JA3.

Figure 6. Calculated *P-T* pseudosection for sample JA3 with interpreted peak assemblage indicated by bold outline (biotite, garnet, kyanite, plagioclase, quartz, rutile, melt, K-feldspar), with GASP barometer (garnet-kyanite-quartz-plagioclase) plotted as red circles, *a)* calculated modal proportions of garnet in black (g) and biotite in blue (bi), *b)* calculated compositional isopleths for X_{Alm} represented by green lines, X_{Grs} represented by black lines and X_{An} represented by red lines.

Figure 7. Calculated *P-T* pseudosection for sample JA7 with interpreted peak assemblage indicated by bold outline (biotite, garnet, kyanite, plagioclase, quartz, rutile,

melt, K-feldspar), with GASP barometer (garnet-kyanite-quartz-plagioclase) plotted as red circles, *a)* calculated modal proportions of garnet in black (g) and biotite in blue (bi), *b)* calculated compositional isopleths for X_{Alm} represented by green lines, X_{Grs} represented by black lines and X_{An} represented by red lines, *c)* superimposed JA3 and JA7 with common *P-T* space of peak field outlined in bold.

Figure 8. a-f) Graphical representations of average *P-T* conventional thermobarometry for reaction sets JA9a-1, JA9a-2, JA10-1, JA10-2, EM19-1 and EM19-2, with aH_2O= 0, 0.25 and 0.5 superimposed on garnet-clinopyroxene and garnet-amphibole thermometers. Bold ellipse corresponds to appropriate aH_2O for each reaction set.

Figure 9. a) Table summarising average *P-T* conventional thermobarometry estimates, *b)* weighted average of conventional thermobarometry temperatures for JA9a-1, JA9a-2, JA10-1, JA10-2, EM19-1, EM19-2 and *b)* weighted average of conventional thermobarometry pressures JA9a-1, JA9a-2, JA10-1, JA10-2, EM19-1, EM19-2.

Figure 10. Sample JA3 LA-ICP-MS U-Pb zircon geochronology data, *a)* Concordia plot of 100 ± 5 % concordant data, inset top: concordia plot of all data, inset bottom: probability density plot for all data (top dashed line) and 100 ± 5 % concordant data (bottom solid line) with population maxima, *b)* $^{207}Pb/^{206}Pb$ weighted average of 100 ± 5 % concordant oscillatory zoned cores, uncertainty is quoted at 1 σ, *c)* Concordia plot for 100 ± 5 % concordant oscillatory zoned cores, *d)* $^{207}Pb/^{206}Pb$ weighted average of 100 ± 5 % concordant weakly luminescent domains, uncertainty is quoted at 1 σ, e*)* Concordia plot for weakly 100 ± 5 % concordant weakly luminescent domains.

Figure 11. Sample JA13 LA-ICP-MS U-Pb zircon geochronology data, *a)* Concordia plot of all 100 ± 10 % concordant data, inset top: all data, inset bottom: probability density plot for all data (top dashed line) and 100 ± 10 % (bottom solid line) with population maxima, *b)* $^{207}Pb/^{206}Pb$ weighted average of 100 ± 10 % concordant data excluding interpreted inherited cores, uncertainty is quoted at 1 σ, *c)* Concordia plot of 100 ± 10 % concordant data excluding interpreted inherited cores, *d)* Concordia plot of interpreted oscillatory zoned cores.

Figure 12. Sample JA14 LA-ICP-MS U-Pb zircon geochronology data, *a)* Concordia plot of 100 ± 10 % concordant data, inset concordia plot of all data, *b)* $^{207}Pb/^{206}Pb$ weighted average of 100 ± 10 % concordant data, uncertainty is quoted at 1 σ, *c)* Probability density plot of all data (dashed line) and 100 ± 10 % concordant data (solid line).

Figure 13. Sample JA7 LA-ICP-MS U-Pb monazite geochronology data, *a)* Concordia plot of monazite data, *b)* $^{207}Pb/^{206}Pb$ age weighted average of monazite data, uncertainty is quoted at 1 σ, *b)* $^{207}Pb/^{206}Pb$ age probability density plot of monazites with population maxima.

Figure 14. a) Representative monazite Backscatter-Electron image of sample JA7 with location of LA-ICP-MS analysis and individual $^{207}Pb/^{206}Pb$ age quoted to 2 σ, *b-f)* representative Cathodoluminescence zircon images of sample JA3, JA13 and JA14 with location of LA-ICP-MS analysis and individual $^{207}Pb/^{206}Pb$ age quoted to 2 σ.

Figure 15. a, c, e) Th vs. U concentrations (ppm) for samples JA3, JA13 and JA14 respectively, *b, d, f)* Th/U ratios vs. $^{207}Pb/^{206}Pb$ age for samples JA3, JA13 and JA14 respectively.

Figure 16. a) Zircon chondrite normalised REE plots for sample JA14, shaded area are core analyses, black individual line are rims, *b)* Zircon chondrite normalised REE plots for sample JA3, shaded area are core analyses, blue individual plots are weakly luminescent domains (cores and rims) showing solid state recrystallisation features, red individual plot are weakly luminescent featureless domains (cores and rims).

Figure 17. a) Age (Ma) *vs. P* estimates of metamorphic events between 2400-3500 Ma for temperature > 700 ºC in black diamonds with peak *P-T* estimates from this study in red circle, *b)* Age (Ma) vs. apparent geothermal gradient (ºC/km) for metamorphic events between 2400-3500 Ma for temperature > 700 ºC in black diamonds with peak *P-T* estimates from this study in red circle. Apparent geothermal gradient is calculated from 3.3km/kbar for simplicity. Data represented by black diamonds are from plots and graphs compiled by Brown (2007a), and *P-T* estimates of the Sleafordian Orogeny from Dutch *et al.* (2010).

Table 1 . Summary of lithological features, units and structure in sample collection area of Kanja Malai Hills.

Table 2-3. Representative EPMA analyses of samples JA3, JA7, JA9a, JA10, EM16, EM19.

Table 4. Top: Conventional thermobarometry estimates showing water activity, average *P*, average *T* and average *P-T* for samples JA9a, JA10 and EM19. Middle: Fe-Mg thermometry for samples JA9a, JA10 and EM19. Bottom: Grossular-Quartz-Kyanite-Anorthite (GASP) barometer for samples JA3 and JA7.

Table 5-8. Zircon geochronology tables for samples JA3, JA13 and JA14. $^{+}$ denotes that analysis was disgarded, * denotes that effective age is $^{207}Pb/^{206}Pb$.

*Table 9.*Monazite geochronology table for samples JA7. $^{+}$ denotes that analysis was disgarded, * denotes that effective age is $^{207}Pb/^{206}Pb$.

Table 10. Zircon chondrite normalised major, trace and REE table of samples JA3 and JA14.

11. APPENDIX I- MONAZITE AND ZIRCON CHARACTERISTICS

11.1 Monazite characteristics

JA7

Monazite grains from this sample are typically subhedral to anhedral, approximately 20–60 μm long and irregularly shaped, although sub-rounded grains are also present. Monazite grains are texturally located within garnet, on the edges of garnet and within the quartz, K-feldspar, plagioclase matrix. Most monazite grains exhibit irregular internal zoning when viewed under BSE (Fig. 14a). However, some monazite grains display a lighter core and a darker rim or no zoning. No correspondence between monazite grain morphology and textural relationship could be established.

11.2 Zircon characteristics

SAMPLE JA3

Zircon grains from this sample are approximately 100 to 300 μm long and commonly have subhedral prismatic to stubby external morphologies with sub-rounded to rounded crystal terminations and aspect ratios of ~4:1 to 3:1. Approximately 60% of zircon grains show moderately to weakly luminescent cores with sporadically preserved oscillatory zoning (Fig. 14.b). These cores are often observed to be partially overgrown by thick (~20–40 μm) weakly luminescent rims (Fig. 14.c). A thick, weakly luminescent rim is visible in most zircon grains, in which the same oscillatory zonation present in the core is sometimes faintly visible. Similar features have been described by Hoskin & Black (2000) and termed ‘ghost rims’. Approximately 40% of zircon grains have weakly luminescent cores, often displaying zoning that is relatively parallel to the

outer crystal faces. Similarly to zircon grains with oscillatory zoned cores, these zircon grains often have a strongly luminescent and featureless outer rim.

SAMPLE JA14

Zircon grains from this sample range from 50 to 200 µm long, with external morhpologies that are dominantly subhedral to anhedral and rounded to ovoid in shape, with aspect ratios from 1:1 to 3:1. Approximately 80% of zircon grains display a core, half of these have a strongly luminescent core that is either featureless or displays oscillatory zoning (~50-70 µm in diameter). These cores often contain strongly luminescent cracks. Cores that display faded oscillatory zoning are often truncated by a strongly luminescent, featureless domain similar to the 'recrystallisation fronts' described by Hoskins and Black (2000). The other cores are weakly luminescent (~30-100 µm in diameter), and some of these cores exhibit faded concentric or oscillatory patterns, truncated by a moderately luminescent to strongly luminescent featureless domains. The boundaries between cores and moderately-strongly luminescent featureless domains vary from sharp to gradual and are usually rounded to irregular. Most zircon grains also show weakly luminescent rims and sometimes show faint concentric zoning. The majority of rims are irregular in shape and are usually truncated by the inner strongly luminescent featureless domains, however some zircon grains show rims that truncate other internal features (Fig. 14.d).

SAMPLE JA13

Zircon grains from this sample range from 75 to 200 µm long and have external morphologies that are dominantly subhedral and subrounded to ovoid in shape, although some zircon grains have subhedral and prismatic to stubby morphologies with subrounded pyramidal terminations. Zircon cores are commonly moderately to weakly luminescent and typically display either oscillatory or concentric luminescence zoning, or have a very weakly luminescent featureless inner core and concentric zoned outer core. Some zircon grains show convoluted structures and sometimes display chaotic internal morphologies. Approximately 20% of zircon cores have oscillatory zoning that is characteristic of primary igneous textures (Hoskin & Black 2000; Corfu *et al.* 2003a).

Approximately 40% of cores show concentric/sector zoned cores, which, when coupled with dominantly sub-rounded to ovoid external morphologies and weakly luminescent cores is indicative of new metamorphic growth (Corfu *et al.* 2003a; Hoskin & Schaltegger 2003). 40% of cores are weakly luminescent and featureless, and may indicate the cores have undergone recrystallisation. This recrystallisation may be concentrated in the core as result of metamictisation from higher Th and U contents than surrounding rims, making the resulting metamict core region more susceptible to subsequent thermal recrystallisation (Geisler *et al.* 2001). Some zircon grains also show a moderately to strongly luminescent inner core with boundaries that are in different orientations to the majority of internal morphological boundaries. This striking change in luminescence and shape of the internal core suggests the inner core may be inherited (e.g. Fig. 14.e). Most zircon grains have weakly luminescent rims of varying thickness

that appear to truncate the core. Some rims are featureless (Fig. 14.f), while others preserve faint concentric patterns.

12. APPENDIX II- ANALYTICAL PROCEDURES

12.1 Quantified metamorphic analysis- *P-T* phase diagrams

An approximately 10 x 10 x 0.5 cm representative slice of each sample was crushed using a jaw crusher and milled to a particle size of <75 µm. Elements were analysed using solution ICP-OES and ICP-MS at Amdel Laboratories, Adelaide. Samples were prepared for major and some trace element analysis by fusion of 0.1 g of the milled sample with lithium metaborate and dissolution in nitric acid. The remaining trace and REE elements were prepared by digestion of 0.5 g of the milled sample in hydrofluoric acid/multi acid solution for analysis of concentrations REE and trace elements (see Payne *et al.* 2010).

P-T pseudosections were calculated using the phase equilibria modelling program THERMOCALC v3.33 (June 2009 update of Powell & Holland 1988), using the internally consistent dataset of Holland and Powell (Holland & Powell 1998; data set tc-ds55, updated Nov. 2003). The geologically realistic system NCKFMASHTO (Na_2O-CaO-K_2O-FeO-MgO-Al_2O_3-SiO_2-H_2O-TiO_2-Fe_2O_3) was used for P-T pseudosection calculations using *a-x* relationships of White et al. (2007) for biotite, garnet and silicate melt, White et al. (2000) for ilmenite, Holland and Powell (2003) for K-feldspar plagioclase and White et al. (2002) for magnetite and orthopyroxene. Microprobe

analyses of individual minerals were used to determine observed compositional abundance.

12.2 Quantified metamorphic analysis- Thermobarometry

ANALYTICAL PROCEDURES

Average pressure-temperature thermobarometry (Powell & Holland 1994) was conducted on three garnet, clinopyroxene bearing mafic gneiss samples in the northern Kanja Malai Hills. Electron microprobe was used to obtain spot chemical compositions for minerals that are considered to have once been in equilibrium with each other, for the purpose of conventional average pressure-temperature thermobarometry (Powell & Holland 1994; Powell & Holland 2008). Software AX (Powell *et al.* 1998) was used to calculate mineral end member activity and compositional relationships.

Pressure and temperatures estimates were obtained following the method of Powell and Holland (1994), whereby average *P*, average *T* and average *P-T* were calculated using multiple independent sets of reactions representing the equilibria volume. THERMOCALC v. 321 software (update of Powell and Holland, 1988) was used to calculate average *P-T* by determining an optimal *P-T* solution from the thermodynamics of an independent set of end member reactions. As outlined in Powell and Holland (1994), multiple reactions that involve one or more of the same end member allow the behaviour of activities and uncertainties to be correlated in a predictable manner. Uncertainty of the optimal solution is statistically quantified using a least squares method that proportionally varies the positions of reactions with respect to their uncertainties and correlations so that a common intersection is obtained. The statistical

χ^2 test at 95% confidence level was employed to assess the scatter of the observed minus the calculated data values and associated uncertainties. Failure of the χ^2 test may be a due to one or more outlying end members or a general scatter of the data. On occasions where the χ^2 test failed, one or two statistical outlier end members were omitted. The omission of the outliers resulted in a better constrained sigma fit and passing of the χ^2 test with 95% confidence, yet did not alter the *P-T* estimates by more than 50 °C or 1 kbar.

Conventional thermobarometry was conducted using end member activity and compositional relationships of two sets of mineral chemical analyses per sample. Six to nine independent reactions were obtained for all three samples JA9a, JA10, EM19 for use in thermobarometry calculations. The selection of water activity (aH$_2$O) values (necessary due to presence of hydrous mineral phases in the equilibration volume) was investigated by conducting average *P-T* calculations with varying aH$_2$O (aH$_2$O = 0, 0.25, 0.5), coupled with H$_2$O independent single reaction thermometer calculations incorporating Fe-Mg end members of clinopyroxene, amphibole and garnet using mode 3 THERMOCALC v 3.21 (update of Powell and Holland, 1988). The correspondence between these two methods can assist with the estimation of aH$_2$O in mineral equilibria (Raimondo 2009) (refer to Fig. 8). Estimation of aH$_2$O was obtained by: 1) assessing the correspondence between Fe-Mg reaction thermometers and average *P-T* of using varying aH$_2$O, 2) refining aH$_2$O based on associated aH$_2$O values that allow *P-T* estimates to pass χ^2 test at 95% confidence level, and 3) refining aH$_2$O values based on those that are associated with better constrained *P-T* estimates with smaller uncertainties.

12.3 LA-ICP-MS U-Th-Pb zircon and U-Pb monazite Geochronology

U-(Th)-Pb geochronology was conducted using the Laser Ablation Inductively Coupled Plasma Mass Spectrometer (LA-ICP-MS) at Adelaide Microscopy, University of Adelaide. Samples for zircon geochronology were crushed using a jaw crusher, placed in a tungsten carbide mill for 3–5 seconds and sieved using 75 μm and 425 μm mesh, retaining a size fraction between 75–425 μm. Zircon grains were subsequently separated using traditional panning techniques, followed by removal of magnetic mineral grains from the heavier mineral fraction using conventional and neodymium magnets. Approximately 200 zircon grains per sample were randomly handpicked and mounted in epoxy resin. Mounted zircon grains were ground down to approximately half their width.

Thin sections and epoxy mounts were imaged using a Phillips XL20 SEM with attached Gatan cathodoluminescence (CL) detector at Adelaide Microscopy to determine internal chemical zonation of zircon and monazite grains and the textural relationship of monazite grains to other minerals. A beam accelerating voltage of 12 kV was used, combined with a spot size of 7 when zircon mounts were imaged using CL detector, and spot size of 5 when monazite grains in thin section were imaged using a backscattered electron (BSE) detector.

U-Th-Pb analysis of zircon and *in situ* U-Pb analysis of monazite was undertaken using an Agilent 7500cs ICPMS with a New Wave 213 nm Nd-YAG laser in a helium ablation atmosphere, following similar methods and operating procedures outlined by Payne et al. (2008; 2010). A laser spot size of 30 μm and repetition rate of 5 Hz was

used for zircon analyses. A 40 second gas blank was initially measured followed by 60 seconds of zircon sample ablation. The laser was fired for 10 seconds with the shutter closed seconds prior to ablation in order to allow for beam and crystal stabilisation. A spot size of 12 μm, repetition rate of 5 Hz and laser intensity of 70% was used for monazite analyses. A 50 second blank was measured proceeded by 50 seconds of monazite sample ablation. Similarly to zircon analyses, the laser was fired for 10 seconds with the shutter closed prior to ablation.

Analyses measured isotopes ^{204}Pb, ^{206}Pb, ^{207} Pb and ^{238}U for 10, 15, 30 and 15 ms respectively for monazite grains, and ^{204}Pb, ^{206}Pb, ^{207}Pb, ^{208}Pb, ^{232}Th and ^{238}U for 10, 15, 30, 10, 10, 15 ms respectively for zircon grains. For both zircon and monazite analyses, common lead was not corrected due to an unresolvable interference of ^{204}Hg and ^{204}Pb peaks, however ^{204}Pb was monitored to assess the common lead of each analysis. No anomalous ^{204}Pb above background counts were observed.

The real-time correction program Glitter vers. 4.0 (Van Achterbergh *et al.* 2001) was used to correct zircon and monazite data. Mass bias and fractionation were corrected for zircon analyses using the GEMOC standard GJ-1 (TIMS normalisation data: 207Pb/206Pb = 608.3 Ma, 206Pb/238U = 600.7 Ma and 207Pb/235U = 602.2 Ma; Jackson *et al.* 2004). An uncertainty of 1% was assigned to the age of the GJ-1 zircon standard for sample age error calculations to avoid inaccurate age reporting. An internal standard, the Plesovice zircon standard (ID TIMS 206Pb/238U age = 337.13 ± 0.37 Ma; Sláma *et al.* 2008) was used to assess accuracy before and during the analysis of unknowns. Average Plesovice ages obtained during this study were ^{207}Pb/^{235}U = 339 ±

3.4 Ma (2σ, *n* = 36, MSWD = 1.4), $^{207}Pb/^{206}Pb$ = 344 ± 19 Ma (MSWD = 0.4) and $^{206}Pb/^{238}U$ = 337 ± 3.2 Ma (MSWD = 1.12).

Monazite standard 44069 was used to correct for mass bias and fractionation for monazite analyses (TIMS normalisation data: 206Pb/238U = 426 ± 3 Ma; Aleinikoff 2006). A 1% uncertainty was given to the age of the 44069 standard for sample age error calculations. Accuracy was monitored by analysing the Madel monazite standard prior to and during unknown analysis runs (TIMS Madel age: 207Pb/206Pb = 490.7 Ma, 206Pb/238U = 514.8 Ma and 207Pb/235U = 510.4 Ma; Payne *et al.* 2008). Average Madel monazite ages obtained throughout this study were $^{207}Pb/^{235}U$ = 511 ± 9.6 Ma (2σ, *n* = 8, MSWD = 0.29), $^{207}Pb/^{206}Pb$ = 495 ± 38 Ma (MSWD = 0.31) and $^{206}Pb/^{238}U$ = 515.3 ± 10.8 Ma (MSWD = 0.13). Conventional concordia, weighted averages, and probability density distribution plots were generated using Isoplot vers. 4.11 (Ludwig 2003). All quoted effective ages are $^{207}Pb/^{206}Pb$ ages. Calculation of Th/U ratios was achieved by applying an offline linear correction equation correcting to a known Th and U concentrations of 8.84 ppm and Th 264 ppm Ufor the GJ zircon standard.

12.4 Zircon REE chemistry

REE and trace elements of zircon grain mounts for samples JA3, JA7 and JA14 were analysed using the LA-ICP-MS at Adelaide Microscopy. Oscillatory zoned cores and weakly luminescent domains with pre-collected U-Th-Pb data were analysed. Analyses were conducted using 40 μm laser spot size at 75% intensity and 5 Hz repetition rate. Total acquisition time was 110 seconds, divided into a 40 second gas blank, 10 second firing of the laser with the shutter closed and 60 seconds of laser ablation. External

standard Nist 610 was used correct for fractionation and mass bias (Pearce *et al.* 1997), and standards Nist 612 and BHVO were used as internal standards to monitor the accuracy of analyses. Data was corrected using GLITTER software (Van Achterbergh *et al.* 2001). Analyses were calibrated internally using ^{72}Hf oxide percent measurements on zircon domains corresponding to spot locations of LA-ICP-MS REE and trace element analyses using Cameca SX51 microprobe at Adelaide Microscopy with an accelerating voltage of 15 kV and beam current of 20 nA.

Figure 1

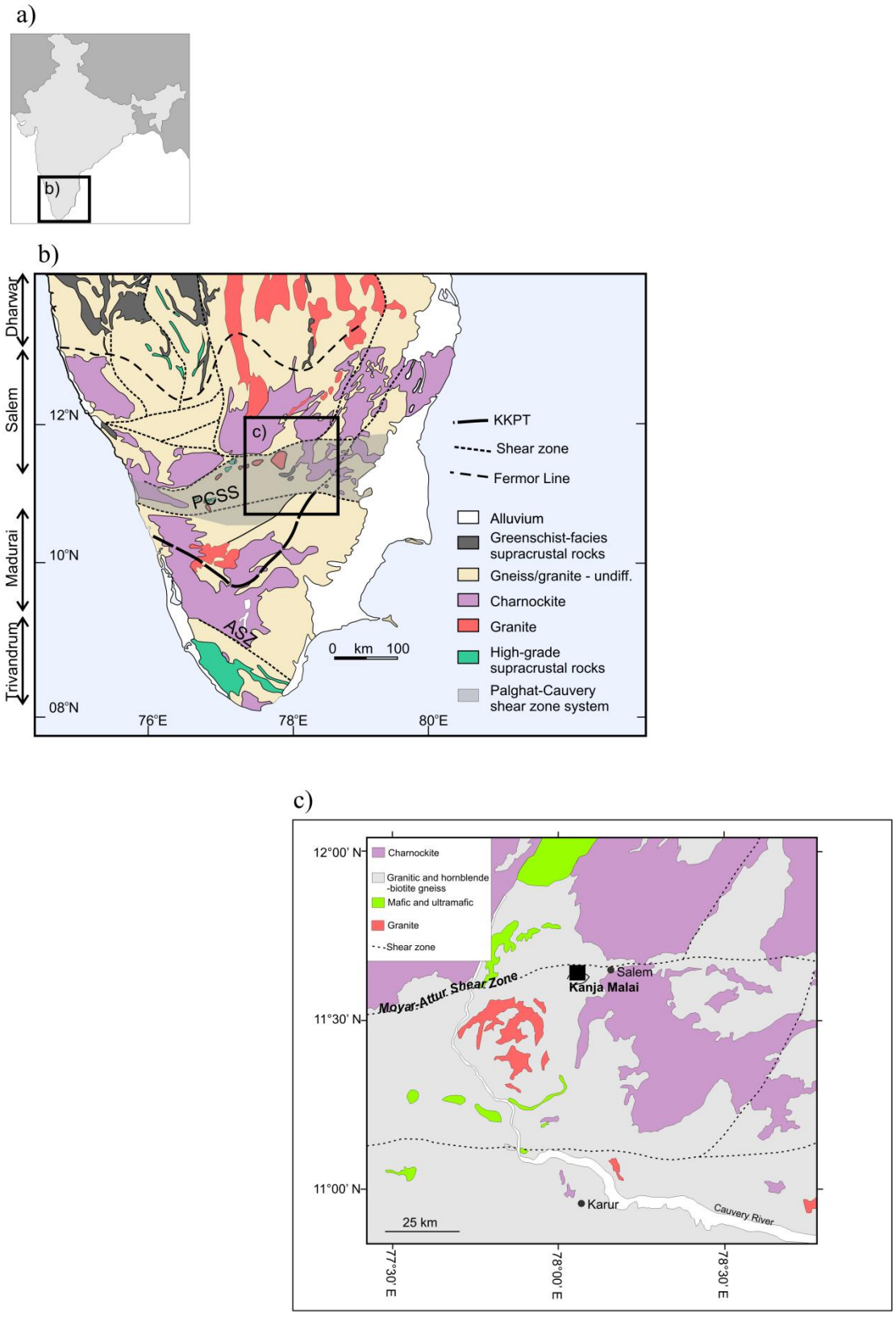
a)
b)
b)
Dharwar
Salem
Madurai
Trivandrum
12°N
10°N
08°N
76°E
78°E
80°E
c)
PCSS
ASZ
0 km 100
KKPT
Shear zone
Fermor Line
Alluvium
Greenschist-facies supracrustal rocks
Gneiss/granite - undiff.
Charnockite
Granite
High-grade supracrustal rocks
Palghat-Cauvery shear zone system
c)
12°00' N
11°30' N
11°00' N
77°30' E
78°00' E
78°30' E
Charnockite
Granitic and hornblende -biotite gneiss
Mafic and ultramafic
Granite
Shear zone
Moyar-Attur Shear Zone
Salem
Kanja Malai
Karur
Cauvery River
25 km

Figure 2

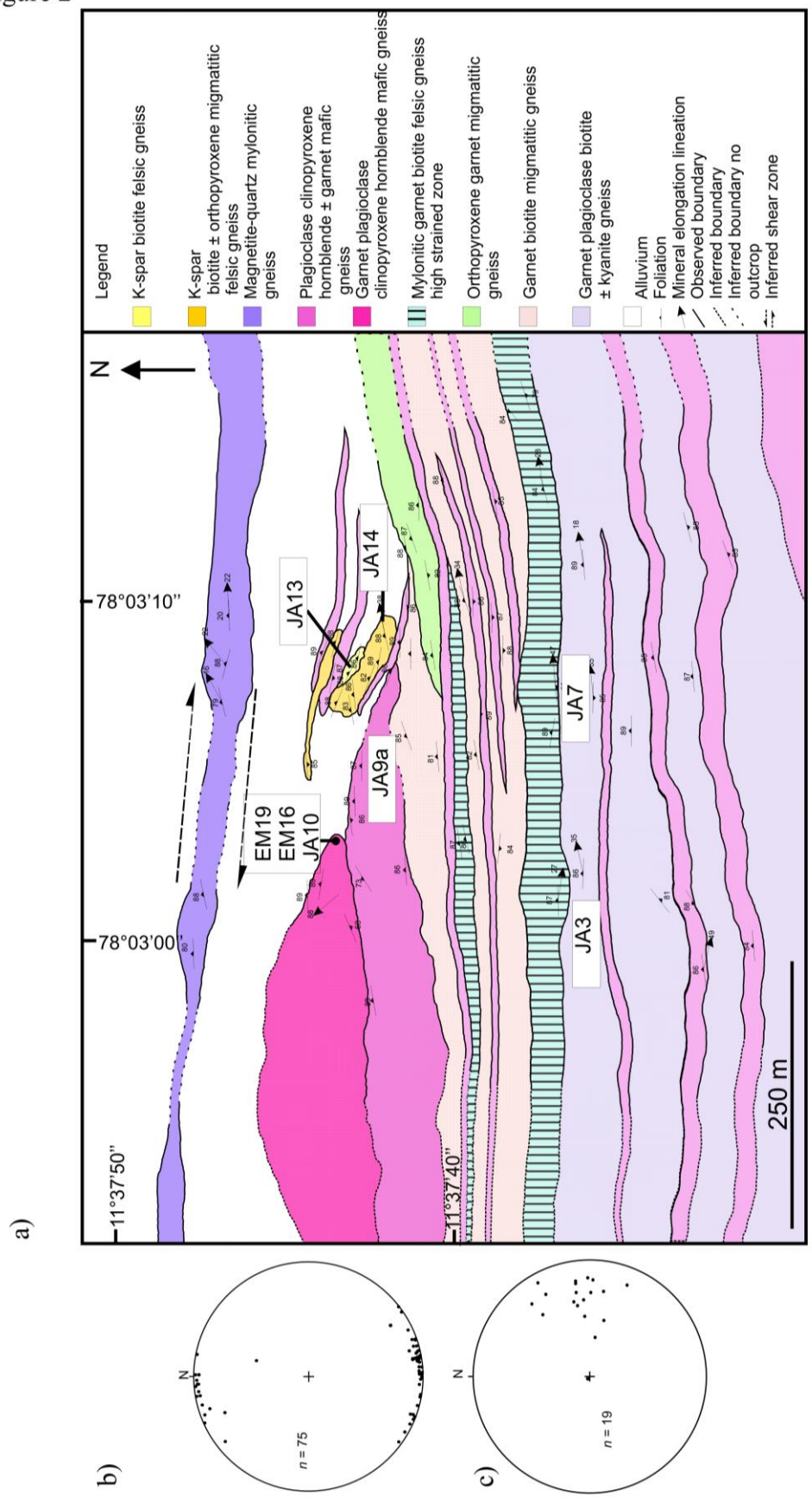
a)
b)
c)
Legend
K-spar biotite felsic gneiss
K-spar biotite ± orthopyroxene migmatitic felsic gneiss
Magnetite-quartz mylonitic gneiss
Plagioclase clinopyroxene hornblende ± garnet mafic gneiss
Garnet plagioclase clinopyroxene hornblende mafic gneiss
Mylonitic garnet biotite felsic gneiss high strained zone
Orthopyroxene garnet migmatitic gneiss
Garnet biotite migmatitic gneiss
Garnet plagioclase biotite ± kyanite gneiss
Alluvium
Foliation
Mineral elongation lineation
Observed boundary
Inferred boundary
Inferred boundary no outcrop
Inferred shear zone
N
78°03'10"
78°03'00"
11°37'50"
11°37'40"
JA13
JA14
JA9a
EM19
EM16
JA10
JA7
JA3
250 m
n = 75
n = 19

Figure 3

a) 

b) 

c) 

d) 

e) 

f) 

g) 

h) 

Figure 4

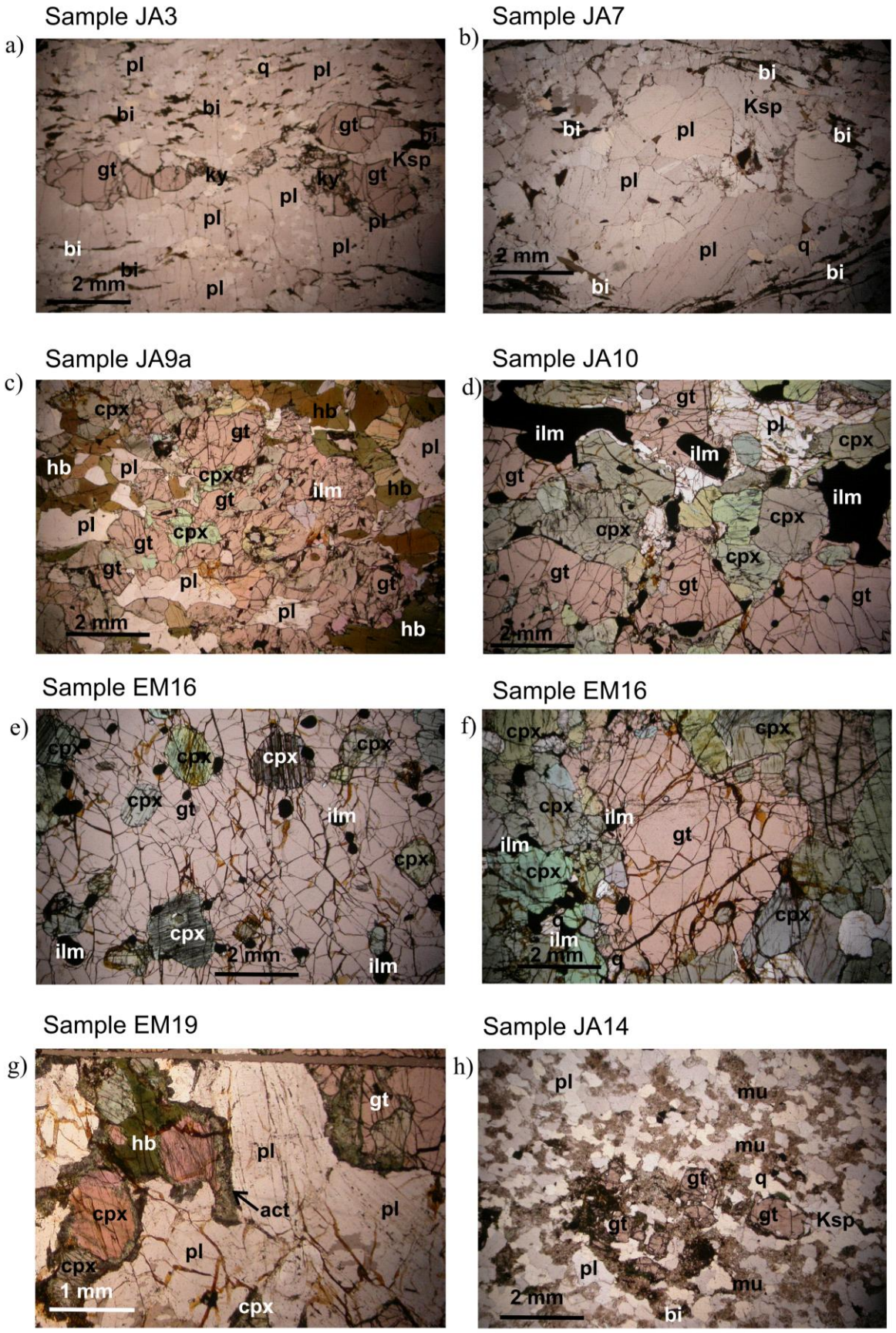
Sample JA3
a)
pl
q
pl
bi
bi
gt
bi
gt
ky
ky
gt
Ksp
pl
pl
pl
bi
pl
bi
2 mm
pl
Sample JA7
b)
bi
Ksp
bi
pl
bi
pl
2 mm
pl
q
bi
bi
Sample JA9a
c)
cpx
hb
gt
pl
hb
pl
cpx
ilm
hb
gt
pl
gt
cpx
gt
gt
pl
gt
pl
2 mm
hb
Sample JA10
d)
gt
ilm
pl
cpx
ilm
gt
ilm
cpx
cpx
cpx
gt
gt
gt
2 mm
Sample EM16
e)
cpx
cpx
cpx
cpx
cpx
gt
ilm
cpx
cpx
ilm
2 mm
ilm
Sample EM16
f)
cpx
cpx
cpx
ilm
ilm
gt
ilm
cpx
cpx
q
ilm
2 mm
q
Sample EM19
g)
gt
hb
pl
act
cpx
pl
pl
cpx
1 mm
cpx
Sample JA14
h)
pl
mu
mu
gt
q
gt
gt
Ksp
pl
mu
2 mm
bi

Figure 5

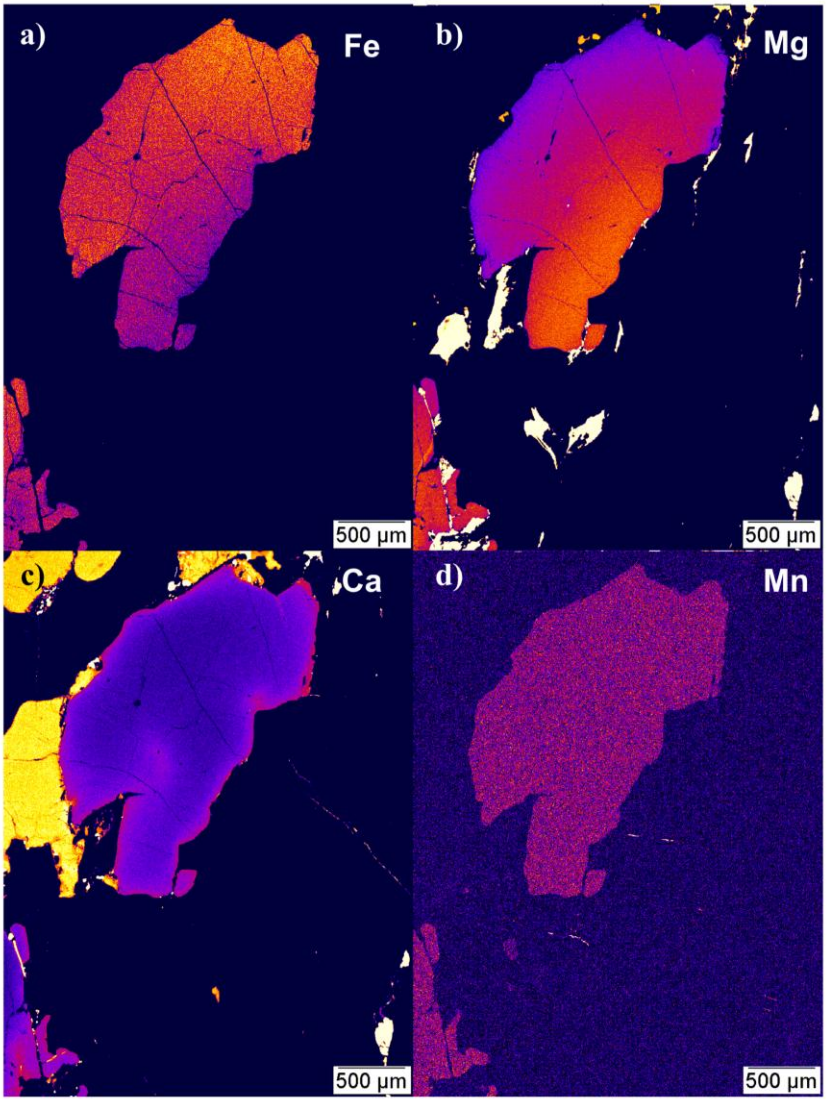

Figure 6: *P-T* pseudosection of JA3

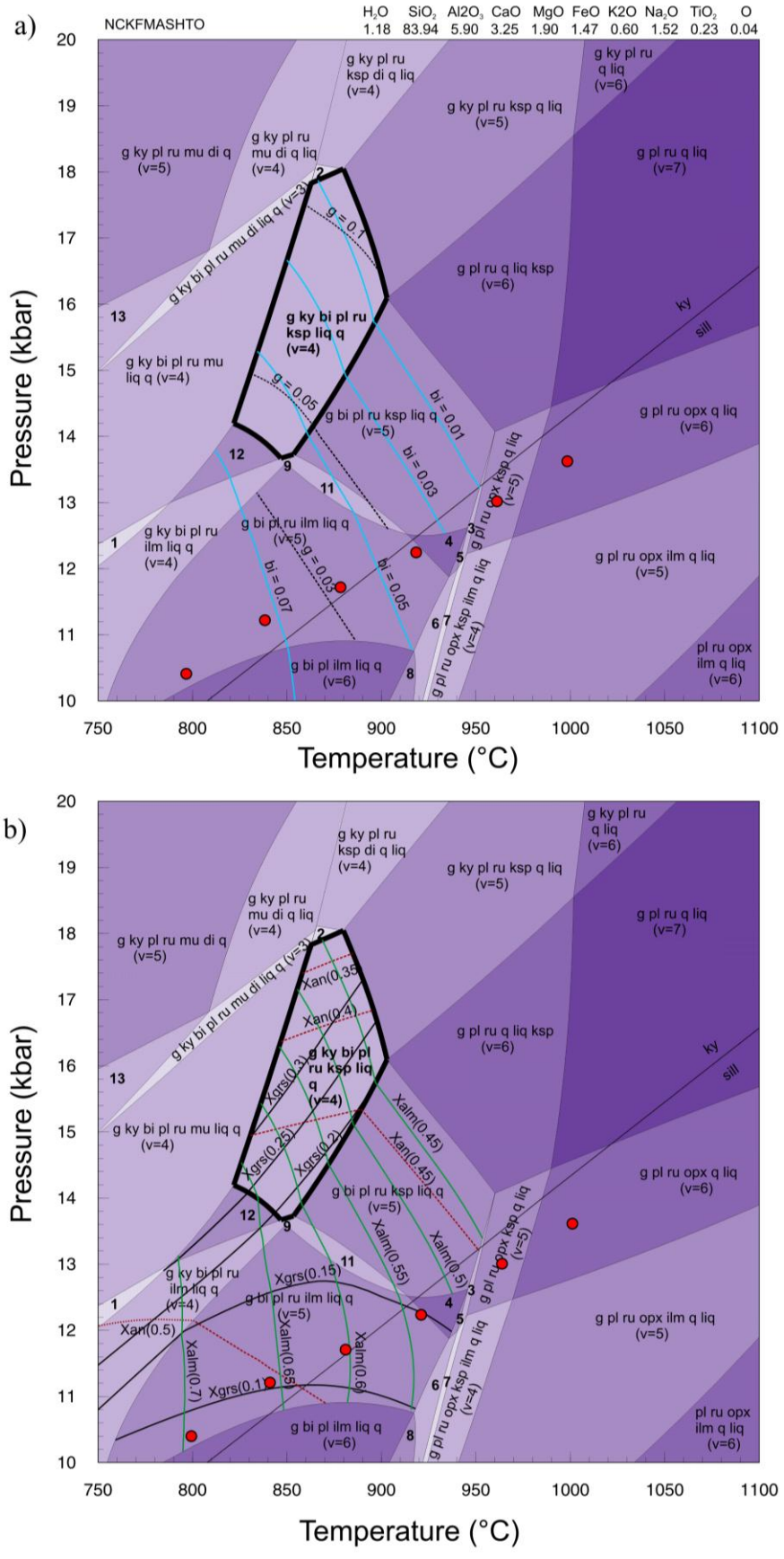

1. g ky bi pl ru ilm liq q mu (v=3)
2. g ky bi pl ru ksp liq q di (v=3)
3. g pl ru opx ksp q liq bi (v=4)
4. g bi pl ru liq g (v=6)
5. g bi pl ru liq q opx (v=5)
6. g bi pl ru ilm liq q opx (v=4)
7. g pl ru opx ksp ilm bi q liq (v=3)
8. g bi pl ilm liq q opx (v=5)
9. g bi pl ru ky ilm ksp liq q (v=3)
10. g bi pl ru ilm ksp liq q (v=4)
11. g bi pl ru ilm ksp liq q (v=4)
12. g ky bi pl ru liq q (v=5)
13. g ky bi pl ru mu di q (v=4)

● GASP barometer
grossular + quartz + 2kyanite
= 3anorthite

Figure 7: *P-T* pseudosection of JA7, and (inset) overlayed JA3 and JA7.

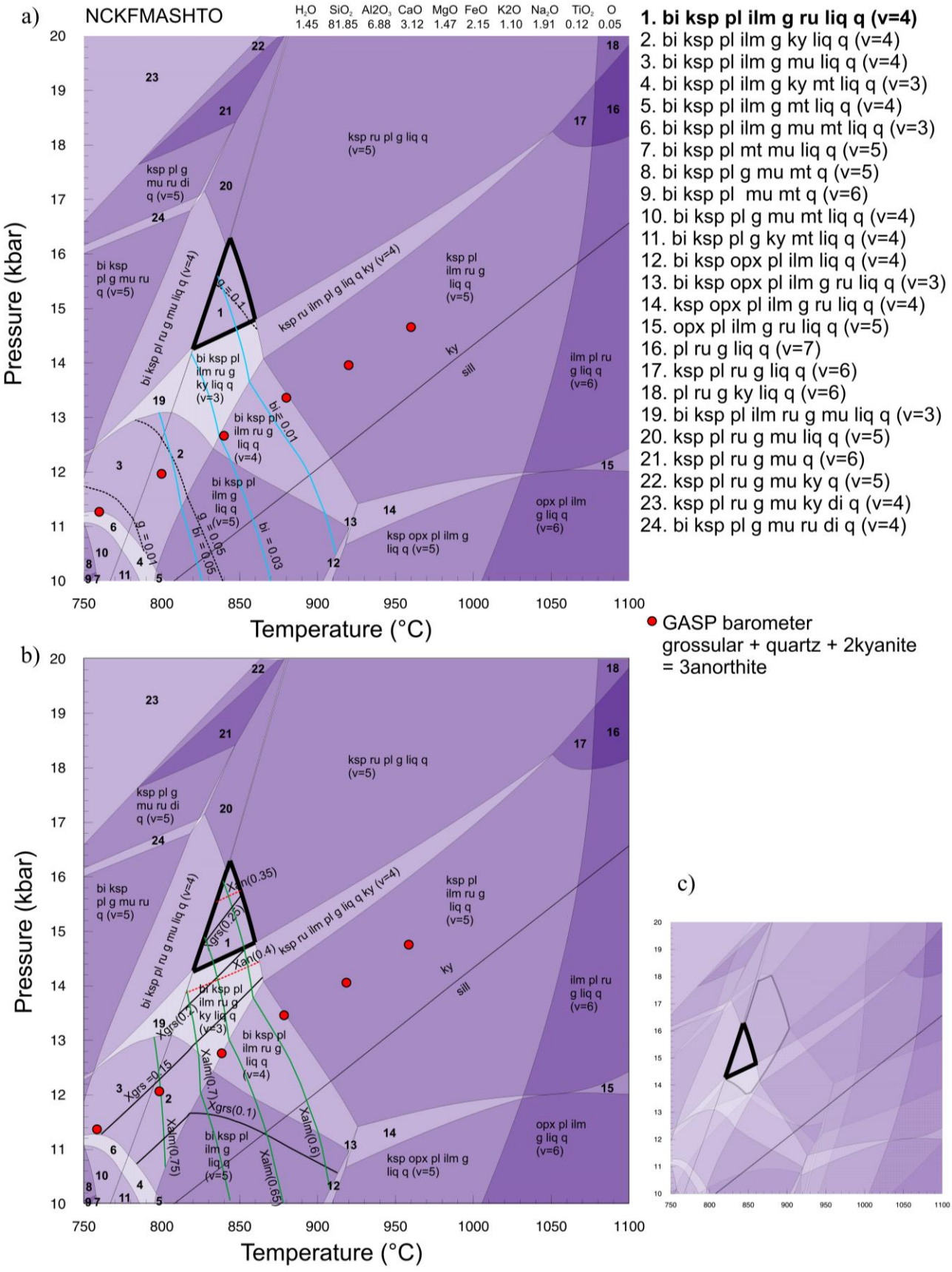

Figure 8: Garnet bearing mafic gneiss average *P-T* conventional thermobarometry

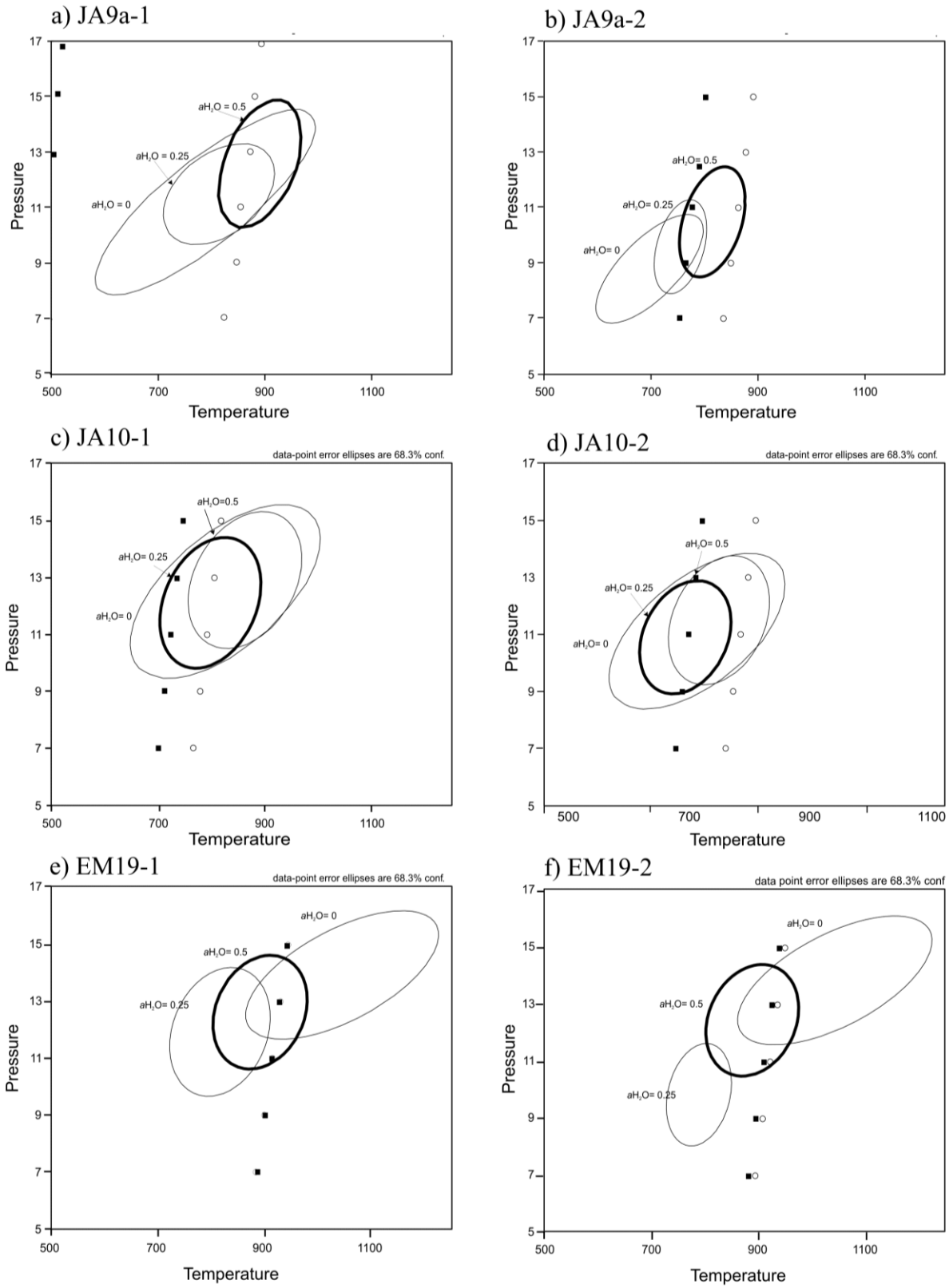

○ Reaction 1: garnet-clinopyroxene thermometer- 3di + alm = 3hed + py

▪ Reaction 2: garnet-amphibole thermometer- 5py + 3fact = 5alm + 3tr

Figure 9: Conventional thermobarometry results

a) Summary of average *P-T* results

Sample and analysis set	Average *P* (at 850°C) ± (1 σ)	Average *T* (at 12.5 kbar) ± (1 σ)	Average *P-T* ± (1σ)	
JA9a 1	12 ± 1.71	856 ± 50	12.6 ± 1.5	891 ± 51
JA9a 2	10.9 ± 1.20	826 ± 44	8.8 ± 1.3	815 ± 40
JA10 1	12.6 ± 1.48	777 ± 55	12.1 ± 1.5	798 ± 62
JA10 2	11.5 ± 1.53	763 ± 55	10.9 ± 1.3	764 ± 56
EM19 1	12.3 ± 1.13	876 ± 50	12.6 ± 1.3	891 ± 58
EM19 2	12.2 ± 1.14	877 ± 50	12.4 ± 1.3	890 ± 58
Average	11.9 ± 1.1*	832 ± 40*	11.5 ± 1.6*	839 ± 42*

* denotes weighted average ± 1 σ uncertainty

b) Weighted average of conventional thermobarometry temperatures (°C)

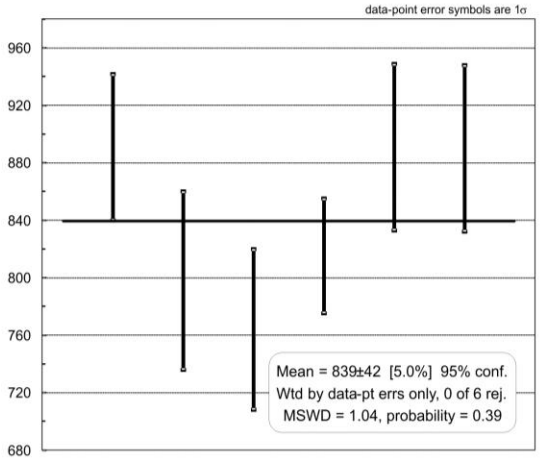

c) Weighted average of conventional thermobarometry pressures (kbar)

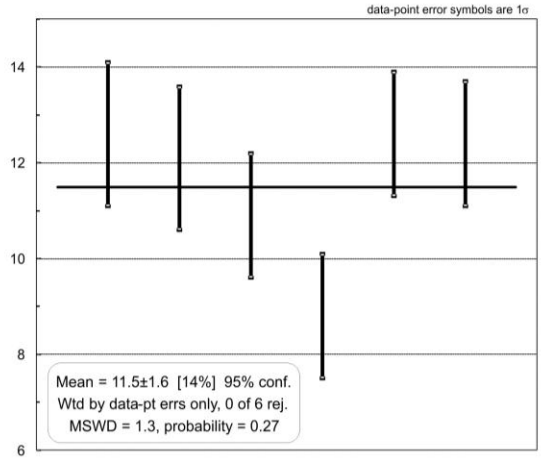

Figure 10: Sample JA3 U-Pb zircon geochronology

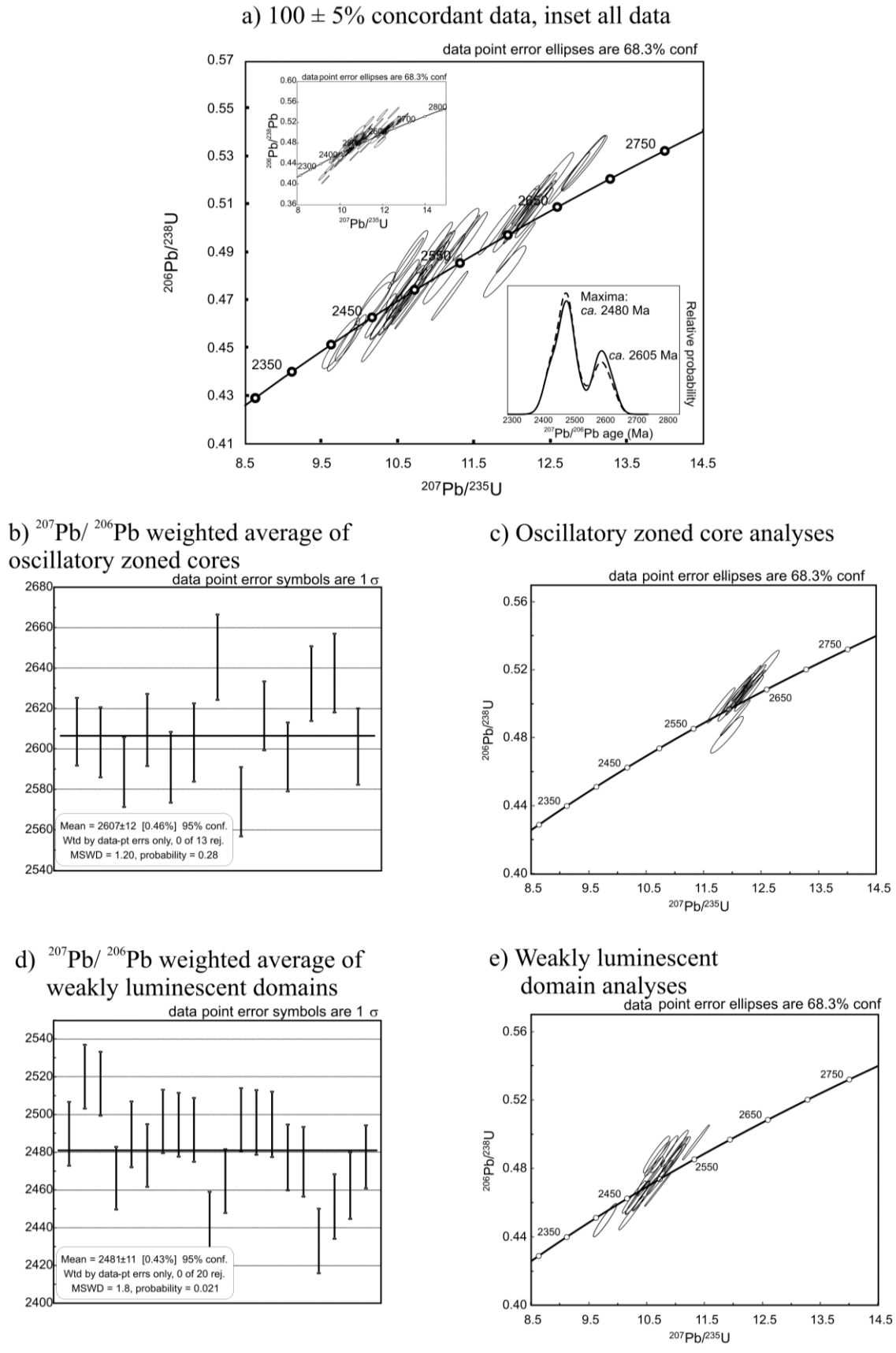

Figure 11: Sample JA13 zircon U-Pb geochronology

a) 100 ± 10% concordant data, inset all data

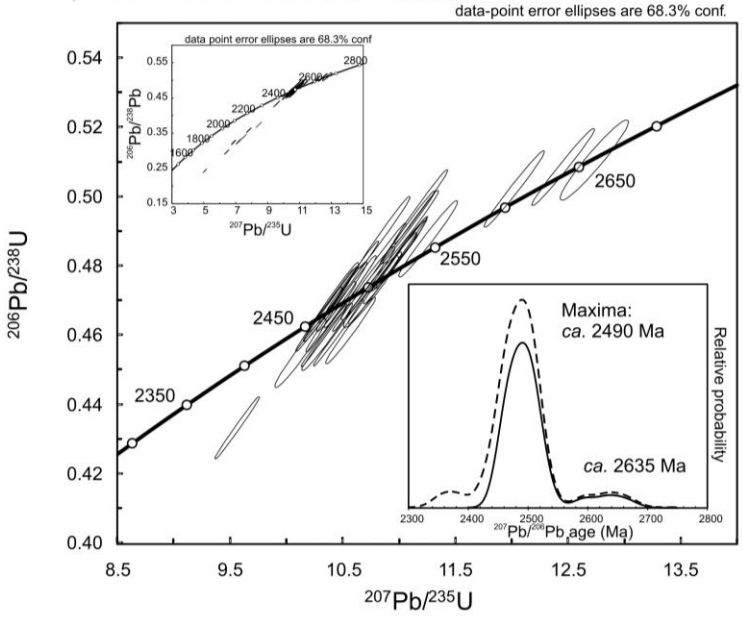

b) Weighted $^{207}Pb/^{206}Pb$ average of rims, weakly luminescent domains and concentric zoned cores

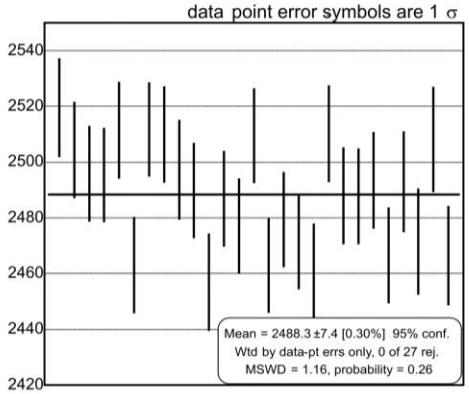

c) Rims, weakly luminescent domains and concentric zoned cores

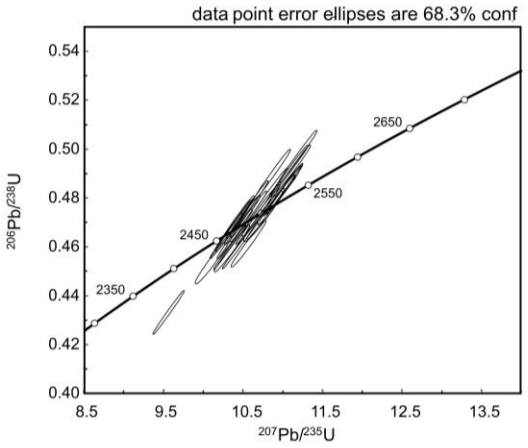

d) Inherited oscillatory zoned cores

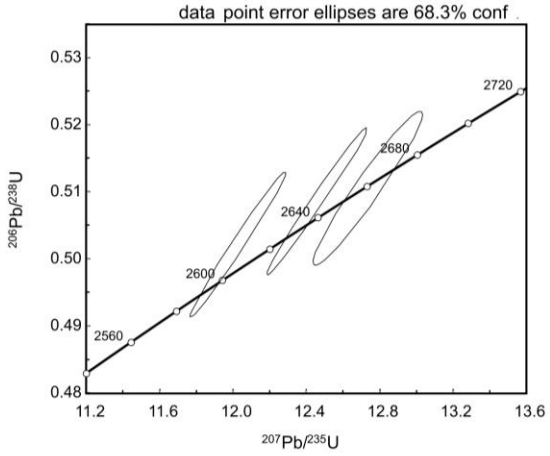

Figure 12: Sample JA14 U-Pb zircon geochronology

a) 100 ± 10% concordant data, inset all data

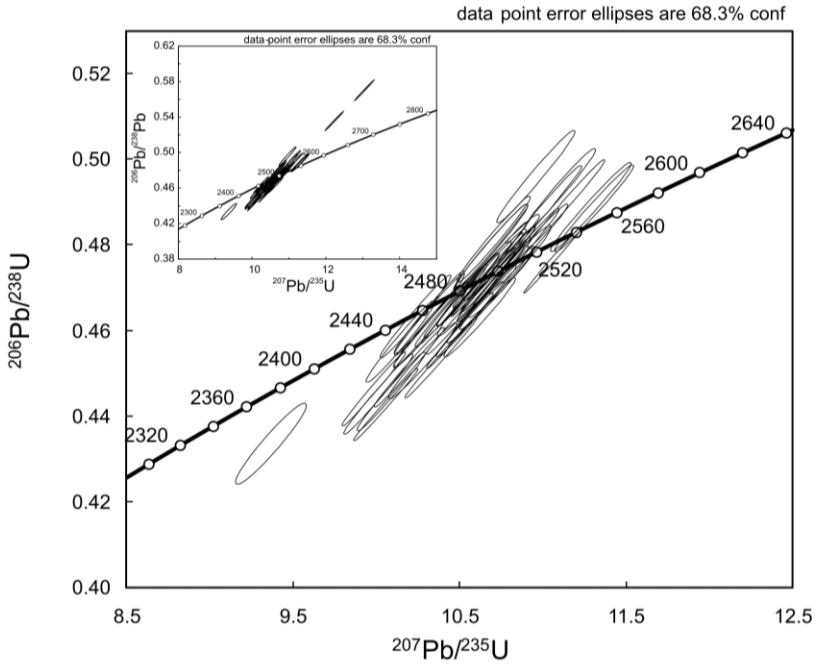

b) $^{207}Pb/^{206}Pb$ weighted average

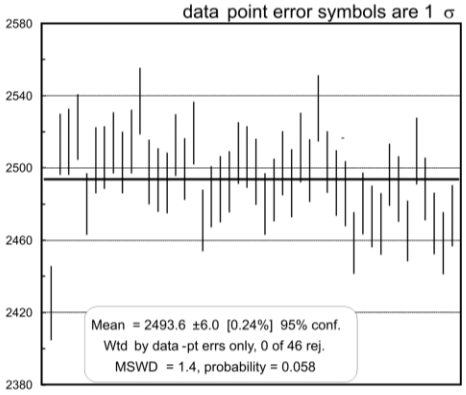

c) Probability density distribution plot

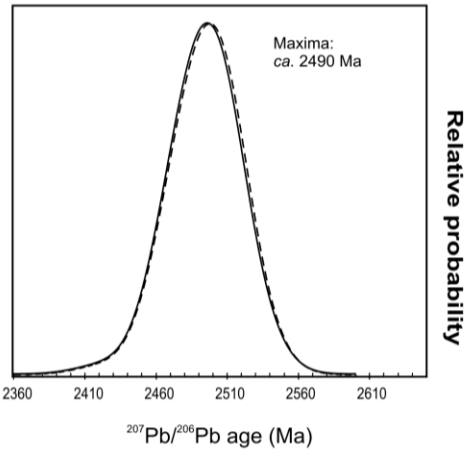

Figure 13: Sample JA7 U-Pb monazite geochronology

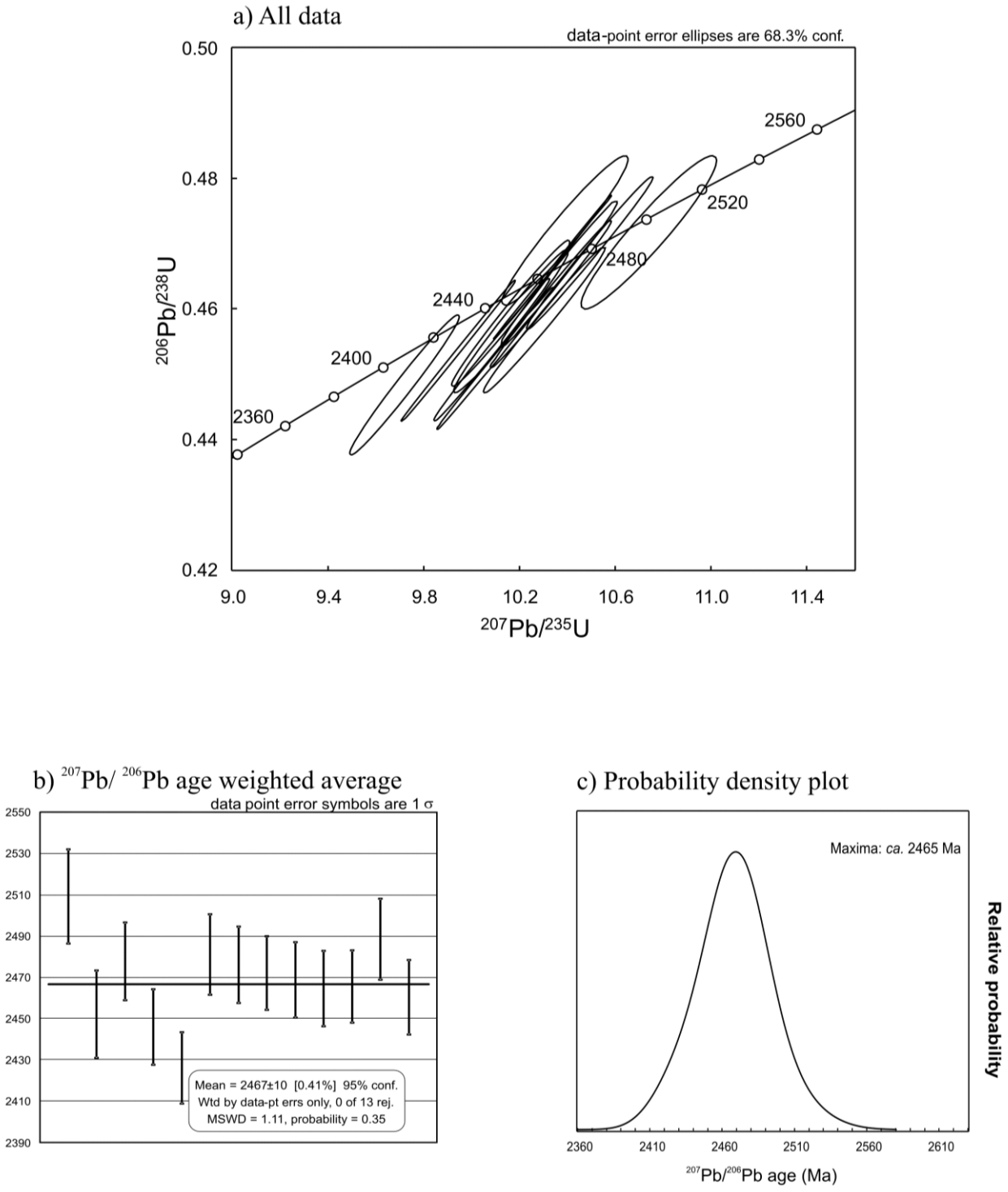

Figure 14: Zircon Cathodoluminescence and monazite backscatter electron images

a) Sample JA7 monazite

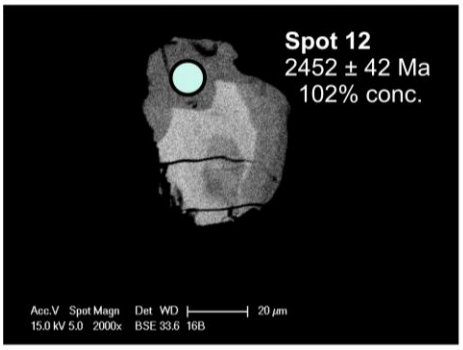

b) Sample JA3 zircon

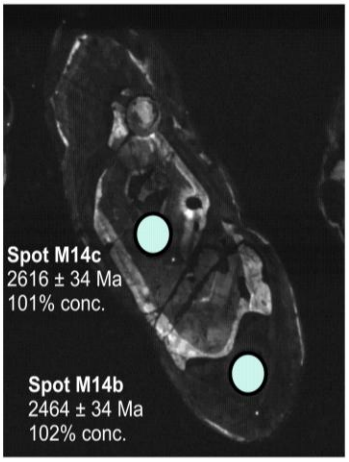

c) Sample JA3 zircon

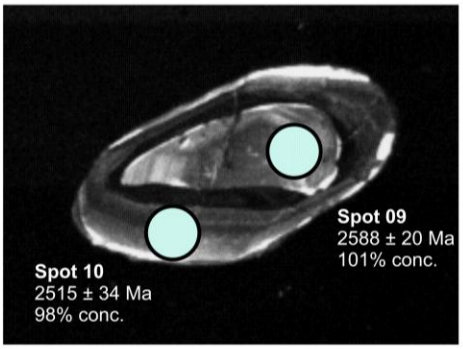

d) Sample JA14 zircon

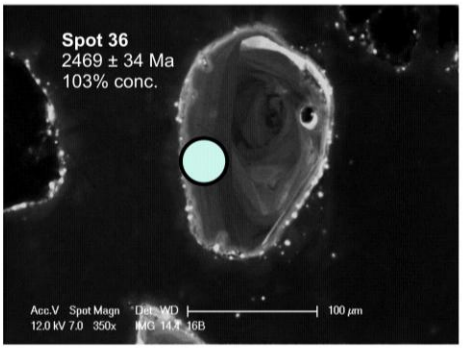

e) Sample JA13 zircon

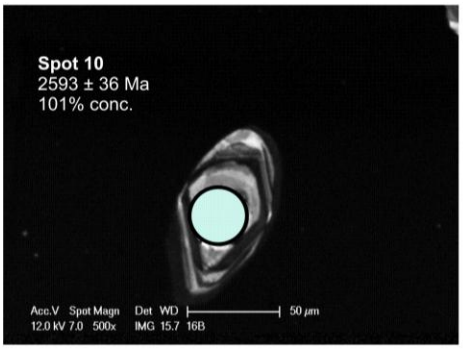

f) Sample JA13 zircon

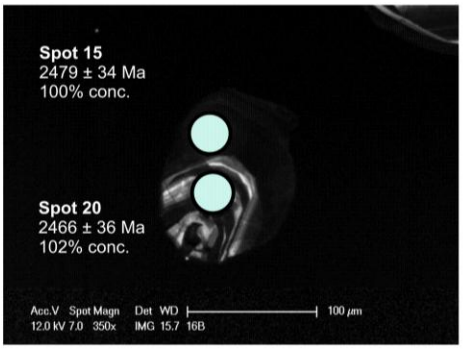

Figure 15: Zircon Th vs. U plots and Th/U vs. age plots

a) JA3- Th vs. U

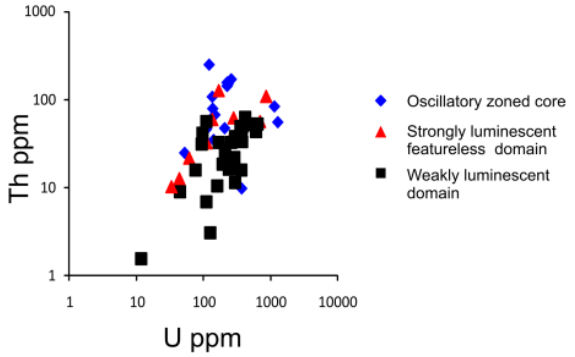

b) JA3- Th/U vs. $^{207}Pb/^{206}Pb$ age

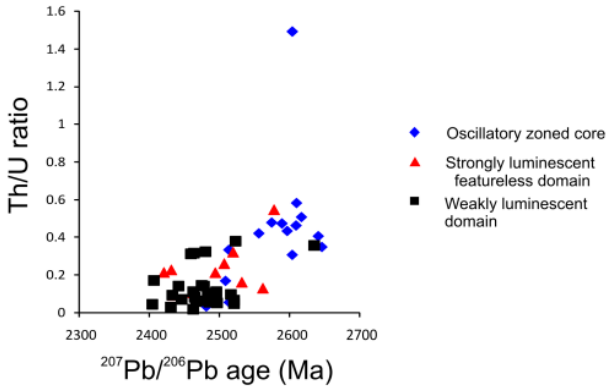

c) JA13- Th vs. U

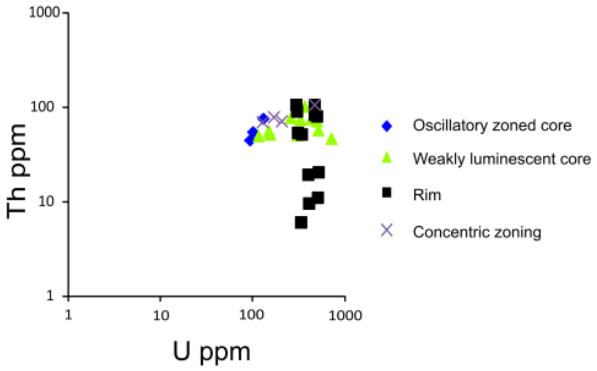

d) JA13- Th/U vs. $^{207}Pb/^{206}Pb$ age

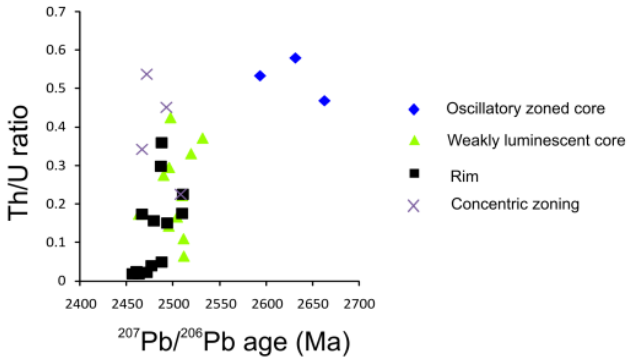

e) JA14- Th vs. U

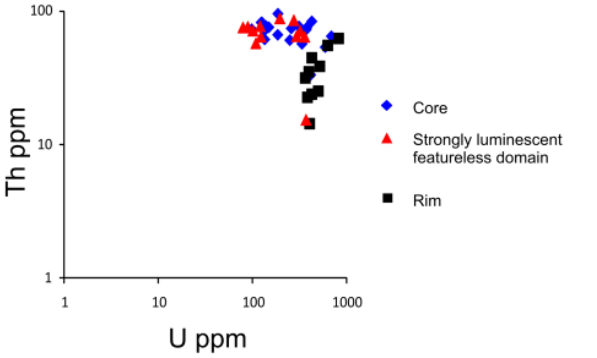

f) JA14- Th/U vs. $^{207}Pb/^{206}Pb$ age

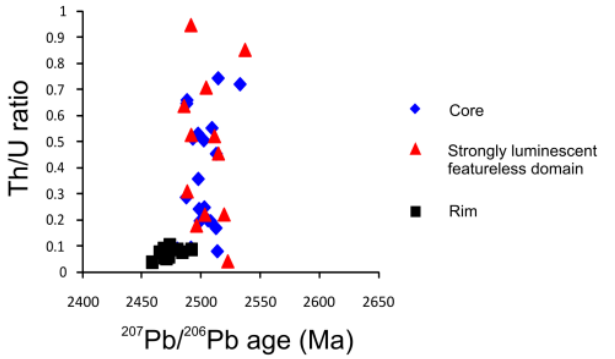

Figure 16: Zircon REE patterns

a) Zircon REE plots for sample JA14

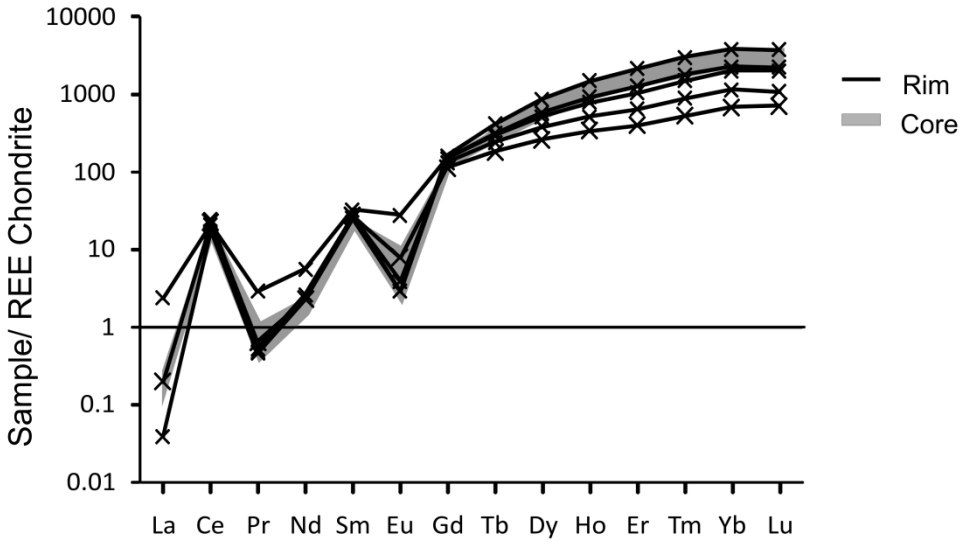

b) Zircon REE plots for JA3

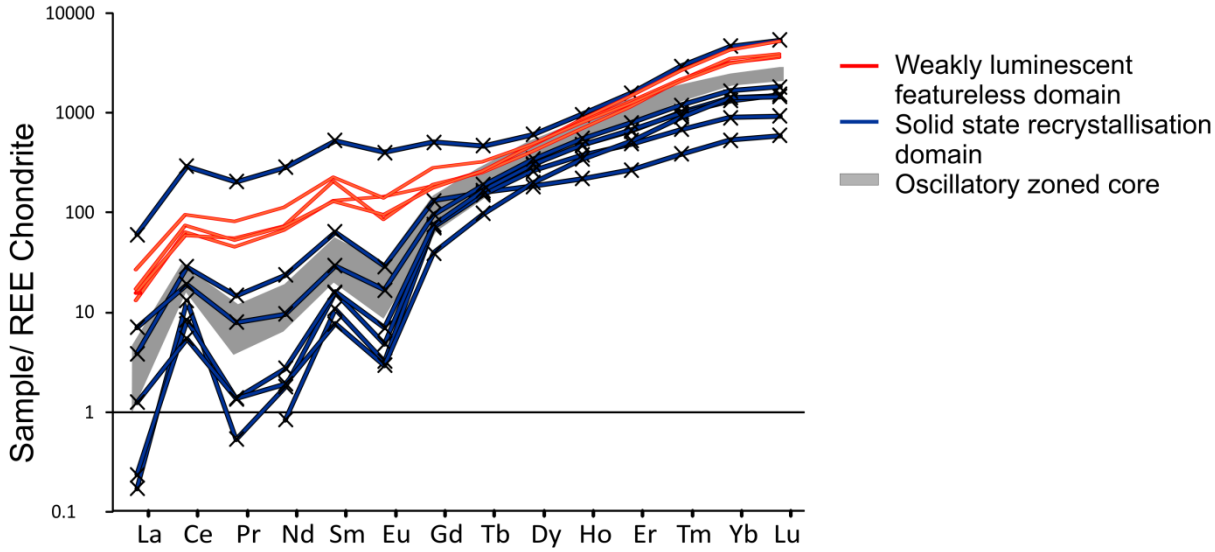

Figure 17

a) *P* (kbar) vs. age (Ma) for >2400 Ma, > 700 °C metamorphism

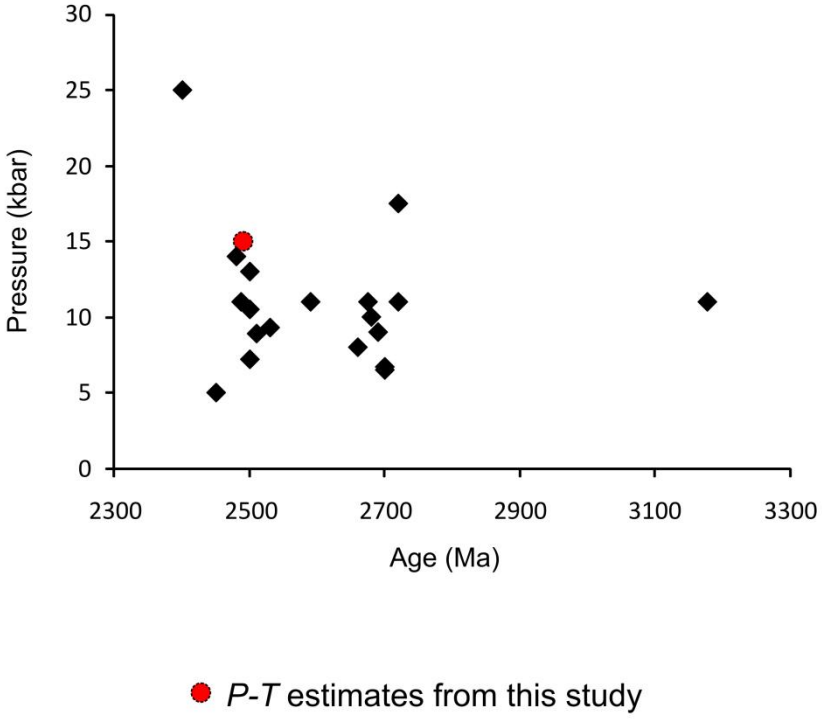

b) Apparent geothermal gradients for >2400 Ma, > 700 °C metamorphism

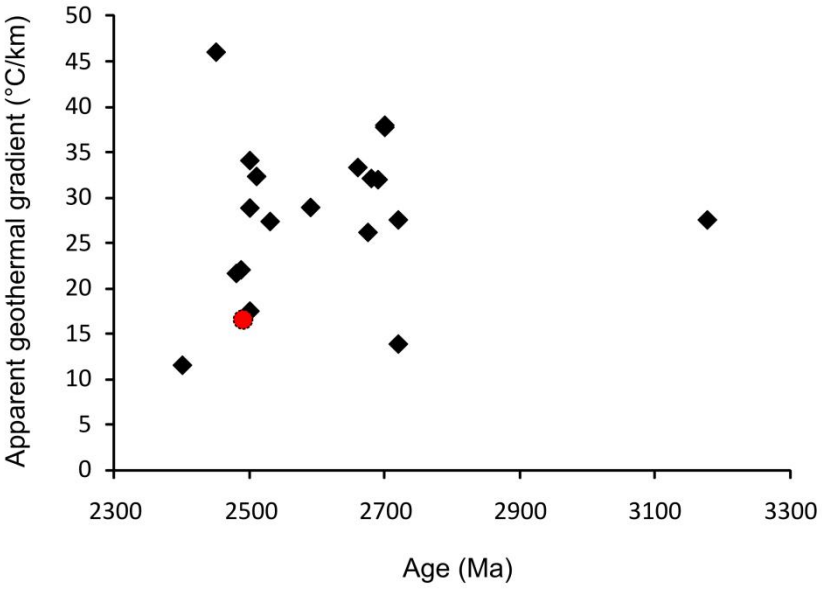

Table 1

Unit and sample number	Spatial distribution	Lithological features	Structural features
Quartz and Magnetite mylonitic gneiss -	East - west trending typically ~ 20-50 m wide ridge extending along the north face of the Kanja Malai Hills. Up to 200 m wide in the east of the hills. No contact with other lithologies is evident.	Elongate quartz and magnetite ribbons between 2-20 cm.	S-L tectonite, foliation is strongly defined (S2) with a subhorizontal east plunging mineral elongation. S-C' fabrics common indicating north block east movement.
Garnet, plagioclase, clinopyroxene, hornblende mafic gneiss and garnet poor gneiss Samples JA10, EM16, EM19, JA9a	East-west trending ~100-200 m wide ridge along the northern face of the Kanja Malai Hills. Garnet poor gneiss variations typically existing as 10-150 m wide east-west trending ridges. Contact between garnet rich and garnet poor variations are gradational, cross cuts felsic gneiss S1 folds.	2-5 cm garnet and clinopyoxene pods surrounded by hornblende, plagioclase and quartz matrix, locally compositionally variable garnet with largest abundance around 2-15 cm wide folded leucosomes.	S1 folds are defined by trails of garnet aggregates. Foliation (S2) is moderate, subvertical-vertical, east-west trending and defined by plagioclase and hornblende. Localised ~50 cm wide east-west trending higher strain domains.
K-feldspar, biotite felsic gneiss Sample JA13	300 m^2 area in contact with garnet bearing felsic gneiss (sample JA14).	K-feldspar, plagioclase, biotite and quartz gneiss with little compositional variation.	S2 subvertical-vertical, east-west to northwest-southeast foliation defined by biotite, no evidence for S1 fabric.
K-feldspar biotite garnet ± orthopyroxene migmatitic felsic gneiss Sample JA14	700 m^2 area in contact with K-feldspar, biotite felsic gneiss (sample JA13).	Folded gneissic layering defined by biotite and comprised of alternating 2-5 cm K-feldspar, plagioclase, garnet bands. Up to 1 cm pods of garnet and orthopyroxene abundant around leucosomes 5-20 cm quartz and feldspar rich leucosomes present throughout the area. Boudinaged 1 m wide mafic dyke in the north of the area.	S1 is represented by closed-tight migmatitic folding. Folded leucosomes cross cut S1 and are post-S1, pre-S2 S2 is typically represented by subvertical-vertical, east-west to northwest-southeast trending axial planes of folded S1 fabric. S2 linear 5-20 cm high strained K-feldspar and quartz leucsomes cross cut S1 along antiformal hinges in areas. East-west trending dyke is boudinaged (S2) and folded with axial trace northeast-southwest (S3).
Proto-mylonitic garnet, biotite felsic gneiss -	10-30 m east-west trending zones.	Gneissic layering consisting of 1-5 cm alternating lighter layers of quartz, feldspar ± garnet, and darker layers of quartz, biotite, feldspar and garnet.	S1 gneissic layering folded into tight-isoclinal, gently to moderately east plunging folds, with axial planes subvertical -vertical, east-west trending and defining S2.
Garnet, plagioclase, biotite ± kyanite gneiss JA3, JA7	East-west trending >250 m wide extending along the northern Kanjamalai Hills. Unit containing intercalated garnet poor mafic gneiss domains.	Folded gneissic layering defined by biotite containing 1-2 cm alternating light quartz, feldspar, garnet, kyanite biotite layers and dark quartz, feldspar bioite rich layers.	Strongly defined S1 folded into steeply plunging west, close-tight folds, S2 is subvertical-vertical and east-west trending defined by axial planes.

Table 2

Sample	JA3							JA7							JA9a						
	grt- core	grt- rim	bt	pl	K-spr	ky	ru	grt- core	grt- rim	bt	pl	K-spr	ru	ky	grt-core	grt- rim	cpx	pl	hb	mt	ilm
Analysis number	22.000	8.000	625.000	684.000	673.000	631.000	2.000	790	781	764	772	802	2	766	15	165	19	8	162	192	299
SiO2	38.672	39.020	37.577	54.679	66.324	36.714	0.054	38.640	37.778	36.455	57.515	63.940	0.054	36.278	39.486	39.336	52.865	57.277	45.223	0.106	0.056
TiO2	0.000	0.057	3.487	0.000	0.037	0.078	96.801	0.049	0.011	3.336	0.000	0.000	96.801	0.000	0.045	0.078	0.385	0.000	1.750	0.000	50.767
Al2O3	21.762	21.691	15.740	28.111	17.646	62.541	0.000	22.088	21.794	16.956	26.709	18.421	0.000	62.344	21.797	21.900	3.408	25.997	11.532	0.000	0.000
Cr2O3	0.039	0.016	0.008	0.030	0.047	0.038	0.004	0.003	0.023	0.000	0.000	0.004	0.004	0.013	0.000	0.000	0.034	0.000	0.122	0.053	0.135
FeO	27.444	28.029	11.241	0.039	0.011	0.706	0.809	26.613	26.811	14.317	0.045	0.127	0.809	0.704	24.316	23.031	6.831	0.199	11.245	76.473	44.791
MnO	0.281	0.278	0.017	0.000	0.024	0.000	0.000	0.5744	0.769	0.000	0.000	0.021	0.000	0.066	0.466	0.661	0.014	0.000	0.025	0.000	0.160
MgO	9.609	8.260	16.664	0.000	0.071	0.030	0.014	8.609	8.183	13.499	0.000	0.000	0.014	0.014	8.201	7.716	13.665	0.000	13.892	0.000	1.933
ZnO	0.000	0.120	0.249	0.000	0.000	0.000	0.196	0.000	0.000	0.188	0.171	0.066	0.196	0.000	0.000	0.069	0.022	0.000	0.140	0.080	0.130
CaO	2.431	3.372	0.003	11.242	0.087	0.012	0.064	3.686	4.051	0.008	8.738	0.024	0.064	0.000	6.432	7.296	22.105	8.298	11.330	0.009	0.210
Na2O	0.000	0.000	0.057	5.236	0.813	0.000	0.000	0.040	0.019	0.047	6.663	0.955	0.000	0.000	0.012	0.000	0.876	6.936	2.083	0.007	0.003
K2O	0.014	0.022	10.029	0.201	14.421	0.000	0.041	0.002	0.013	9.818	0.247	15.332	0.041	0.027	0.000	0.000	0.000	0.051	0.208	0.055	0.013
Total	100.251	100.864	95.071	99.538	99.481	100.120	97.984	100.31	99.450	94.623	100.089	98.890	97.984	99.447	100.755	100.088	100.205	98.759	97.548	76.785	98.197
No. Oxygens	12.000	12.000	11.000	8.000	8.000	5.000	2.000	12.000	12.000	11.000	8.000	8.000	2.000	5.000	12.000	12.000	6.000	8.000	23.000	4.000	3.000
Si	2.975	2.998	2.772	2.480	3.046	0.991	0.001	2.973	2.948	2.738	2.579	2.985	0.001	0.985	3.010	3.012	1.946	2.599	6.577	0.005	0.001
Ti	0.000	0.003	0.193	0.000	0.001	0.002	0.993	0.003	0.001	0.188	0.000	0.000	0.993	0.000	0.003	0.004	0.011	0.000	0.191	0.000	0.965
Al	1.973	1.964	1.368	1.503	0.955	1.989	0.000	1.999	2.004	1.501	1.412	1.014	0.000	1.995	1.958	1.977	0.148	1.390	1.977	0.000	0.000
Cr	0.002	0.001	0.000	0.001	0.002	0.001	0.000	0.000	0.001	0.000	0.000	0.000	0.000	0.000	0.000	0.000	0.001	0.000	0.014	0.002	0.003
Fe3+	-	-	-	-	-	0.025	-	-	-	-	-	-	-	0.035	-	-	0.001	-	-	1.992	0.066
Fe2+	1.765	1.801	0.693	0.001	0.000	-0.009	0.009	1.712	1.750	0.899	0.002	0.005	0.009	-0.019	1.550	1.475	0.209	0.008	1.368	0.994	0.881
Mn2+	0.018	0.018	0.001	0.000	0.001	0.000	0.000	0.037	0.051	0.000	0.000	0.001	0.000	0.002	0.030	0.043	0.000	0.000	0.003	0.000	0.003
Mg	1.102	0.946	1.832	0.000	0.005	0.001	0.000	0.987	0.952	1.512	0.000	0.000	0.000	0.001	0.932	0.881	0.750	0.000	3.012	0.000	0.073
Zn	0.000	0.007	0.014	0.000	0.000	0.000	0.002	0.000	0.00	0.010	0.006	0.002	0.002	0.000	0.000	0.004	0.001	0.000	0.015	0.003	0.002
Ca	0.200	0	0.000	0.546	0.004	0.000	0.001	0.304	0.339	0.001	0.420	0.001	0.001	0.000	0.525	0.599	0.872	0.403	1.765	0.000	0.006
Na	0.000	0.000	0.008	0.460	0.072	0.000	0.000	0.006	0.003	0.007	0.579	0.086	0.000	0.000	0.002	0	0.063	0.610	0.587	0.001	0.000
K	0.001	0.002	0.944	0.012	0.845	0.000	0.001	0.000	0.001	0.941	0.014	0.913	0.001	0.001	0.000	0.000	0.000	0.003	0.039	0.003	0.000
Total Cations (S)	8	8	8	5	5	3	1	8	8	8	5	5	1	3	8	8	4	5	16	4	2
XFe	0.616	0.656	0.275					0.634	0.648	0.373					0.625	0.626	0.218		0.312		
XMg	0.384	0.344	0.725					0.366	0.352	0.627					0.375	0.374	0.782		0.688		
XAlm	0.572	0.592						0.563	0.566						0.510	0.492					
XPy	0.357	0.311						0.325	0.308						0.307	0.294					
XGrs	0.065	0.091						0.100	0.110						0.173	0.200					
XSpss	0.006	0.006						0.012	0.016						0.010	0.014					
XAb																		0.602			
XAn																		0.398			
Fsp XK				0.011	0.917						0.014	0.912									
Fsp XNa				0.452	0.079						0.572	0.086									
Fsp XCa				0.536	0.005						0.414	0.001									

Table 3

Sample	JA10							EM16					EM19						
	grt-core	grt- rim	cpx	pl	hb	mt	ilm	grt-core	grt- rim	cpx	pl	ilm	grt-core	grt- rim	cpx	pl	hb	mt	ru
Analysis number	121	898	147	188	190	194	87	227	266.000	210	256	250	311	307.000	306	312	1013	1004	303
SiO2	38.135	37.170	51.574	59.271	42.055	0.102	0.037	38.273	38.451	50.989	58.239	0.046	39.165	39.160	51.923	56.810	44.048	6.944	0.006
TiO2	0.045	0.036	0.274	0.000	2.001	0.217	48.471	0.065	0.000	0.376	0.000	48.633	0.032	0.015	0.444	0.000	1.693	0.032	98.703
Al2O3	20.910	21.101	3.097	25.206	12.133	0.226	0.000	20.771	20.894	3.574	26.124	0.000	21.457	21.289	3.641	26.435	11.508	0.013	0.000
Cr2O3	0.000	0.012	0.000	0.030	0.008	0.044	0.015	0.000	0.000	0.063	0.000	0.000	0.000	0.103	0.009	0.039	0.087	0.000	0.038
FeO	27.503	29.670	9.951	0.019	14.186	87.457	47.371	27.711	27.512	10.480	0.018	47.385	23.477	23.661	7.031	0.026	10.067	70.423	0.035
MnO	0.617	0.752	0.101	0.000	0.028	0.000	0.112	0.526	0.610	0.098	0.000	0.141	0.714	0.775	0.028	0.021	0.024	0.000	0.000
MgO	5.801	4.128	12.177	0.015	11.252	0.054	1.302	5.817	5.428	11.713	0.000	1.635	8.555	8.357	13.405	0.000	14.376	0.145	0.000
ZnO	0.000	0.032	0.000	0.095	0.000	0.236	0.000	0.000	0.000	0.159	0.000	0.015	0.033	0.000	0.028	0.017	0.060	0.000	0.000
CaO	7.092	7.006	22.021	7.893	11.873	0.025	0.000	7.085	7.488	21.743	8.914	0.016	6.683	6.621	22.485	9.622	11.328	0.415	0.000
Na2O	0.010	0.007	0.954	7.014	1.445	0.001	0.037	0.000	0.000	0.949	6.473	0.000	0.023	0.030	0.852	6.254	1.597	0.058	0.000
K2O	0.000	0.000	0.000	0.234	1.837	0.012	0.000	0.000	0.000	0.000	0.270	0.001	0.000	0.014	0.010	0.054	0.333	0.019	0.002
																		0.000	
Total	100.114	99.914	100.149	99.777	96.818	88.374	97.345	100.248	100.382	100.143	100.038	97.871	100.138	100.024	99.856	99.278	95.121	78.05	98.785
No. Oxygens	12.000	12.000	6.000	8.000	23.000	4.000	3.000	12.000	12.000	6.000	8.000	3.000	12.000	12.000	6.000	8.000	23.000	4	2.000
Si	2.989	2.957	1.920	2.654	6.341	0.004	0.001	2.997	3.006	1.904	2.608	0.001	3.003	3.010	1.919	2.570	6.540	0.378	0.000
Ti	0.003	0.002	0.008	0.000	0.227	0.007	0.932	0.004	0.000	0.011	0.000	0.928	0.002	0.001	0.012	0.000	0.189	0.001	0.999
Al	1.932	1.978	0.136	1.330	2.156	0.011	0.000	1.917	1.925	0.157	1.378	0.000	1.939	1.928	0.159	1.409	2.014	0.001	0.000
Cr	0.000	0.001	0.000	0.001	0.001	0.001	0.000	0.000	0.000	0.002	0.000	0.000	0.000	0.006	0.000	0.001	0.010	0.000	0.000
Fe3+	-	-	0.077	-	-	1.967	0.135	-	-	0.080	-	0.142	-	-	0.039	-	-	3.201	-
Fe2+	1.803	1.974	0.233	0.001	1.789	0.998	0.877	1.815	1.799	0.248	0.001	0.864	1.505	1.521	0.178	0.001	1.250	0.000	0.000
Mn2+	0.041	0.051	0.003	0.000	0.004	0.000	0.002	0.035	0.040	0.003	0.000	0.003	0.046	0.050	0.001	0.001	0.003	0.012	0.000
Mg	0.678	0.490	0.676	0.001	2.529	0.003	0.050	0.679	0.633	0.652	0.000	0.062	0.978	0.958	0.739	0.000	3.182	0.000	0.000
Zn	0.000	0.002	0.000	0.003	0.000	0.007	0.000	0.000	0.000	0.004	0.000	0.000	0.002	0.000	0.001	0.001	0.007	0.024	0.000
Ca	0.596	1	0.878	0.379	1.918	0.001	0.000	0.594	1	0.870	0.428	0.000	0.549	0.545	0.890	0.466	1.802	0.006	0.000
Na	0.001	0.001	0.069	0.609	0.422	0.000	0.002	0.000	0.000	0.069	0.562	0.000	0.003	0.004	0.061	0.548	0.460	0.001	0.000
K	0.000	0.000	0.000	0.013	0.353	0.001	0.000	0.000	0.000	0.000	0.015	0.000	0.000	0.001	0.000	0.003	0.063	0.000	0.000
Total Cations (S)	8	8	4	5	16	4	2	8	8	4	5	2	8	8	4	5	16	4	1
XFe	0.727	0.801	0.256		0.414			0.728	0.740	0.275			0.606	0.614	0.194		0.282		
XMg	0.273	0.199	0.744		0.586			0.272	0.260	0.725			0.394	0.386	0.806		0.718		
XAlm	0.578	0.634						0.581	0.580				0.489	0.495					
XPy	0.217	0.157						0.217	0.204				0.318	0.312					
XGrs	0.191	0.192						0.190	0.202				0.178	0.177					
XSpss	0.013	0.016						0.011	0.013				0.015	0.016					
XAb				0.617							0.568					0.540			
XAn				0.383							0.432					0.460			

Table 4

THERMOCALC Average *P-T* estimates for different water activities

Sample and analysis set	*a* H2O	Average *P* (at 850°C) ± (1 σ)	Average *T* (at 12.5 kbar°C) ± (1 σ)	Average *P-T* ± (1σ)		Sigma fit required for 95% confidence	Calculated sigma fit	Error correlation
JA9a 1	0	12.3 ± 1.72	774 ± 83	11.2 ± 2.2	788 ± 138	1.54	1.13	0.829
JA9a 1	0.25	12 ± 1.55	803 ± 42	11.5 ± 1.2	813 ± 40	1.49	0.99	0.429
JA9a 1	0.5	12 ± 1.71	856 ± 50	12.6 ± 1.5	891 ± 51	1.49	1.08	0.418
JA9a 2	0	10.9 ± 1.27	807 ± 68	8.8 ± 1.3	697 ± 67	1.45	0.93	0.793
JA9a 2	0.25	10.8 ± 1.42	778 ± 42	9.6 ± 1.1	755 ± 32	1.42	0.93	0.381
JA9a 2	0.5	10.9 ± 1.20	826 ± 44	8.8 ± 1.3	815 ± 40	1.42	1.1	0.385
JA10 1	0	12.7 ± 1.65	779 ± 84	12.5 ± 2.0	826 ± 117	1.45	1.5	0.604
JA10 1	0.25	12.6 ± 1.48	777 ± 55	12.1 ± 1.5	798 ± 62	1.42	1.4	0.288
JA10 1	0.5	12.9 ± 1.42	826 ± 62	12.9 ± 1.6	863 ± 71	1.42	1.6	0.309
JA10 2	0	11.7 ± 1.48	802 ± 84	11.1 ± 1.8	787 ± 109	1.45	1.44	0.587
JA10 2	0.25	11.5 ± 1.53	763 ± 55	10.9 ± 1.3	764 ± 56	1.42	1.34	0.27
JA10 2	0.5	11.7 ± 1.38	810 ± 59	11.5 ± 1.5	827 ± 63	1.42	1.36	0.288
EM19 1	0	12.4 ± 1.25	952 ± 89	13.9 ± 1.5	1045 ± 120	1.54	0.99	0.62
EM19 1	0.25	12.1 ± 1.40	807 ± 57	11.9 ± 1.5	816 ± 62	1.49	1.49	0.225
EM19 1	0.5	12.3 ± 1.13	876 ± 50	12.6 ± 1.3	891 ± 58	1.49	1.17	0.22
EM19 2	0	12.2 ± 1.26	958 ± 90	13.8 ± 1.5	1044 ± 121	1.54	1.01	0.613
EM19 2	0.25	11.9 ± 1.41	807 ± 58	11.7 ± 1.5	816 ± 63	1.49	1.52	0.216
EM19 2	0.5	12.2 ± 1.14	877 ± 50	12.4 ± 1.3	890 ± 58	1.49	1.19	0.213

THERMOCALC Fe-Mg thermometer *T* estimates

Sample and analysis set		*P* (kbar)	5	7	9	11	13	15	17	1 σ uncertainty (°C)
JA9a 1	Reaction 1 (grt - cpx)	*T* (°C)	467	476	485	495	504	513	522	90
JA9a 1	Reaction 2 (grt - amph)	*T* (°C)	819	832	845	858	871	885	898	114
JA9a 2	Reaction 1 (grt - cpx)	*T* (°C)	823	837	851	865	879	893	907	141
JA9a 2	Reaction 2 (grt - amph)	*T* (°C)	742	755	767	779	791	803	816	100
JA10 1	Reaction 1 (grt - cpx)	*T* (°C)	751	764	777	790	803	816	829	123
JA10 1	Reaction 2 (grt - amph)	*T* (°C)	688	699	711	722	734	745	756	94
JA10 2	Reaction 1 (grt - cpx)	*T* (°C)	823	838	852	866	880	894	908	142
JA10 2	Reaction 2 (grt - amph)	*T* (°C)	734	747	759	771	783	795	807	102
EM19 1	Reaction 1 (grt - cpx)	*T* (°C)	865	880	894	909	924	938	953	155
EM19 1	Reaction 2 (grt - amph)	*T* (°C)	878	892	906	920	934	948	962	121
EM19 2	Reaction 1 (grt - cpx)	*T* (°C)	872	886	901	916	931	945	960	156
EM 19 2	Reaction 2 (grt - amph)	*T* (°C)	875	888	902	916	930	944	958	120

Reaction 1: 3di + alm = 3hed + py

Reaction 2: 5py + 3fact = 5alm +3tr

THERMOCALC barometer *P* estimates (grossular + quartz + 2kyanite = 3 anorthite)

Sample	*T* (°C)	600	640	680	720	760	800	840	880	920	960	1000	1 σ uncertainty (kbar)
JA3		7.3	7.9	8.5	9.2	9.8	10.4	11.1	11.7	12.3	13	13.6	0.95
JA7		8.5	9.2	9.9	10.6	11.3	12	12.7	13.4	14	14.7	15.5	0.62

Table 5

Sample JA3			Isotope Ratios									Ages (Ma)									
Spot name	^{204}Pb (cps)	Th/U	^{207}Pb/^{206}Pb	± 1σ	^{206}Pb/^{238}U	± 1σ	^{207}Pb/^{235}U	± 1σ	^{208}Pb/^{232}Th	± 1σ	rho	^{207}Pb/^{206}Pb	± 1σ	^{206}Pb/^{238}U	± 1σ	^{207}Pb/^{235}U	± 1σ	^{208}Pb/^{232}Th	± 1σ	Conc. (%)	Eff. Age*
JA3-01	14	0.581	0.1735	0.0018	0.5067	0.0070	12.1136	0.1628	0.0995	0.0011	0.9773	2591.7	17.61	2642.7	29.8	2613.2	12.61	1917.1	20.73	102	2591.7
JA3-02	46	0.120	0.1621	0.0017	0.5070	0.0070	11.3276	0.1553	0.1203	0.0022	0.9943	2477.9	17.95	2643.9	29.88	2550.5	12.79	2296.1	39.81	107	2477.9
JA3-03	30	0.131	0.1621	0.0016	0.4630	0.0063	10.3472	0.1359	0.1108	0.0014	0.9697	2477.5	16.71	2452.9	27.63	2466.3	12.16	2123.4	25.76	99	2477.5
JA3-04	21	0.283	0.1637	0.0018	0.4726	0.0066	10.6626	0.1485	0.1113	0.0017	0.9954	2493.7	18.47	2495	28.69	2494.2	12.93	2132.4	30.66	100	2493.7
JA3-05	35	0.217	0.1674	0.0017	0.4963	0.0066	11.4525	0.1498	0.1294	0.0016	0.9820	2531.4	16.82	2597.8	28.49	2560.7	12.21	2458.6	29.21	103	2531.4
JA3-06	35	0.122	0.1627	0.0017	0.4747	0.0062	10.6400	0.1365	0.1433	0.0026	0.9808	2483.6	17.23	2504.1	27.17	2492.2	11.91	2706.6	45.86	101	2483.6
JA3-07	47	0.125	0.1580	0.0016	0.4541	0.0063	9.8909	0.1313	0.1375	0.0021	0.9598	2433.9	16.55	2413.6	27.83	2424.7	12.24	2604.4	36.62	99	2433.9
JA3-08	34	0.121	0.1636	0.0017	0.4669	0.0062	10.5270	0.1366	0.1397	0.0023	0.9723	2493.1	16.88	2470	27.38	2482.3	12.03	2642.9	40.96	99	2493.1
JA3-09	26	0.576	0.1745	0.0020	0.5119	0.0073	12.3104	0.1767	0.1195	0.0019	0.9937	2601.2	18.85	2664.7	31.13	2628.4	13.48	2281.7	34.65	102	2601.2
JA3-10	22	0.626	0.1753	0.0018	0.5081	0.0069	12.2775	0.1638	0.1312	0.0014	0.9896	2608.6	16.73	2648.7	29.28	2625.9	12.53	2491.2	24.32	102	2608.6
JA3-11+	33	0.043	0.1624	0.0016	0.3964	0.0055	8.8726	0.1205	0.1191	0.0016	0.9734	2480.7	16.52	2152.3	25.55	2325	12.39	2275.2	29.07	87	2480.7
JA3-12	6	0.451	0.1655	0.0018	0.5174	0.0074	11.8010	0.1682	0.1181	0.0015	0.9911	2512.9	17.93	2688	31.63	2588.7	13.34	2256.9	27.31	107	2512.9
JA3-13	4	0.073	0.1656	0.0017	0.4092	0.0056	9.3427	0.1263	0.1242	0.0017	0.9914	2513.4	16.86	2211.1	25.52	2372.2	12.4	2366.2	29.84	88	2513.4
JA3-14	19	2.023	0.1747	0.0018	0.5036	0.0067	12.1301	0.1629	0.1072	0.0011	0.9951	2603.3	17.35	2629.4	28.85	2614.5	12.6	2058.5	20.07	101	2603.3
JA3-15	22	0.089	0.1662	0.0017	0.4952	0.0066	11.3508	0.1502	0.1358	0.0018	0.9977	2520.1	16.93	2593.3	28.34	2552.4	12.35	2573.7	31.35	103	2520.1
JA3-16	30	0.352	0.1649	0.0020	0.4976	0.0068	11.3133	0.1632	0.1275	0.0022	0.9433	2506.4	20.04	2603.6	29.14	2549.3	13.46	2426.1	38.97	104	2506.4
JA3-17	20	0.434	0.1661	0.0018	0.4873	0.0065	11.1620	0.1504	0.1268	0.0015	0.9911	2519.0	17.59	2559.1	28.21	2536.7	12.56	2412.2	26.5	102	2519
JA3-18	26	0.129	0.1732	0.0018	0.5052	0.0071	12.0627	0.1669	0.1135	0.0012	0.9903	2588.5	17.23	2636.1	30.22	2609.3	12.98	2173.1	22.07	102	2588.5
JA3-19	31	0.388	0.1659	0.0017	0.4674	0.0062	10.6872	0.1406	0.1142	0.0014	0.9997	2516.3	16.97	2472.2	27.01	2496.3	12.21	2186.4	24.99	98	2516.3
JA3-20	18	0.151	0.1689	0.0019	0.5388	0.0075	12.5378	0.1758	0.1407	0.0020	0.9887	2546.5	18.39	2778.5	31.29	2645.6	13.19	2659.8	36.22	109	2546.5
JA3-21	19	0.516	0.1606	0.0016	0.4930	0.0066	10.9184	0.1425	0.1305	0.0016	0.9797	2462.3	16.75	2583.8	28.35	2516.2	12.14	2478.8	28.05	105	2462.3
JA3-22	10	0.739	0.1665	0.0018	0.4249	0.0056	9.7519	0.1301	0.1276	0.0016	0.9930	2522.4	18.05	2282.5	25.45	2411.6	12.29	2427.1	28.61	90	2522.4
JA3-23	13	0.080	0.1720	0.0018	0.4716	0.0066	11.1810	0.1553	0.1130	0.0013	0.9956	2577.2	17.72	2490.6	28.83	2538.3	12.95	2163	24.38	97	2577.2
JA3-24	16	0.082	0.1631	0.0016	0.4422	0.0058	9.9457	0.1286	0.1258	0.0015	0.9788	2488.3	16.58	2360.6	26.1	2429.8	11.93	2395.6	27.69	95	2488.3
JA3-25	6	0.123	0.1610	0.0016	0.4632	0.0061	10.2823	0.1325	0.1221	0.0015	0.9784	2466.3	16.6	2453.7	26.88	2460.5	11.92	2329.1	27.18	99	2466.3
JA3-26	10	0.094	0.1632	0.0017	0.4650	0.0062	10.4676	0.1394	0.1204	0.0019	0.9925	2489.5	17.34	2461.8	27.46	2477.1	12.34	2297	34.3	99	2489.5
JA3-27	19	0.085	0.1633	0.0016	0.4881	0.0066	10.9867	0.1460	0.1337	0.0019	0.9856	2489.8	16.87	2562.5	28.52	2522	12.36	2535.8	33.1	103	2489.8
JA3-28	17	0.528	0.1622	0.0016	0.4625	0.0061	10.3412	0.1331	0.1266	0.0016	0.9789	2478.3	16.6	2450.8	26.81	2465.8	11.91	2408.8	27.98	99	2478.3
JA3-29	13	0.569	0.1645	0.0018	0.4695	0.0065	10.6474	0.1494	0.1173	0.0016	0.9898	2502.8	18.42	2481.5	28.62	2492.9	13.02	2242.2	28.32	99	2502.8
JA3-30	14	0.071	0.1698	0.0018	0.5144	0.0072	12.0437	0.1677	0.1295	0.0019	0.9996	2555.6	17.84	2675.2	30.46	2607.8	13.06	2461.7	34.65	105	2555.6
JA3-31	20	0.113	0.1639	0.0016	0.4747	0.0065	10.7297	0.1440	0.1323	0.0021	0.9832	2496.3	16.76	2504.2	28.33	2500	12.47	2511.3	37.93	100	2496.3
JA3-32	6	0.788	0.1637	0.0017	0.4828	0.0063	10.9005	0.1410	0.1357	0.0021	0.9883	2494.5	16.86	2539.5	27.49	2514.7	12.03	2572.4	36.82	102	2494.5
JA3-33	19	0.549	0.1753	0.0019	0.5090	0.0070	12.3071	0.1698	0.1350	0.0020	0.9956	2609.3	17.8	2652.2	29.87	2628.1	12.95	2560.2	34.66	102	2609.3
JA3-34	19	3.287	0.1786	0.0019	0.5639	0.0075	13.8920	0.1848	0.1563	0.0023	0.9933	2640.3	17.7	2882.9	30.71	2742.4	12.6	2935	40.71	109	2640.3
JA3-35	17	0.415	0.1734	0.0018	0.5120	0.0068	12.2415	0.1621	0.1326	0.0017	0.9987	2590.9	17.5	2665	28.86	2623.1	12.43	2517.4	30.15	103	2590.9
JA3-36	18	0.227	0.1747	0.0021	0.5201	0.0074	12.5292	0.1827	0.1303	0.0027	0.9720	2603.2	19.4	2699.5	31.27	2644.9	13.71	2475.4	48.06	104	2603.2
JA3-37	28	0.472	0.1651	0.0018	0.4862	0.0066	11.0654	0.1509	0.1289	0.0024	0.9982	2508.1	17.8	2554.1	28.8	2528.7	12.7	2450.5	42.09	102	2508.1
JA3-38	19	0.098	0.1792	0.0023	0.4818	0.0070	11.9049	0.1824	0.1128	0.0024	0.9512	2645.4	21.04	2535	30.53	2596.9	14.35	2160	42.62	96	2645.4
JA3-39	15	0.302	0.1635	0.0017	0.4648	0.0063	10.4745	0.1402	0.1120	0.0019	0.9826	2491.8	16.89	2460.6	27.86	2477.7	12.4	2146.3	33.9	99	2491.8
JA3-40+	33	0.197	0.1641	0.0021	0.5193	0.0080	11.6978	0.1829	0.1058	0.0024	0.9802	2497.9	21.73	2696	33.76	2580.5	14.63	2033.4	43.19	108	2497.9
JA3-41	31	0.647	0.1587	0.0017	0.5213	0.0074	11.3932	0.1570	0.1141	0.0019	0.9735	2441.8	17.69	2704.6	31.26	2555.9	12.86	2183.8	33.96	111	2441.8
JA3-42	23	0.174	0.1717	0.0018	0.4991	0.0067	11.8058	0.1566	0.1306	0.0016	0.9838	2573.9	17.04	2609.9	28.93	2589.1	12.42	2480.8	28.15	101	2573.9
JA3-43	11	0.687	0.1628	0.0017	0.4714	0.0066	10.5748	0.1442	0.1102	0.0018	0.9712	2485.2	17.26	2489.7	29.02	2486.5	12.65	2112.5	32.68	100	2485.2
JA3-44	20	0.571	0.1761	0.0018	0.5061	0.0068	12.2870	0.1631	0.1344	0.0018	0.9839	2616.3	17.01	2640	29.22	2626.6	12.47	2548	31.31	101	2616.3
JA3-45	7	0.719	0.1682	0.0020	0.4785	0.0068	11.0907	0.1641	0.1324	0.0024	0.9659	2539.8	19.94	2520.6	29.81	2530.8	13.78	2513	42.68	99	2539.8
JA3-46	12	0.063	0.1784	0.0021	0.5269	0.0076	12.9530	0.1909	0.1340	0.0023	0.9775	2637.5	19.47	2728.4	32.05	2676.2	13.89	2542.3	40.34	103	2637.5
JA3-47	17	0.587	0.1628	0.0017	0.5349	0.0076	12.0127	0.1665	0.1520	0.0031	0.9769	2485.3	16.94	2762	31.86	2605.4	12.99	2859.1	53.78	111	2485.3

Table 6

Sample JA3 continued			Isotope Ratios									Ages (Ma)									
Spot name	^{204}Pb (cps)	Th/U	^{207}Pb/^{206}Pb	± 1σ	^{206}Pb/^{238}U	± 1σ	^{207}Pb/^{235}U	± 1σ	^{208}Pb/^{232}Th	± 1σ	rho	^{207}Pb/^{206}Pb	± 1σ	^{206}Pb/^{238}U	± 1σ	^{207}Pb/^{235}U	± 1σ	^{208}Pb/^{232}Th	± 1σ	Conc. (%)	Eff. Age*
JA3-48	22	0.587	0.1740	0.0018	0.5004	0.0069	12.0007	0.1621	0.1295	0.0020	0.9780	2596	17.08	2615.5	29.69	2604.5	12.66	2461.5	34.9	101	2596
JA3-49	4	0.548	0.1778	0.0020	0.4917	0.0069	12.0499	0.1691	0.1284	0.0022	0.9959	2632.3	18.47	2578	29.71	2608.3	13.15	2442.2	39.23	98	2632.3
JA3-50	14	0.191	0.1621	0.0017	0.4917	0.0070	10.9842	0.1523	0.1105	0.0023	0.9768	2477.3	17.43	2577.8	30.17	2521.8	12.91	2118.9	42.6	104	2477.3
JA3-51	13	0.436	0.1623	0.0021	0.4371	0.0065	9.7811	0.1498	0.0900	0.0023	0.9757	2479.7	21.1	2337.7	29.3	2414.4	14.1	1741.5	42.86	94	2479.7
JA3-52	25	0.450	0.1616	0.0022	0.4569	0.0066	10.1741	0.1581	0.1233	0.0025	0.9241	2472	22.86	2425.9	29.04	2450.7	14.37	2349.6	44.64	98	2472
JA3-53	26	0.142	0.1607	0.0019	0.4160	0.0056	9.2121	0.1282	0.1253	0.0031	0.9586	2462.7	20.07	2242.2	25.26	2359.3	12.75	2385.8	55.26	91	2462.7
JA3-54	9	0.176	0.1704	0.0019	0.4553	0.0062	10.6946	0.1459	0.1395	0.0024	0.9931	2561.3	18.07	2418.8	27.34	2497	12.67	2639.5	42.09	94	2561.3
JA3-55	12	0.107	0.1587	0.0016	0.4881	0.0069	10.6727	0.1455	0.1114	0.0023	0.9600	2441.7	17.3	2562.4	30.04	2495	12.65	2135	41.99	105	2441.7
JA3-56^{+}	21	0.429	0.1607	0.0024	0.4553	0.0069	10.0922	0.1688	0.1210	0.0033	0.9022	2463.4	24.67	2418.9	30.42	2443.3	15.45	2309.4	59.15	98	2463.4
JA3-57	4	0.193	0.1587	0.0018	0.4850	0.0070	10.6092	0.1515	0.1235	0.0026	0.9950	2441.6	18.71	2549.2	30.22	2489.5	13.25	2352.9	46.58	104	2441.6
JA3-58	10	0.109	0.1609	0.0016	0.4767	0.0066	10.5708	0.1419	0.1256	0.0021	0.9721	2464.7	16.96	2512.7	28.74	2486.2	12.45	2390.7	37.33	102	2464.7
JA3-59	33	0.470	0.1733	0.0025	0.4910	0.0076	11.7349	0.1962	0.1374	0.0034	0.9209	2590	23.83	2575.2	32.69	2583.5	15.64	2602.6	60.22	99	2590
JA3-60	28	0.045	0.1640	0.0016	0.4841	0.0068	10.9437	0.1493	0.1264	0.0024	0.9782	2497.3	16.72	2545	29.3	2518.4	12.69	2406.1	43.77	102	2497.3
JA3-61^{+}	25	0.143	0.1638	0.0021	0.4943	0.0076	11.1765	0.1760	0.1601	0.0071	0.9702	2495.3	21.58	2589.2	32.56	2538	14.67	3001	122.9	104	2495.3
JA3-62	18	0.485	0.1781	0.0021	0.5270	0.0075	12.9349	0.1865	0.1413	0.0030	0.9858	2634.9	19.32	2728.8	31.63	2674.9	13.59	2672	53.54	104	2634.9
JA3-63	5	0.150	0.1639	0.0017	0.4885	0.0066	11.0322	0.1466	0.1273	0.0023	0.9807	2495.8	17.12	2564.1	28.68	2525.9	12.37	2421.1	41.56	103	2495.8
JA3-64	12	0.142	0.1638	0.0017	0.4537	0.0063	10.2402	0.1399	0.1192	0.0024	0.9837	2494.7	17.34	2411.7	27.92	2456.7	12.64	2276	43.69	97	2494.7
JA3-65^{+}	7	0.038	0.1576	0.0017	0.4795	0.0068	10.4110	0.1449	0.1533	0.0047	0.9889	2430.3	18.33	2525	29.41	2472	12.9	2881.9	82.84	104	2430.3
JA3-66^{+}	21	0.024	0.1607	0.0020	0.4567	0.0066	10.1094	0.1515	0.1952	0.0099	0.9641	2462.6	20.98	2424.8	29.22	2444.8	13.85	3603.4	167.58	98	2462.6
JA3-67^{+}	25	0.083	0.1677	0.0044	0.5829	0.0119	13.4421	0.3485	0.3691	0.0252	0.7855	2534.7	42.97	2960.4	48.35	2711.2	24.5	6349.2	371.4	117	2534.7
JA3-68	14	0.096	0.1591	0.0019	0.4761	0.0070	10.4173	0.1550	0.1476	0.0040	0.9822	2446.3	20.18	2510.4	30.41	2472.6	13.79	2783.1	69.75	103	2446.3
JA3-69^{+}	20	0.062	0.1553	0.0023	0.4851	0.0075	10.3777	0.1731	0.1769	0.0093	0.9291	2404.6	24.83	2549.6	32.64	2469.1	15.45	3292.1	159.19	106	2404.6
JA3-70^{+}	17	0.263	0.2014	0.0054	0.4363	0.0091	12.1108	0.3196	0.1973	0.0100	0.7878	2837.4	43.4	2334	40.73	2613	24.75	3639.8	168.52	82	2837.4
JA3-71^{+}	46	0.066	0.1663	0.0019	0.4683	0.0067	10.7222	0.1563	0.1504	0.0048	0.9861	2520.9	18.77	2476.1	29.53	2499.3	13.54	2832.1	84.08	98	2520.9
JA3-72^{+}	21	0.075	0.1716	0.0042	0.5320	0.0105	12.5885	0.3126	0.3194	0.0264	0.7971	2573	40.72	2749.8	44.29	2649.4	23.36	5602.5	405.08	107	2573
JA3-73^{+}	15	0.073	0.1628	0.0057	0.5778	0.0141	12.9559	0.4334	0.3631	0.0487	0.7275	2485.3	57.48	2939.6	57.44	2676.5	31.53	6261.5	722.06	118	2485.3
JA3-74	16	0.425	0.1603	0.0020	0.4303	0.0061	9.5087	0.1398	0.1223	0.0024	0.9593	2458.7	20.73	2307.1	27.34	2388.4	13.51	2332.7	43.03	94	2458.7
JA3-75^{+}	0	0.233	0.1554	0.0085	0.5233	0.0179	11.2016	0.5665	0.1440	0.0238	0.6752	2406.4	89.91	2713.1	75.64	2540	47.14	2718.9	419.98	113	2406.4
JA3-76	12	0.197	0.1618	0.0018	0.4744	0.0067	10.5795	0.1506	0.1262	0.0031	0.9967	2475	18.43	2502.8	29.43	2486.9	13.2	2401.7	54.7	101	2475
JA3-77	40	0.121	0.1579	0.0016	0.4498	0.0063	9.7859	0.1300	0.0841	0.0013	0.9562	2433	17.09	2394.1	27.79	2414.8	12.24	1632.2	23.66	98	2433
JA3-78	23	0.154	0.1565	0.0016	0.4811	0.0068	10.3827	0.1403	0.1165	0.0019	0.9558	2418.6	17.19	2532.1	29.61	2469.5	12.51	2226.8	34.29	105	2418.6
JA3-79	5	0.158	0.1596	0.0016	0.4855	0.0066	10.6810	0.1405	0.1316	0.0021	0.9748	2451.2	17.08	2551.3	28.44	2495.8	12.21	2498.7	37.92	104	2451.2
JA3-80	3	0.200	0.1606	0.0017	0.4883	0.0070	10.8131	0.1496	0.1174	0.0021	0.9707	2462.4	17.63	2563.2	30.13	2507.2	12.86	2243.6	38.01	104	2462.4
JA3-81	23	0.137	0.1626	0.0016	0.5023	0.0067	11.2627	0.1447	0.1314	0.0019	0.9648	2483.3	16.57	2623.8	28.7	2545.1	11.98	2494.9	33.39	106	2483.3
JA3-82	28	0.529	0.1776	0.0020	0.5207	0.0071	12.7477	0.1759	0.1344	0.0020	0.9937	2630.8	18.14	2702.1	30.28	2661.2	12.99	2548.5	34.73	103	2630.8
JA3-83^{+}	53	0.219	0.1537	0.0030	0.5617	0.0104	11.9847	0.2371	0.0858	0.0038	0.9358	2387.7	32.46	2873.5	42.95	2603.2	18.54	1664.4	69.98	120	2387.7
JA3-84	11	0.294	0.1577	0.0023	0.4704	0.0072	10.2176	0.1686	0.0949	0.0023	0.9262	2431.2	24.8	2485.3	31.51	2454.7	15.26	1833.2	42.28	102	2431.2
JA3-85	18	0.281	0.1567	0.0023	0.4519	0.0069	9.7594	0.1612	0.0929	0.0024	0.9232	2420.7	24.63	2403.5	30.58	2412.3	15.21	1795.1	43.62	99	2420.7
JA3-87	21	0.473	0.1577	0.0024	0.5033	0.0075	10.9384	0.1825	0.1425	0.0034	0.8955	2430.9	25.37	2627.8	32.23	2517.9	15.52	2693.1	60.5	108	2430.9
JA3-88^{+}	7	0.205	0.1870	0.0042	0.6225	0.0120	16.0433	0.3692	0.3113	0.0144	0.8384	2716.1	36.69	3119.7	47.72	2879.4	22	5478.5	221.99	115	2716.1
JA3-89^{+}	20	0.344	0.1685	0.0026	0.6613	0.0104	15.3601	0.2690	0.1773	0.0050	0.9006	2542.9	25.76	3272.2	40.49	2837.8	16.7	3299.7	86	129	2542.9

Table 7

Sample JA13			Isotope Ratios									Ages (Ma)									
Spot name	^{204}Pb (cps)	Th/U	^{207}Pb/^{206}Pb	± 1σ	^{206}Pb/^{238}U	± 1σ	^{207}Pb/^{235}U	± 1σ	^{208}Pb/^{232}Th	± 1σ	rho	^{207}Pb/^{206}Pb	± 1σ	^{206}Pb/^{238}U	± 1σ	^{207}Pb/^{235}U	± 1σ	^{208}Pb/^{232}Th	± 1σ	Conc. (%)	Eff. Age*
JA13- 01	7	0.015	0.1607	0.0016	0.4645	0.0060	10.2897	0.1324	0.1271	0.0028	0.9947	2463	16.95	2459.3	26.47	2461.2	11.91	2418.5	50.79	100	2463
JA13- 02	48	0.087	0.1602	0.0016	0.3399	0.0043	7.5071	0.0957	0.1112	0.0014	0.9989	2457.7	17.09	1886.2	20.81	2173.8	11.43	2130.6	25.46	77	2457.7
JA13- 03	48	0.073	0.1509	0.0016	0.2434	0.0034	5.0607	0.0709	0.0733	0.0014	0.9943	2356.2	18	1404.5	17.77	1829.5	11.88	1429.4	26.35	60	2356.2
JA13- 04	9	0.018	0.1601	0.0017	0.4332	0.0057	9.5632	0.1272	0.1278	0.0035	0.9960	2456.9	17.38	2320.2	25.8	2393.6	12.23	2430.6	63.3	94	2456.9
JA13- 05	40	0.451	0.1636	0.0018	0.4595	0.0063	10.3595	0.1441	0.1134	0.0015	0.9870	2492.9	18.08	2437.2	27.86	2467.4	12.88	2170.9	26.34	98	2492.9
JA13- 06	43	0.536	0.1615	0.0018	0.4548	0.0064	10.1253	0.1458	0.1114	0.0016	0.9773	2471.5	19.12	2416.4	28.34	2446.3	13.31	2135.1	28.35	98	2471.5
JA13- 07	14	0.297	0.1630	0.0017	0.4603	0.0061	10.3426	0.1376	0.1166	0.0013	0.9990	2486.8	17.16	2440.9	27.01	2465.9	12.32	2229.3	24.3	98	2486.8
JA13- 08	29	0.170	0.1638	0.0017	0.3737	0.0052	8.4391	0.1175	0.1153	0.0017	0.9995	2495.5	17.71	2046.6	24.38	2279.4	12.64	2205	30.66	82	2495.5
JA13- 09	0	0.330	0.1662	0.0018	0.4613	0.0062	10.5697	0.1434	0.1226	0.0016	0.9877	2519.5	17.73	2445.4	27.24	2486.1	12.58	2337.1	28.38	97	2519.5
JA13- 10	4	0.016	0.1544	0.0016	0.4632	0.0069	9.8573	0.1412	0.0935	0.0039	0.9674	2395.1	17.6	2453.8	30.21	2421.5	13.21	1806.2	71.17	102	2395.1
JA13- 11	5	0.166	0.1647	0.0017	0.4607	0.0062	10.4583	0.1417	0.1272	0.0017	0.9983	2504.3	17.22	2442.6	27.51	2476.2	12.55	2420.4	31.06	98	2504.3
JA13- 12	11	0.089	0.1581	0.0017	0.3584	0.0047	7.8114	0.1026	0.1338	0.0022	0.9923	2435.8	17.58	1974.5	22.17	2209.5	11.82	2537.3	39.85	81	2435.8
JA13- 13	33	0.039	0.1620	0.0016	0.4651	0.0066	10.3961	0.1461	0.1239	0.0022	0.9934	2477.1	17.02	2462.1	28.93	2470.7	13.02	2360	39.37	99	2477.1
JA13- 14	12	0.295	0.1639	0.0017	0.4710	0.0064	10.6390	0.1448	0.1256	0.0015	0.9981	2495.8	17.14	2487.8	28.14	2492.1	12.63	2391.8	27.1	100	2495.8
JA13- 15	18	0.024	0.1605	0.0016	0.4709	0.0064	10.4197	0.1411	0.1285	0.0026	0.9935	2460.9	16.98	2487.5	28.15	2472.8	12.55	2443.6	45.97	101	2460.9
JA13- 16	21	0.580	0.1777	0.0019	0.5085	0.0073	12.4565	0.1798	0.1241	0.0017	0.9894	2631.3	17.99	2650	31.05	2639.4	13.56	2363.9	30.37	101	2631.3
JA13- 17	26	0.065	0.1654	0.0017	0.4833	0.0063	11.0178	0.1432	0.1412	0.0022	0.9935	2511.7	16.91	2541.4	27.48	2524.6	12.1	2670.4	39.09	101	2511.7
JA13- 18	10	0.173	0.1610	0.0017	0.4895	0.0068	10.8673	0.1490	0.1203	0.0017	0.9942	2466.5	17.16	2568.4	29.23	2511.8	12.75	2296.5	29.69	104	2466.5
JA13- 19	13	0.424	0.1640	0.0018	0.4912	0.0069	11.1065	0.1563	0.1225	0.0016	0.9921	2497.3	17.92	2575.9	29.66	2532.1	13.11	2335.9	29.01	103	2497.3
JA13- 20	10	0.274	0.1633	0.0017	0.4970	0.0069	11.1880	0.1552	0.1253	0.0016	0.9949	2489.8	17.14	2601	29.86	2538.9	12.93	2386.6	29.29	104	2489.8
JA13- 21	4	0.022	0.1615	0.0016	0.4711	0.0065	10.4896	0.1440	0.1185	0.0026	0.9891	2471.4	16.92	2488.4	28.68	2479	12.73	2262.5	46.86	101	2471.4
JA13- 22	10	0.533	0.1737	0.0019	0.5021	0.0072	12.0237	0.1731	0.1254	0.0018	0.9891	2593.7	18.13	2622.7	30.7	2606.3	13.5	2388.4	32.39	101	2593.7
JA13- 23	17	0.173	0.1607	0.0017	0.4686	0.0068	10.3795	0.1491	0.1167	0.0019	0.9912	2463	17.28	2477.2	29.8	2469.2	13.3	2230	34.43	101	2463
JA13- 24	17	0.191	0.1573	0.0016	0.2967	0.0043	6.4349	0.0931	0.0857	0.0014	0.9936	2427.3	17.47	1674.7	21.46	2037	12.72	1661.2	26.2	69	2427.3
JA13- 25	12	0.143	0.1638	0.0017	0.4749	0.0069	10.7247	0.1531	0.1173	0.0018	0.9840	2495.4	16.94	2505	30.13	2499.6	13.26	2241.8	33.06	100	2495.4
JA13- 26	3	0.359	0.1631	0.0017	0.4817	0.0069	10.8283	0.1531	0.1183	0.0015	0.9925	2487.8	17.13	2534.7	29.84	2508.5	13.14	2260	27.56	102	2487.8
JA13- 27	20	0.342	0.1610	0.0017	0.4765	0.0069	10.5787	0.1530	0.1169	0.0018	0.9971	2466.5	17.81	2512.2	30	2486.8	13.41	2235.2	31.97	102	2466.5
JA13- 28	15	0.157	0.1623	0.0017	0.4724	0.0067	10.5684	0.1495	0.1141	0.0017	0.9932	2479.4	17.07	2494.1	29.45	2485.9	13.13	2183.5	30.38	101	2479.4
JA13- 29	6	0.371	0.1674	0.0019	0.4878	0.0072	11.2610	0.1684	0.1221	0.0023	0.9859	2532	18.77	2561.2	31.15	2545	13.94	2327.6	41.35	101	2532
JA13- 30	15	0.175	0.1652	0.0017	0.4736	0.0068	10.7849	0.1530	0.1238	0.0017	0.9927	2509.5	16.97	2499.3	29.63	2504.8	13.19	2358.1	31.05	100	2509.5
JA13- 31	24	0.342	0.1607	0.0017	0.4689	0.0070	10.3918	0.1544	0.1130	0.0020	0.9979	2463.4	18.17	2478.8	30.63	2470.3	13.76	2163.2	36.32	101	2463.4
JA13- 32	8	0.150	0.1636	0.0017	0.4910	0.0068	11.0753	0.1547	0.1149	0.0020	0.9963	2493.5	17.26	2574.8	29.55	2529.5	13	2197.5	37.04	103	2493.5
JA13- 33	36	0.100	0.1534	0.0017	0.3243	0.0044	6.8587	0.0953	0.0798	0.0027	0.9828	2384	18.3	1810.8	21.55	2093.3	12.32	1551.3	50.44	76	2384
JA13- 34	26	1.812	0.1686	0.0019	0.4846	0.0072	11.2630	0.1684	0.0946	0.0021	0.9868	2543.7	18.47	2547.3	31.03	2545.1	13.94	1827.7	38.03	100	2543.7
JA13- 35	6	0.170	0.1594	0.0017	0.3265	0.0046	7.1754	0.1024	0.1002	0.0020	0.9895	2449.3	17.89	1821.6	22.38	2133.4	12.71	1929.9	36.57	74	2449.3
JA13- 36	19	0.222	0.1652	0.0017	0.4837	0.0067	11.0192	0.1538	0.1217	0.0021	0.9969	2509.9	17.26	2543.5	29.22	2524.8	12.99	2320.5	38.1	101	2509.9
JA13- 37	0	0.419	0.1651	0.0019	0.4725	0.0067	10.7493	0.1577	0.1242	0.0026	0.9708	2508.1	18.88	2494.4	29.46	2501.7	13.63	2367	47.07	99	2508.1
JA13- 38	7	0.049	0.1631	0.0017	0.4814	0.0068	10.8224	0.1531	0.1316	0.0030	0.9943	2488	17.35	2533.3	29.47	2508	13.15	2498.6	53.7	102	2488
JA13- 39	12	0.225	0.1653	0.0017	0.4832	0.0068	11.0051	0.1569	0.1206	0.0026	0.9913	2510.2	17.41	2541	29.7	2523.6	13.27	2301.6	47.41	101	2510.2
JA13- 40	0	0.110	0.1654	0.0017	0.4792	0.0067	10.9220	0.1527	0.1285	0.0031	0.9944	2511.4	17.35	2523.8	29.03	2516.5	13	2444.1	55.32	100	2511.4
JA13- 41	5	0.468	0.1810	0.0022	0.5105	0.0075	12.7349	0.1951	0.1180	0.0034	0.9615	2662.2	19.86	2658.9	32.11	2660.2	14.42	2253.9	61.57	100	2662.2

Table 8

Sample JA14			Isotope Ratios									Ages (Ma)									
Spot name	^{204}Pb (cps)	Th/U	^{207}Pb/^{206}Pb	± 1σ	^{206}Pb/^{238}U	± 1σ	^{207}Pb/^{235}U	± 1σ	^{208}Pb/^{232}Th	± 1σ	rho	^{207}Pb/^{206}Pb	± 1σ	^{206}Pb/^{238}U	± 1σ	^{207}Pb/^{235}U	± 1σ	^{208}Pb/^{232}Th	± 1σ	Conc. (%)	Eff. Age*
JA14-01	26	0.851	0.1679	0.0019	0.4885	0.0066	11.3074	0.1543	0.1257	0.0015	0.9874	2537	18.31	2564.2	28.49	2548.8	12.73	2392.6	26.85	98	2537
JA14-02	9	0.531	0.1640	0.0018	0.4753	0.0064	10.7466	0.1445	0.1207	0.0015	0.9971	2497.7	17.81	2506.7	27.82	2501.5	12.49	2304.1	26.29	99	2497.7
JA14-03	17	0.512	0.1636	0.0017	0.4730	0.0063	10.6656	0.1420	0.0887	0.0011	0.9975	2493.3	17.62	2496.6	27.5	2494.4	12.36	1717.7	20.71	97	2493.3
JA14-04	19	0.095	0.1635	0.0016	0.4924	0.0065	11.0932	0.1450	0.0754	0.0010	0.9838	2491.7	16.7	2580.9	28.23	2531	12.17	1468.3	19.15	96	2491.7
JA14-05	20	0.170	0.1655	0.0017	0.4697	0.0063	10.7167	0.1418	0.1249	0.0016	0.9913	2512.8	17	2482.3	27.52	2498.9	12.29	2378.7	28.16	96	2512.8
JA14-06	19	0.197	0.1642	0.0017	0.4457	0.0060	10.0887	0.1335	0.1169	0.0014	0.9897	2499.4	16.94	2376.3	26.58	2442.9	12.23	2233.9	24.95	96	2499.4
JA14-07	20	0.221	0.1662	0.0017	0.4535	0.0061	10.3875	0.1386	0.1274	0.0016	0.9968	2519.4	17.23	2411	26.91	2469.9	12.36	2423.5	28.87	94	2519.4
JA14-08	14	0.051	0.1615	0.0016	0.4637	0.0062	10.3201	0.1371	0.1133	0.0018	0.9903	2470.9	16.93	2456	27.41	2463.9	12.3	2169.7	33.18	97	2470.9
JA14-09	16	0.075	0.1627	0.0016	0.4657	0.0063	10.4451	0.1391	0.1142	0.0016	0.9906	2484	16.9	2464.7	27.55	2475.1	12.34	2185.1	29.2	100	2484
JA14-10	7	0.646	0.1631	0.0018	0.4708	0.0064	10.5866	0.1466	0.1111	0.0013	0.9875	2488.2	18.18	2487.3	28.23	2487.5	12.85	2129.6	24.11	97	2488.2
JA14-11	22	0.542	0.1655	0.0017	0.5356	0.0073	12.2248	0.1680	0.1247	0.0015	0.9972	2513.1	17.55	2765.2	30.8	2621.8	12.9	2375.2	27.14	101	2513.1
JA14-12	23	0.421	0.1658	0.0017	0.5703	0.0078	13.0381	0.1777	0.1413	0.0017	0.9978	2516	17.27	2909	31.97	2682.4	12.85	2670.4	30.14	100	2516
JA14-13	18	0.088	0.1635	0.0016	0.4883	0.0066	11.0063	0.1478	0.1192	0.0016	0.9903	2492.3	16.81	2563.1	28.69	2523.7	12.5	2276.3	28.81	100	2492.3
JA14-14	20	0.196	0.1651	0.0017	0.4896	0.0067	11.1413	0.1504	0.1168	0.0015	0.9938	2508.3	16.99	2568.7	28.8	2535	12.58	2233.2	27.12	104	2508.3
JA14-15	21	0.200	0.1649	0.0017	0.4784	0.0065	10.8732	0.1467	0.1197	0.0015	0.9930	2506	16.99	2520.5	28.35	2512.3	12.54	2285.1	27.57	99	2506
JA14-16	11	0.358	0.1641	0.0018	0.4688	0.0067	10.6024	0.1531	0.1161	0.0018	0.9856	2497.9	18.27	2478.3	29.27	2488.9	13.39	2219.1	32.46	95	2497.9
JA14-17	15	0.087	0.1623	0.0017	0.4610	0.0063	10.3179	0.1391	0.1165	0.0018	0.9930	2480.1	17.05	2444.1	27.62	2463.7	12.48	2227.3	32.5	96	2480.1
JA14-18	17	0.287	0.1631	0.0017	0.4752	0.0065	10.6842	0.1448	0.1084	0.0014	0.9951	2487.8	17.23	2506.5	28.25	2496.1	12.58	2079.9	25.95	99	2487.8
JA14-19	3	0.506	0.1645	0.0017	0.4641	0.0064	10.5258	0.1447	0.1225	0.0016	0.9956	2502.5	17.72	2457.8	27.96	2482.2	12.74	2336	28.52	99	2502.5
JA14-20	4	0.946	0.1634	0.0018	0.4770	0.0066	10.7477	0.1518	0.1238	0.0016	0.9794	2491.5	18.73	2514.2	28.8	2501.6	13.12	2359.1	28.91	100	2491.5
JA14-21	12	0.521	0.1654	0.0019	0.4738	0.0070	10.8012	0.1621	0.1138	0.0022	0.9791	2511.3	19.29	2500.1	30.45	2506.2	13.94	2178.6	39.47	110	2511.3
JA14-22	9	0.243	0.1641	0.0017	0.4743	0.0064	10.7318	0.1446	0.1248	0.0017	0.9939	2498.6	17.18	2502.4	28.12	2500.2	12.52	2377.7	31.14	116	2498.6
JA14-23	26	0.720	0.1675	0.0018	0.4889	0.0068	11.2893	0.1582	0.1290	0.0018	0.9866	2533	18.28	2565.7	29.28	2547.3	13.07	2451.7	31.95	103	2533
JA14-24	21	0.220	0.1646	0.0017	0.4719	0.0064	10.7072	0.1436	0.1217	0.0017	0.9917	2503.2	17.01	2492	27.96	2498	12.45	2320.3	29.75	102	2503.2
JA14-25	12	0.525	0.1635	0.0018	0.4737	0.0065	10.6738	0.1484	0.1255	0.0018	0.9888	2491.7	18.21	2499.7	28.48	2495.2	12.9	2389.7	31.66	101	2491.7
JA14-26	8	0.636	0.1629	0.0018	0.4681	0.0064	10.5109	0.1449	0.1207	0.0016	0.9917	2485.7	18.03	2475.2	28.11	2480.9	12.78	2302.9	29.12	99	2485.7
JA14-27	10	0.036	0.1603	0.0016	0.4632	0.0063	10.2363	0.1368	0.1253	0.0025	0.9889	2458.6	17	2453.8	27.56	2456.4	12.36	2385.5	44.24	99	2458.6
JA14-28	19	0.091	0.1624	0.0016	0.4614	0.0064	10.3267	0.1419	0.1218	0.0020	0.9859	2480.3	16.94	2445.8	28.35	2464.5	12.72	2323.9	36.13	101	2480.3
JA14-29	10	0.060	0.1617	0.0016	0.4795	0.0065	10.6869	0.1428	0.1240	0.0021	0.9902	2473.2	16.98	2524.9	28.21	2496.3	12.41	2362.4	38.03	98	2473.2
JA14-30	14	0.089	0.1613	0.0016	0.4643	0.0063	10.3215	0.1379	0.1242	0.0019	0.9890	2468.9	16.99	2458.3	27.59	2464	12.37	2366.6	33.94	101	2468.9
JA14-31	13	0.178	0.1639	0.0017	0.4513	0.0060	10.1993	0.1353	0.1270	0.0019	0.9943	2496.2	17.17	2401.2	26.74	2453	12.26	2417	33.67	100	2496.2
JA14-32	89	0.659	0.1631	0.0018	0.4710	0.0065	10.5928	0.1462	0.1147	0.0024	0.9924	2488.4	18.08	2487.8	28.27	2488.1	12.8	2193.8	42.91	100	2488.4
JA14-33	88	0.076	0.1609	0.0016	0.4574	0.0062	10.1470	0.1348	0.1094	0.0023	0.9848	2465.2	16.76	2428	27.31	2448.3	12.28	2098.5	42.22	101	2465.2
JA14-34	95	0.552	0.1652	0.0018	0.4790	0.0068	10.9097	0.1557	0.1123	0.0032	0.9903	2509.4	18.45	2523.1	29.51	2515.5	13.27	2151.7	58.25	100	2509.4
JA14-35	95	0.309	0.1631	0.0017	0.4451	0.0061	10.0113	0.1352	0.1085	0.0023	0.9916	2488.4	17.25	2373.5	27.01	2435.8	12.46	2082.2	41.51	100	2488.4
JA14-36	73	0.056	0.1613	0.0016	0.4814	0.0065	10.7052	0.1434	0.1087	0.0026	0.9873	2469.2	16.97	2533.4	28.43	2497.9	12.44	2086.5	47.55	100	2469.2
JA14-37	98	0.058	0.1603	0.0016	0.4959	0.0070	10.9566	0.1526	0.1074	0.0040	0.9850	2458.4	17.23	2596.1	30.21	2519.5	12.96	2062.3	73.01	100	2458.4
JA14-38	98	0.096	0.1617	0.0016	0.4794	0.0065	10.6884	0.1433	0.1181	0.0027	0.9861	2473.6	16.96	2524.7	28.4	2496.4	12.45	2255.6	47.92	99	2473.6
JA14-39	19	0.105	0.1655	0.0017	0.4662	0.0059	10.6332	0.1333	0.1317	0.0017	0.9921	2513	16.85	2466.8	25.9	2491.6	11.63	2499.8	30.85	102	2513
JA14-40	25	0.454	0.1657	0.0018	0.4699	0.0063	10.7286	0.1454	0.1308	0.0018	0.9891	2514.6	18.25	2483.1	27.61	2499.9	12.59	2484.9	31.32	100	2514.6
JA14-41	39	0.743	0.1665	0.0018	0.4631	0.0060	10.6223	0.1391	0.1342	0.0016	0.9846	2522.5	18.1	2453	26.31	2490.7	12.15	2544.8	28.94	96	2522.5
JA14-42	27	0.041	0.1623	0.0016	0.4463	0.0056	9.9847	0.1237	0.1304	0.0022	0.9942	2480.1	16.95	2378.9	24.78	2433.4	11.43	2477	39.31	100	2480.1
JA14-43	40	0.247	0.1572	0.0019	0.4335	0.0061	9.3656	0.1379	0.0439	0.0013	0.9591	2425.2	20.49	2321.3	27.51	2374.5	13.51	867.8	25.19	98	2425.2
JA14-44	28	0.707	0.1647	0.0018	0.4529	0.0058	10.2779	0.1335	0.1289	0.0016	0.9812	2504.3	18.17	2408.1	25.6	2460.1	12.02	2450.5	28.34	101	2504.3
JA14-45	28	0.092	0.1648	0.0017	0.4426	0.0055	10.0551	0.1244	0.1233	0.0020	0.9969	2505.7	17.26	2362.2	24.39	2439.9	11.43	2350.6	35.21	95	2505.7
JA14-46	15	0.081	0.1656	0.0017	0.4600	0.0057	10.5007	0.1295	0.1264	0.0018	0.9954	2513.9	16.9	2439.6	25.17	2480	11.44	2405	31.71	103	2513.9
JA14-47	17	0.249	0.1646	0.0017	0.4716	0.0058	10.6953	0.1315	0.1287	0.0015	0.9945	2503	16.96	2490.5	25.52	2497	11.42	2446.2	27.16	106	2503
JA14-48	37	0.454	0.1657	0.0017	0.4626	0.0057	10.5650	0.1312	0.1237	0.0015	0.9922	2514.6	17.47	2450.8	25.11	2485.6	11.52	2357.6	26.76	102	2514.6

Table 9

Sample JA7		Isotope Ratios							Ages (Ma)							
Spot name	^{204}Pb (cps)	^{207}Pb/ ^{206}Pb	± 1σ	^{206}Pb/ ^{238}U	± 1σ	^{207}Pb/ ^{235}U	± 1σ	rho	^{207}Pb/ ^{206}Pb	± 1σ	^{206}Pb/ ^{238}U	± 1σ	^{207}Pb/ ^{235}U	± 1σ	Conc. (%)	Eff. Age*
m01	0	0.16516	0.00226	0.47185	0.00779	10.74702	0.18747	0.946433	2509.2	22.86	2491.7	34.12	2501.5	16.2	99	2509.2
m02	5	0.16243	0.00189	0.4686	0.00764	10.49343	0.17216	0.993748	2481.1	19.52	2477.4	33.52	2479.3	15.21	100	2481.1
m03	18	0.16095	0.00168	0.4581	0.00725	10.16555	0.15833	0.984135	2465.7	17.52	2431.2	32.07	2449.9	14.4	99	2465.7
m04	1	0.16315	0.00191	0.45825	0.00742	10.30696	0.16847	0.990625	2488.6	19.63	2431.8	32.8	2462.7	15.13	98	2488.6
m06	18	0.16045	0.00173	0.45936	0.00734	10.16183	0.16051	0.988524	2460.4	18.1	2436.7	32.42	2449.6	14.6	99	2460.4
m07 +	0	0.16229	0.00234	0.5531	0.00946	12.37379	0.22533	0.939228	2479.7	24.12	2838.1	39.25	2633.2	17.11	114	2479.7
m09 +	0	0.15469	0.00164	0.46172	0.00738	9.84738	0.15479	0.983432	2398.4	17.88	2447.1	32.54	2420.6	14.49	102	2398.4
m11 +	13	0.15369	0.00162	0.42534	0.00667	9.01211	0.14043	0.993674	2387.4	17.89	2284.7	30.17	2339.2	14.24	96	2387.4
m12	9	0.15968	0.00201	0.47212	0.0076	10.39288	0.17385	0.962326	2452.3	21.14	2492.9	33.26	2470.4	15.49	102	2452.3
m13	10	0.16212	0.00182	0.46227	0.00735	10.3292	0.16496	0.995588	2477.9	18.83	2449.6	32.39	2464.7	14.78	99	2477.9
m16	5	0.15909	0.00173	0.45348	0.00718	9.9414	0.15749	0.99945	2446	18.24	2410.7	31.86	2429.4	14.62	99	2446
m17	1	0.15725	0.00161	0.44838	0.007	9.71932	0.14943	0.984805	2426.3	17.29	2388	31.17	2408.5	14.16	98	2426.3
m20	3	0.16196	0.00178	0.45231	0.00719	10.09821	0.16065	0.999209	2476.2	18.46	2405.5	31.9	2443.8	14.7	97	2476.2
m22	6	0.16157	0.00172	0.46552	0.00733	10.36699	0.16193	0.991994	2472.1	17.82	2463.9	32.25	2468.1	14.47	100	2472.1
m25	11	0.16125	0.00175	0.45378	0.00715	10.08368	0.15832	0.996451	2468.8	18.23	2412	31.69	2442.5	14.5	98	2468.8
m26	34	0.16086	0.00175	0.46644	0.00733	10.33949	0.16249	0.999955	2464.7	18.25	2467.9	32.23	2465.6	14.55	100	2464.7

Table 10

Sample	Element analysis- Chondrite Normalised																							
	Na23	Mg24	Al27	Si29	K39	Ca43	Ti49	Fe57	Zr90	La139	Ce140	Pr141	Nd146	Sm147	Eu153	Gd157	Tb159	Dy163	Ho165	Er166	Tm169	Yb172	Lu175	Hf178
JA31_04	0	0.00002	0.00056	1.2	0	0	0.0162	0.00023	98029.04	0	7.67	0	0.836	10.81	3.22	71.3	167.71	302.95	474.61	663.03	1018.38	1429.45	1473.59	75195.33
JA31_02	0.00058	0.00031	0.0176	1.15	0.0211	0	0.0166	0.00051	97010.8	3.86	28.73	14.75	23.68	64.41	29.02	132.65	159.38	184.76	218.27	268.73	386.03	533.68	595	79312.05
JA31_06	0.00034	0.00103	0.0501	1.33	0.0105	0	0.0222	0.00065	113665.5	7.11	19.02	8	9.66	29.22	16.78	95.61	190.36	343.07	553.38	798.09	1199.37	1656.48	1824.05	84447.3
JA31_07	0	0.00007	0.00429	1.03	0.0042	0	0.0148	0.00024	91126.61	0.236	8.37	1.38	2.73	15.98	6.99	75.73	166.76	306.04	477.16	673.09	988.02	1325.57	1522.6	73035.12
JA31_08	0.0069	0.00158	0.14	1.31	0.099	0	0.0252	0.00204	115588.5	12.89	61.53	44.09	64.47	127	139.2	179.3	251.09	450	819.51	1393.99	2523.06	4060.52	4969.15	88061.87
JA31_10	0.00162	0.00104	0.0345	1.63	0.083	0	0.0256	0.00125	139603.6	5.01	33.54	12.85	21.27	62.95	34.63	167.74	291.93	529.1	903.28	1326.59	2020.11	2828.39	2881.31	72954.58
JA31_13	0.00292	0.0058	0.066	0.99	0.53	0	0.597	0.00306	95567.28	1.52	23.18	4	6.83	22.42	9.23	71.07	155.29	313.71	572.35	920.8	1497.88	2161.62	2463.85	66852.92
JA31_14	0.00111	0.00024	0.0112	1.08	0.0184	0	0.0164	0.00045	100651.8	1.008	17.83	3.96	9.21	43.49	19.23	162.38	308.65	576.17	1010.66	1504.43	2157.24	2831.61	3249.6	55483.38
JA32_01	0.00173	0.00004	0.00052	0.49	0.0162	0	0.0099	0.00018	60245.87	1.26	5.44	1.37	1.93	7.72	2.93	39.36	98.45	198.52	343.61	530.04	910.02	1418.24	1457.34	44047.5
JA32_06	0.0051	0.00071	0.046	1.25	0.042	0	0.0298	0.00147	113284.3	60.63	292.98	205.41	284.43	526.33	402.91	510.03	469.86	607.24	970.45	1593.43	2926.79	4640.27	5359.42	85328.41
JA32_05	0.0008	0.00024	0.0052	1.11	0.0162	0	0.0096	0.00058	100162.3	4.61	28.97	7.35	12.57	40.2	18.25	129.29	253.3	467.82	808.97	1195.99	1812.35	2478.54	2539.32	53597.92
JA32_08	0.00197	0.00034	0.0167	0.95	0.041	0	0.014	0.00094	86609.84	15.25	56.88	53.62	71.29	200.05	83.07	184.61	241.26	389.74	658	1096.08	2023.16	3342	3721.9	68951.54
JA32_07	0.00083	0.00035	0.032	1.21	0.036	0	0.0203	0.00104	111690.5	16.62	71.82	51.38	69.92	125.88	91.87	169.97	250.65	449.02	779.03	1241.73	2066.95	3035.5	3401.42	93230.25
JA32_12	0.0042	0.0047	0.134	1.27	0.79	0	0.0226	0.0061	106814.7	26.17	91.28	79.36	109.5	217.02	135.24	268.08	311.33	465.09	751.98	1179	1956.17	2959.62	3520.32	76365.44
JA14_36	0.00043	0.00001	0	0.967	0	0	0.0133	0.00027	89576.87	0	18.81	0.369	1.82	21.6	3.09	105.47	191.77	301.1	410.09	507.37	704.04	911.53	849.44	62509.95
JA14_47	0.00073	0.00009	0.00495	0.851	0.00606	0	0.0153	0.00221	79569.34	0.224	14.96	0.917	2.09	19.86	8.78	112.15	281.08	582.25	999.9	1442.88	2048.81	2614.01	2761.76	61504.63
JA14_46	0	0.00001	0.00042	0.9	0	0	0.0159	0.00023	87313.71	0.134	15.29	0.303	1.32	17.64	1.89	113.4	304.21	664.21	1166.36	1678.04	2359.97	2975.91	3071	66969.57
JA14_24	0	0.00002	0.00032	0.954	0	0	0.0202	0.00013	89124.93	0	16.79	0.406	1.79	18.81	2.36	113.12	273.93	564.58	998.94	1477.25	2183.16	2895.9	3049.43	67733.07
JA14_15	0.00036	0.0001	0.00136	0.97	0.0073	0	0.0245	0.00015	88585.6	0	17.61	0.369	1.63	19.97	2.56	105.52	230.87	461.28	797.96	1194.62	1813.56	2512.91	2667.43	66000.69
JA14_17	0.00163	0.00004	0.00127	0.94	0.0388	0	0.0266	0.0003	89020.44	1.583	18.94	2.03	4.28	27.59	18.87	127.86	260.31	470.5	721.7	983.29	1369.89	1762.68	1701.26	67424.84
JA14_18	0.00049	0.00006	0.00064	0.97	0.0062	0	0.0134	0.0002	88595.49	0.077	18.28	0.446	2.16	24.5	2.54	137.74	296.78	549.52	883.18	1177.36	1635.11	2064.88	1918.91	64825.76
JA14_13	0	0.00011	0.00137	0.92	0	0	0.016	0.00027	87678.66	0.05	14.66	0.4	1.42	16.97	4.02	105.67	304.97	670.5	1139.81	1601.37	2315.02	2988.73	2792.01	63657.55
JA14_9	0	0.00001	0.00036	0.98	0	0	0.0141	0.00026	87895.67	0	18.2	0.409	1.88	20.89	2.39	113.24	222.68	381.35	558.3	737.17	1059.73	1415.74	1376.88	64477.24
JA14_8	0.00178	0.00005	0.00114	0.99	0.0235	0	0.062	0.00035	89081.23	0.178	19.59	0.64	2.05	22.7	7.62	94.38	148.28	205.56	255.25	290.37	387.03	516.85	534.89	66876.66
JA14_5	0	0.00001	0.00024	1.01	0	0	0.0176	0.00035	86796.97	0	21.32	0.579	2.63	31.04	3.65	198.27	509.67	1072.3	1834.94	2619.61	3704.21	4722.99	4663.81	69672.22